การจำลองการจับยึดอนุภาคตัวพายาโดยเป้าแม่เหล็ก

ว่าที่ร้อยตรีณัฐพล ชุมพลอโนมคุณ

วิทยานิพนธ์นี้เป็นส่วนหนึ่งของการศึกษาตามหลักสูตรปริญญาวิทยาศาสตรดุษฎีบัณฑิต
สาขาวิชาฟิสิกส์ ภาควิชาฟิสิกส์
คณะวิทยาศาสตร์ จุฬาลงกรณ์มหาวิทยาลัย
ปีการศึกษา 2559

SIMULATION OF DRUG CARRIER PARTICLE CAPTURE BY MAGNETIC TARGET

Acting Sub Lieutenant Natthaphon Choomphon-anomakhun

A Dissertation Submitted in Partial Fulfillment of the Requirements

for the Degree of Doctor of Philosophy Program in Physics

Department of Physics

Faculty of Science

Chulalongkorn University

Academic Year 2016

Thesis Title	SIMULATION OF DRUG CARRIER PARTICLE CAPTURE BY MAGNETIC TARGET
By	Acting Sub Lieutenant Natthaphon Choomphon-anomakhun
Field of Study	Physics
Thesis Advisor	Associate Professor Dr.Mayuree Natenapit, Ph.D.

Accepted by the Faculty of Science, Chulalongkorn University in Partial Fulfillment of the Requirements for the Doctoral Degree

.....Dean of the Faculty of Science
(Associate Professor Dr.Polkit Sangvanich, Ph.D.)

THESIS COMMITTEE

.....Chairman
(Assistant Professor Dr.Rattachat Mongkolnavin, Ph.D.)

.....Thesis Advisor
(Associate Professor Dr.Mayuree Natenapit, Ph.D.)

.....Examiner
(Associate Professor Dr.Nakorn Phaisangittisakul, Ph.D.)

.....Examiner
(Assistant Professor Dr.Nuttakorn Thubthong, Ph.D.)

.....External Examiner
(Dr.Supitch Khemmani, Ph.D.)

ณัฐพล ชุมพลอโนมคุณ : การจำลองการจับยึดอนุภาคตัวพายาโดยเป้าแม่เหล็ก (SIMULATION OF DRUG CARRIER PARTICLE CAPTURE BY MAGNETIC TARGET) อ. ที่ปรึกษาวิทยานิพนธ์หลัก: รศ. ดร.มยุรี เนตรนภิส, 128 หน้า.

การจับยึดอนุภาคตัวพายาแบบฝังเป้าแม่เหล็ก ทำได้โดยฝังเป้าแม่เหล็กเฟร์โรทรงกลมไว้ภายในหลอดเลือด และให้สนามแม่เหล็กสม่ำเสมอจากภายนอก สำหรับทั้งกรณี (ก) ไม่รวม และ (ข) รวมผลกระทบจากผนังหลอดเลือดต่อการไหลของเลือดได้ถูกศึกษาวิจัยแบบสามมิติ สำหรับกรณี (ก) ความเร็วการไหลของเลือดอยู่ในรูปแบบเชิงวิเคราะห์ สำหรับกรณี (ข) ความเร็วของเลือด ณ ตำแหน่งใดๆ รอบเป้าแม่เหล็กหาได้โดยการใช้การประมาณค่าภายในแบบเชิงเส้นคู่จากผลความเร็วเลือดเชิงตัวเลข ในงานวิจัยนี้ พื้นที่การจับยึดของอนุภาคแม่เหล็กตัวพายา (A_s) สำหรับทั้งสองกรณีถูกกำหนดโดยการวิเคราะห์เส้นทางการเคลื่อนที่ของอนุภาคซึ่งจำลองมาจากสมการการเคลื่อนที่ จากนั้น ผลกระทบจากตัวแปรต่างๆ เช่น ชนิดของสารแม่เหล็กเฟร์โรในเป้าแม่เหล็กและอนุภาคแม่เหล็กตัวพายา อัตราการไหลของเลือด สัดส่วนโดยมวลของสารแม่เหล็กเฟร์โรในอนุภาคแม่เหล็กตัวพายา รัศมีเฉลี่ยของอนุภาคแม่เหล็กตัวพายา (R_p) และขนาดของสนามแม่เหล็กที่ให้จากภายนอก ($\mu_0 H_0$) ต่อ A_s ถูกนำมาประเมินผล งานวิจัยนี้ได้รายงานค่า $\mu_0 H_0$ และ R_p ที่เหมาะสมสำหรับการออกแบบการจับยึดอนุภาคตัวพายาแบบฝังเป้าแม่เหล็กในหลอดเลือดแดงใหญ่ และหลอดเลือดแดงรอง นอกจากนี้ ได้มีการพิจารณาผลกระทบของการสะสมของอนุภาคแม่เหล็กตัวพายาต่อการไหลของของไหลและสนามแม่เหล็กรอบๆ เป้าแม่เหล็กที่ถูกแมกนิไตซ์ การจับยึดอนุภาคตัวพายาแบบฝังเป้าแม่เหล็กในสองมิติสำหรับการจับยึดและสะสมอนุภาคแม่เหล็กตัวพายาเชิงพลวัต โดยใช้เป้าแม่เหล็กเฟร์โรทรงกระบอกได้รับการพัฒนาขึ้น ความเร็วและความเข้มข้นเชิงปริมาตรของอนุภาคแม่เหล็กตัวพายา และของไหลภายในพื้นที่ควบคุมหาได้โดยการใช้แบบจำลองเชิงพลวัตนี้ ผลลัพธ์ที่ได้แสดงให้เห็นถึงความสามารถในการทำนายพฤติกรรมเชิงพลวัตของการจับยึดและสะสมอนุภาคแม่เหล็กตัวพายารอบเป้าแม่เหล็กเฟร์โรทรงกระบอกอย่างใกล้เคียงความเป็นจริง

ภาควิชา ฟิสิกส์ ลายมือชื่อนิสิต .....

สาขาวิชา ฟิสิกส์ ลายมือชื่อ อ.ที่ปรึกษาหลัก .....

ปีการศึกษา 2559

5472880523 : MAJOR PHYSICS

KEYWORDS: IMPLANT-ASSISTED MAGNETIC DRUG TARGETING / HIGH GRADIENT MAGNETIC SEPARATION / MAGNETIC DRUG CARRIER PARTICLES / SPHERICAL FERROMAGNETIC TARGETS / CYLINDRICAL FERROMAGNETIC TARGETS / 3-D PARTICLE TRAEJCTORIES / DYNAMIC PARTICLE CAPTURE / PARTICLE ACCUMULATION

NATTHAPHON CHOOMPHON-ANOMAKHUN: SIMULATION OF DRUG CARRIER PARTICLE CAPTURE BY MAGNETIC TARGET. ADVISOR: ASSOC. PROF. DR.MAYUREE NATENAPIT, Ph.D., 128 pp.

The three-dimensional (3-D) implant assisted-magnetic drug targeting (IA-MDT) using ferromagnetic spherical targets implanted within blood vessels and subjected to a uniform externally applied magnetic field, for both (a) excluding and (b) including the effect from the vessel walls on the blood flow, were investigated. For the case (a), the blood velocity was in analytical form. For the case (b), the blood velocity at any particle position was obtained by applying bilinear interpolation to the numerical blood velocity data. In this research, the capture areas (A_s) of MDCPs for both cases were determined by the analysis of particle trajectories simulated from equations of motion. Then, the effects of various parameters, such as types of ferromagnetic materials in the targets and MDCPs, blood flow rates, mass fraction of the ferromagnetic material in the MDCPs, average radii of MDCPs (R_p) and the externally applied magnetic field strength ($\mu_0 H_0$) on the A_s were evaluated. The appropriate $\mu_0 H_0$ and R_p for the IA-MDT designs in large arteries and arterioles were reported. Furthermore, the impacts of the accumulation of MDCPs on the fluid flow and the local magnetic field around the magnetized target were considered. A two-dimensional (2-D) IA-MDT for the dynamic capture and accumulation of MDCPs by a ferromagnetic cylindrical target was developed. The velocities and volume concentrations of the MDCPs and fluid within the control area were obtained by using this dynamic model. The obtained results were shown to be capable of realistically predicting the dynamic behaviors of MDCP capture and accumulation around a ferromagnetic cylindrical target.

Department: Physics Student's Signature .....

Field of Study: Physics Advisor's Signature .....

Academic Year: 2016

ACKNOWLEDGEMENTS

First of All, I am very grateful to express my deeply thank to Assoc. Prof. Dr. Mayuree Natenapit who is my advisor. My research, published papers and this thesis cannot be accomplished without guidance, support and patience of my advisor through six years of my Ph.D. program. Also, I would like to thank the thesis committee: Asst. Prof. Dr. Rattachat Mongkolnavin, Assoc. Prof. Dr. Nakorn Phaisangittisakul, Asst. Prof. Dr. Nuttakorn Thubthong and Dr. Supitch Khemmani for their valuable comments and suggestions.

Moreover, I would like to express my appreciation to Prof. Dr. James A. Ritter and Prof. Dr. Armin D. Ebner for their supervision and valuable suggestions during my one year research trip on Feb, 2015 to Jan, 2016 at Department of Chemical Engineering, University of South Carolina, Columbia, South Carolina, USA.

Finally, I would like to express my gratitude to the Thailand Research Fund through the Royal Golden Jubilee Ph.D. Program (Grant no. PHD/0170/2553) for providing financial support during my Ph.D. program. The research grants from the Chulalongkorn University Centenary Academic Development Project (under the Center of Innovative Nanotechnology, Chulalongkorn University) and the 90th Anniversary of Chulalongkorn University Fund are also gratefully acknowledged.

CONTENTS

Page

Page

Page

Page

Page

Lists of Figures

Lists of Tables

Lists of Abbreviations

HGMS	High gradient magnetic separation
MDT	Magnetic drug targeting
IA-MDT	Implant assisted-magnetic drug targeting
MDCPs	Magnetic drug carrier particles
ρ_b	Blood density
ρ_w	Density of water
η_b	Blood viscosity
μ_w	Viscosity of water
$\mu_{\max}$	Maximum fluid (slurry) viscosity
v_{avg}	Inlet average blood flow rates
v_0	Inlet average blood flow rates
u_0	Average fluid (slurry) velocity at the inlet
$\mu_0 H_0$	Applied magnetic field strength
$x_{fm,p}$	Weight fraction of material in MDCPs
$\rho_{fm,p}$	Density of materials inside MDCPs
$\rho_{pol,p}$	Density of polymer material in MDCPs
$\rho_{fm,w}$	Density of materials inside the cylindrical target
$M_{s,s}$	Saturation magnetization of material in spherical target
$M_{w,s}$	Saturation magnetization of material in cylindrical target
$M_{fm,p,s}$	Saturation magnetization of material in spherical MDCP
a	Spherical target radius
R_w	Cylindrical target radius
R_p	Average radii of MDCPs
$\chi_{s,0}$	Magnetic susceptibility of materials in Spherical target at zero magnetic field
$\chi_{w,0}$	Magnetic susceptibility of materials in Cylindrical target at zero magnetic field

$\chi_{fm,p,0}$	Magnetic susceptibility of materials in MDCPs at zero magnetic field
$\mu_0 H_s$	Magnetic field strength required for the materials in cylindrical and spherical targets becoming magnetically saturated
T	Temperature
w	Control area width
L	Control area height
ϕ_0	Initial volume fraction of MDCPs

CHAPTER I
INTRODUCTION

1.1 Implant Assisted-Magnetic Drug Targeting

High gradient magnetic separation (HGMS) has been widely used in industries such as mineral processing [1] and waste water treatment [2], with its development and implementation dating back more than 40 years. One of the more recent and still evolving applications is implant assisted-magnetic drug targeting (IA-MDT) techniques [3-11].

The advantages of magnetic drug targeting (MDT) techniques based on the use of magnetic drug carrier particles (MDCPs) and an externally applied magnetic field are the ability of the MDCPs to access disease sites and their guidable property to specific locations, which results in efficient drug delivery to specific locations while this cannot be achieved by the conventional drug administration. Consequently, the drug concentration at the disease sites is increased, while the quantity of the drug required and the concentration of the drug at the non-target sites are both reduced, which reduces the side effects on normal tissues [12, 13]. Moreover, the effectiveness in using an external applied magnetic field to control the trajectories of MDCPs in MDT depends not only on the magnetic field strength but also on its field gradient which can strengthen the magnetic force acting on the MDCPs carried by blood stream.

The limitation of using MDT in humans is that it requires a strong magnetic force that is high enough to overcome the effect of the blood drag force so that it works effectively at low blood flow rates, such as in the capillaries [14] by using a low magnetic field strength. For high blood flow rate sites, such as large arteries, much stronger magnetic fields are required to retain the MDCPs [13, 15]. In addition, the magnetic field strength from a permanent magnet located outside the body decreases steeply with the distance deep in the tissue, and so the MDT becomes less efficient as the depth of the disease site increases [15-17]. IA-MDT systems have been proposed

to locally increase the magnetic force acting on the MDCPs. The principle of HGMS has been employed [18], where a weak magnetic field around target sites located deep under the skin can be compensated for by increasing of a local magnetic field and its high gradient produced by magnetized implanted ferromagnetic targets, such as wires [7, 18-21], a stent [5, 6, 22, 23] or spherical seeds [9, 14, 24], near to or within the disease sites. Since the magnetic force acting on the MDCPs depends on a local magnetic field strength and its field gradient therefore the IA-MDT techniques can improve the efficiency of traditional MDT.

There are theoretical and in vitro experimental studies that support the feasibility and effectiveness of using IA-MDT for targeting MDCPs in blood vessels. For example, Chen et al. [23, 25] theoretically evaluated the capture of MDCPs by a magnetizable intravascular stent, whilst in vitro experiments have been conducted for IA-MDT using ferromagnetic stents [26-28], and IA-MDT using ferromagnetic seeds as implants has been investigated both theoretically [14] and by in vitro experimental approaches [29]. Cregg et al. [30] incorporated the superparamagnetic property of MDCPs and calculated the capture distance using a two-dimensional (2-D) trajectory model. In addition, they considered the effects of the magnetic dipole-dipole and hydrodynamic interactions on two MDCPs with a seed implant [24], including the effects of both interactions for multiple particles with a magnetizable stent as the implant [5]. Mardinoglu et al. [6] presented the effects of mechanical forces generated by blood pressure due to pulsatile blood circulation on IA-MDT with a magnetizable stent, including the effects of both dipole-dipole and hydrodynamic interactions. Hournkumnuard and Natenapit [10] further explored the theory of IA-MDT focusing on the targeting of ferromagnetic MDCPs of nano-size by diffusive capture using dilute ferromagnetic micro-wires implanted in small blood vessels, such as small veins. The distribution of the MDCPs was interpreted in 2-D in terms of the particle volume concentration. Furthermore, IA-MDT has received much attention from many researchers over recent years [4-6, 8-11, 19, 21, 22] .

This thesis reports three main topics of our investigations which are introduced as follows.

1.2 Three-Dimensional Trajectory Model for Magnetic Drug Targeting Using Micro-Spheres Implanted Within Large Blood Vessels

In clinical treatments, the spherical targets can be implanted in the body using minimally invasive techniques, such as transdermal injection, instead of angioplasty for targets, such as using stents and catheter tips [14]. Therefore, the use of spherical geometric targets is appropriate for IA-MDT systems because of their simple administration procedure, especially in microvasculature where stents and catheter tips cannot be implanted. The IA-MDT using spherical targets has been explored theoretically [9, 14, 24, 31, 32]. For example, a IA-MDT model using spherical targets for the capture of MDCPs in capillary beds was considered and 2-D theoretical modeling was assumed in order to reduce the complexity of the problem by Aviles et al. [14].

In Chapter II, we focuses on IA-MDT using ferromagnetic spherical targets implanted within large blood vessels, such as arteries, and subjected to a uniform externally applied magnetic field under the influence of potential flow with negligible effect from the vessel wall. The 3-D model of the IA-MDT system is used with the analytic blood velocity to determine the trajectories of the MDCPs computationally simulated from the equations of motion. Then, the capture cross-section areas of MDCPs are determined from the analysis of particle trajectories. The simulation results based on the realistic 3-D model should provide a more accurate prediction of effectiveness of the IA-MDT. Since it is difficult to capture MDCPs in the large blood vessels with a high blood flow rate, IA-MDT proposes the most advantage in improving the performance of drug delivery systems. The effectiveness of the IA-MDT is evaluated and design suggestions are reported based on the analysis of the capture cross-section areas from the results provided in this chapter.

1.3 Three-Dimensional Magnetic Drug Targeting With Spherical Targets by Bilinear Interpolation for Determining the Blood Velocity Profiles

In Chapter III, We investigates the general 3-D IA-MDT model using ferromagnetic spherical targets implanted within arterioles and subjected to a uniform externally applied magnetic field. The blood flow in the circular vessel is categorized as a laminar flow regime and the effect from the vessel wall on the blood flow is considered. Therefore, the blood flow velocity is determined numerically using computational fluid dynamics (CFD) software. The capture cross-section areas of the MDCPs are determined from analysis of the particle trajectories that are computationally simulated from the equations of motion. The blood velocity around the target inside the blood vessels is obtained by applying bilinear interpolation [33] to the blood velocity data generated by the CFD software. The effects on the capture-cross section areas, with respect to variations in the externally applied uniform magnetic field strength, types of ferromagnetic materials in the target and MDCPs, average blood flow rates, weight fraction of ferromagnetic material in MDCPs and average radii of MDCPs, are investigated and the design suggestions are reported.

1.4 Simulation of Dynamic Magnetic Drug Carrier Particle Capture and Accumulation around a Ferromagnetic Cylindrical Target

The force balance concept is generally used for modeling the trajectories of MDCPs in IA-MDT [7, 14, 18, 20, 23]. The equations of motion of MDCPs are created and solved in order to obtain the trajectories of MDCPs. The capture cross-sections of MDCPs are evaluated based on this trajectory analysis method. In the case of ultra-fine MDCPs where the diffusion process is more important than other effects, the trajectory analysis method is not appropriate to use. In this case, the continuity equation with the influence of external forces, such as magnetic, drag and Brownian forces, expressed through the concentration of MDCPs is solved to obtain the steady-state distribution of MDCP concentration around the target [3, 10, 34]. However, these

widely studied IA-MDT models [18, 23, 25] are based on the clean target condition, where the effects of the accumulation of MDCPs on both the fluid flow and magnetic fields around the magnetized target are not taken into account. These clean target models are then applicable only at the very early stages of the capture process of MDCPs and may be seriously in error [35].

Moreover, the main factor for determining the performance of an HGMS-type system appears to be magnetic particle accumulation or buildup around the target and not particle capture [36]. This is because the accumulation of MDCPs on a target changes the geometry of the target [37], consequently affecting the flow pattern and local magnetic field [35] around it. This then affects the efficiency of MDCP capture. Therefore, the dynamic MDCP collection process and its effects on both the fluid flow and magnetic field around the target are the important unresolved issues in determining the efficiency of IA-MDT system from a mathematical model.

There are several studies dedicated to observing, measuring and predicting the accumulation or buildup of MDCPs around a target in HGMS-type systems [1, 35-44]. For example, the rate equation for modeling the buildup of particles on a ferromagnetic wire has been developed by Cowen et al. [45], a practical static HGMS model to predict the maximum particle accumulation on the wire based on finding the region of particle buildup has been proposed and compared to experiments [36, 41], a model for the nanoparticle capture based on calculating the limit of static nanoparticle buildup around the wires has been presented by Moeser et al. [42], the mass of solids collected in the collection zones were calculated and compared to the experimental results for the static models with cylindrical and spherical targets in traverse configuration were developed by Ebner and Ritter [38], and Zheng et al. [1] investigated the influence of magnetic field strength on the behavior of the magnetic monomers and intergrowths in HGMS. However, except for the works of Magnet et al. [23] and Chen et al. [20], the associated models are all steady-state models and the fluid flow is assumed to be in potential flow. In addition, the effects of magnetic particle collection on the fluid flow and magnetic fields around the target are neglected. In contrast, Magnet et al. [23] developed a two phase thermodynamic model that includes the effects of the fluid flow and magnetic field on the

nanoparticle cloud surface around the wire, with the magnetic field oriented parallel to the fluid flow. However, this is also a steady-state model. The most advanced and comprehensive work that predicts the buildup profile or shape of magnetic particle accumulation around a wire was developed recently by Chen et al [35]. Their dynamic model includes the effect of magnetic particle accumulation on a single wire on the fluid flow and magnetic field by treating the dynamic growth process as a moving boundary problem. However, the buildup velocity is determined by using the particle trajectory analysis, and the incompressible fluid flow and magnetic particle concentration are considered only at the steady-state. Their model also predicts magnetic particle buildup shapes that are not found in experimental results.

Chapter IV presents a 2-D IA-MDT model to investigate dynamic capture and accumulation of MDCPs on a single ferromagnetic cylindrical target. This dynamic model includes the effect of the accumulation of MDCPs on both the fluid flow and local magnetic field around the magnetized target manifested by the volume concentration of MDCPs within the control area and the magnetization of MDCPs. The effect of the accumulation of MDCPs on the fluid flow is considered by creating the fluid viscosity as a function of the volume concentration of MDCPs, with imposed maximum particle concentration and maximum fluid viscosity limits to avoid infinite particle concentrations. The effect of the accumulation of MDCPs on the local magnetic field around the target is considered by including the magnetization of MDCPs in the dynamic model. This 2-D dynamic IA-MDT model is described in detail in Chapter III, along with some corresponding simulation results from the model that reveal the realistic time-dependent (dynamic) behaviors of MDCP capture and accumulation around a magnetized ferromagnetic cylindrical target.

CHAPTER II
THREE-DIMENSIONAL TRAJECTORY MODEL FOR MAGNETIC DRUG TARGETING USING MICRO-SPHERES IMPLANTED WITHIN LARGE BLOOD VESSELS

In this chapter, we investigates the capture of MDCPs by the spherical ferromagnetic targets in 3-D IA-MDT. The spherical targets with dilute volume packing fraction are implanted within large blood vessels. An external uniform magnetic field is applied, perpendicular to inlet blood flow direction, in order to magnetize the target then the high gradient magnetic field is created. In this work, the single sphere model is used for the description of the magnetic and blood flow fields around the spherical target. The blood flow in the vessel is categorized into potential flow with negligible the effect from the vessel wall. The particle trajectories are simulated from the equations of motion of MDCPs with analytical blood velocity. The capture areas are determined from the analysis of the particle trajectories. The simulation results are compared with those of previously published works [25, 46] in order to validate the computational program used in this work. The effects of externally applied magnetic field strength on both the capture distance for the cylindrical target and the capture area for spherical target are investigated. We also study the effects of MDCP size on the capture areas with varying types of the ferromagnetic materials in targets and MDCPs, weigh fractions of the ferromagnetic materials in MDCPs and inlet blood flow rates. Moreover, the physical effects of magnetization saturation of ferromagnetic materials within MDCPs and targets are analyzed. The results in this chapter yield the predictions of MDCP sizes that are appropriate for various designs of IA-MDT systems.

2.1 Problem Definition

In this chapter, the dilute ferromagnetic micro-spheres implanted within a certain size of a large blood vessel are considered. An external uniform magnetic field $\boldsymbol{H}_0$ is applied across the considered part of the blood vessel and perpendicular to blood flow velocity $(\boldsymbol{v}_0)$. This is a scenario similar to the transverse mode of MDT as was presented in the work of Furlani [47], but without an implanted ferromagnetic target. The MDCPs, which consist of ferromagnetic materials, coating materials and therapeutic drug agents, are carried by the bloodstream towards the implanted spherical targets of an average radius a. The high gradient magnetic field exists around the magnetized targets, thus creating a strong magnetic force acting on the MDCPs, as explained by the high gradient magnetic separation concept [18, 48]. For dilute volume packing fraction of the targets in the part of the blood vessel considered, the single sphere model offers a good approximation for the description of the magnetic and blood flow fields around the sphere. In this research, large blood vessels, such as arteries, and types of ferromagnetic materials in the target and MDCPs such as iron, SS409 and magnetite, are considered. Figure 2.1 shows a MDCP of radius R_p at the position indicated by spherical coordinates (r,θ,φ) with the target at origin, external magnetic field $(\boldsymbol{H}_0)$ and inlet blood flow velocity $(\boldsymbol{v}_0)$ directions.

We consider the MDCPs with average radii of larger than 100 nm therefore particle capture by interception is dominated while the diffusion process is negligible. The target radius is chosen to be much less than the blood vessel radius to avoid embolism effect caused by aggregation of MDCPs within the blood vessel. In addition, the target size has to be large enough compared to the size of the MDCPs in order to allow a large retention area on the target surface then the base value for a of 26 $\mu\mathrm{m}$ for the MDCPs of average radii less than 3 $\mu\mathrm{m}$ is used. In this case, the low build-up of MDCPs on the target surface, which reduces the effectiveness of MDT, is expected. The inlet blood flow rate $(\boldsymbol{v}_0)$ of the range 0.1-0.3 ms^{-1}, blood density (ρ_b) of 1040 $\mathrm{kg\,m}^{-3}$ and blood viscosity (η_b) of $3.0\times10^{-3}\mathrm{kg\,m}^{-1}\mathrm{s}^{-1}$ are used in the simulations. The blood flow passing the target is taken to be of potential flow type since the

Reynolds number (Re = $2a\rho_b v_0/\eta_b$) is much greater than unity. The other parameters used in this simulation are given in Table 2.1.

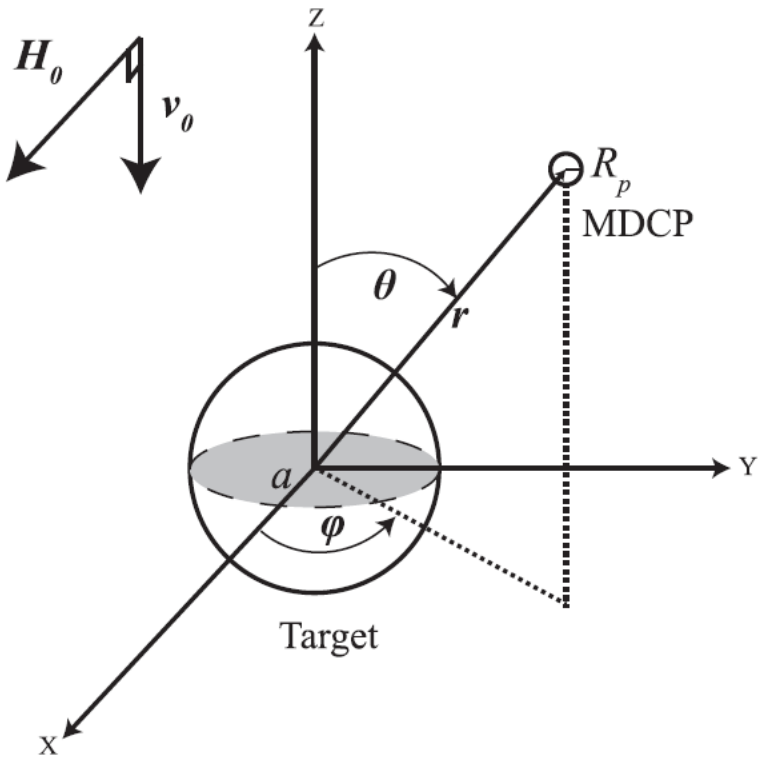

Figure 2.1 A spherical target with radius of a, the MDCP with radius of R_p, the uniform inlet blood velocity $(\boldsymbol{v}_0)$ in $-\hat{\boldsymbol{z}}$ direction and the uniform externally applied magnet field $(\boldsymbol{H}_0)$ in $\hat{\boldsymbol{x}}$ direction are shown.

Table 2.1 The parameters used in this research

Parameters	Symbol	Value(s)	SI Unit
Blood density	ρ_b	1.040×10^{3}	kg m^{-3}
Blood viscosity	η_b	3.0×10^{-3}	kg $m^{-1}s^{-1}$
Inlet blood flow rates	v_0	0.1, 0.2, 0.3	m s^{-1}
Applied magnetic field strength	$\mu_0 H_0$	0.1 – 2.0	T
Weight fraction of material in MDCPs	$x_{fm,p}$	0.4, 0.6, 0.8, 1.0	-
Density of materials	$\rho_{fm,p}$	7850[a], 7710[b], 5050[c]	kg m^{-3}
Density of polymer material in MDCPs	$\rho_{pol,p}$	9.5×10^{2}	kg m^{-3}
Saturation magnetization of material in target or MDCPs	$M_{s,s}$ or $M_{fm,p,s}$	1.735×10^{6}[a], 1.397×10^{6}[b], 4.55×10^{5}[c]	A m^{-1}
Target radius	a	26, 62.5	μm
Average radii of MDCPs	R_p	100-3000	nm
Magnetic susceptibility of materials in target or MDCPs at zero magnetic field	$\chi_{s,0}$ or $\chi_{fm,p,0}$	1000[a], 1000[b], 1000[c]	-
Magnetic field strength required for the materials in cylindrical and spherical targets becoming magnetically saturated	$\mu_0 H_s$	1.092[a], 0.880[b], 0.286[c] 0.729[a], 0.587[b], 0.191[c]	T

[a] Materials: a = iron.

[b] Materials: b = SS409.

[c] Materials: c = magnetite.

2.2 Theory

2.2.1 Forces on MDCPs

The equations of motion of the MDCPs are constructed by considering the influences of the dominant magnetic and fluid drag forces on the MDCP. The other forces and effects, such as gravitational force, diffusion process and collision process, are negligible. Then, force balance equation is expressed as [4, 7, 14, 18, 20, 23]:

$$\boldsymbol{F}_m + \boldsymbol{F}_d = \boldsymbol{F}_i, \tag{2.1}$$

where $\boldsymbol{F}_m$, $\boldsymbol{F}_d$ and $\boldsymbol{F}_i$ represent the magnetic, drag and inertial forces acting on the MDCPs, respectively. The inertial force is negligible for the capture of small magnetic particles in the bloodstream, hence, Eq. (2.1) can be written as [4, 7, 14, 18, 20, 23]:

$$\boldsymbol{F}_m + \boldsymbol{F}_d = 0. \tag{2.2}$$

The magnetic force acting on the considered ferromagnetic MDCPs is as follows [20, 23]:

$$\boldsymbol{F}_m = \frac{1}{2} V_p \mu_0 \omega_{fm,p} \nabla \left(\boldsymbol{M}_{fm,p} \cdot \boldsymbol{H} \right), \tag{2.3}$$

where V_p is an average volume of the MDCPs, μ_0 is the magnetic permeability of free space, $\omega_{fm,p}$ is the volume fraction occupied by the ferromagnetic material inside the MDCPs, $\boldsymbol{M}_{fm,p}$ is the induced magnetization of the MDCPs, and $\boldsymbol{H}$ is the local magnetic field at the particle position around the magnetized ferromagnetic spherical target subjected to a uniform external magnetic field $\left(\boldsymbol{H}_0\right)$.

The volume fraction of the ferromagnetic material $\left(\omega_{fm,p}\right)$ inside the MDCPs is related to the weight fraction of ferromagnetic material inside the MDCPs $\left(x_{fm,p}\right)$. It can be shown as:

$$\omega_{fm,p} = \rho_p \frac{x_{fm,p}}{\rho_{fm,p}}, \tag{2.4}$$

and

$$\rho_p = \frac{1}{\frac{x_{fm,p}}{\rho_{fm,p}} + \frac{1-x_{fm,p}}{\rho_{pol,p}}}, \tag{2.5}$$

where ρ_p represents the average density of the MDCPs. The $\rho_{fm,p}$ and $\rho_{pol,p}$ are the density of the ferromagnetic material inside a MDCP and the density of both the polymer and drug in a MDCP, respectively.

The Stokes drag force $\left(\boldsymbol{F}_d\right)$ exerted on the MDCPs is defined as

$$\boldsymbol{F}_d = 6\pi\eta_b R_p \left(\boldsymbol{v}_b - \boldsymbol{v}_p\right), \tag{2.6}$$

where $\boldsymbol{v}_b$ and $\boldsymbol{v}_p$ are the blood flow and particle velocities, R_p is the average radius of MDCPs and η_b is the viscosity of the blood.

2.2.2 Blood Flow Velocity

We focuses on IA-MDT in arteries where the blood flow passing the target is dominated by the potential flow regime. It is assumed that the blood flow profile is not affected by the vessel wall [23, 25]. The blood flow velocity $\left(\boldsymbol{v}_b\right)$ can be solved analytically using Laplace's equation which is obtained from the continuity equation and irrotational flow condition as shown below.

The fluid flow field satisfies continuity equation in the case of incompressible flow,

$$\nabla \cdot \boldsymbol{v}_b = 0, \tag{2.7}$$

and for irrotational flow condition,

$$\nabla \times \boldsymbol{v}_b = 0, \tag{2.8}$$

or

$$\boldsymbol{v}_b = -\nabla \varphi, \tag{2.9}$$

where φ is the potential function. Then, the Laplace's equation is obtained by using Eqs. (2.7) and (2.9),

$$\nabla^2 \varphi = 0. \tag{2.10}$$

The slip boundary condition, which the normal component of blood velocity vanishes, is applied on the target-blood interface. Uniform blood velocity is used as an inlet boundary condition and the blood flow are not affected by the vessel wall. Hence, the $\boldsymbol{v}_b$ around a spherical target was reported as follows [49, 50]:

$$\boldsymbol{v}_{\mathrm{b}} = v_0\left(1-\frac{1}{r_a^3}\right)\cos\theta\,\hat{\boldsymbol{r}} + v_0\left(1+\frac{1}{2r_a^3}\right)\sin\theta\,\hat{\boldsymbol{\theta}}, \quad r_{\mathrm{a}} = r/a \tag{2.11}$$

where $\hat{\boldsymbol{r}}$ and $\hat{\boldsymbol{\theta}}$ are unit vectors in spherical coordinates and v_0 is the magnitude of the uniform inlet blood flow velocity $(\boldsymbol{v}_0)$ as shown in Fig. 2.1.

2.2.3 Equations of Motion of MDCPs

By substituting the magnetic force $\left(\boldsymbol{F}_m\right)$ and the drag force $\left(\boldsymbol{F}_d\right)$ from Eqs. (2.3) and (2.6) into Eq. (2.2) and assuming that the MDCPs are spherical with volume $V_p = 4\pi R_p^3/3$, the particle velocity $\left(\boldsymbol{v}_p\right)$ is obtained as follows:

$$\boldsymbol{v}_p = \boldsymbol{v}_b + \frac{1}{9}\frac{\mu_0 \omega_{fm,p} R_p^2}{\eta_b}\nabla\left(\boldsymbol{M}_{fm,p}\cdot\boldsymbol{H}\right). \tag{2.12}$$

The magnetization of the MDCPs $\left(\boldsymbol{M}_{fm,p}\right)$ is related to the local magnetic field $\left(\boldsymbol{H}\right)$ as given by [14, 18, 20, 23]:

$$\boldsymbol{M}_{fm,p} = 3\alpha_{fm,p}\boldsymbol{H}, \tag{2.13}$$

where $\alpha_{fm,p}$ is the demagnetization factor of the ferromagnetic material within MDCPs. If the ferromagnetic material contained in MDCPs is not magnetically saturated, $\alpha_{fm,p} = \chi_{fm,p,0}/\left(3+\chi_{fm,p,0}\right)$, and $\boldsymbol{M}_{fm,p}$ is linearly proportional to $\boldsymbol{H}$. $\chi_{fm,p,0}$ is the magnetic susceptibility of the ferromagnetic material in the MDCPs at zero magnetic field. When the external magnetic field is high enough, the ferromagnetic material inside the spherical MDCPs becomes magnetically saturated with $\alpha_{fm,p} = M_{fm,p,s}/3H$, where $M_{fm,p,s}$ represents the saturation magnetization and $\boldsymbol{M}_{fm,p} = M_{fm,p,s}\hat{\boldsymbol{H}}$.

The local magnetic field strength at any position around the magnetized spherical target is obtained from the familiar two-dimensional result with azimuthal symmetry [49] by using the coordinate transformation [51]:

$$H = H_0\left[1+\left(\frac{K_s^2}{r_a^6}-\frac{2K_s}{r_a^3}\right)+\left(\frac{K_s^2}{r_a^6}+\frac{2K_s}{r_a^3}\right)\left(3\sin^2\theta\cos^2\varphi\right)\right]^{\frac{1}{2}}, \tag{2.14}$$

where $K_s = \chi_{s,0}/\left(3+\chi_{s,0}\right)$ when the ferromagnetic material contained in the target is not magnetically saturated and $K_s = M_{s,s}/3H_0$ when it is magnetically saturated. $\chi_{s,0}$ and $M_{s,s}$ represent the magnetic susceptibility of the ferromagnetic material in

the target at zero magnetic field and the saturation magnetization of the ferromagnetic material in the target, respectively.

When the magnetization of the MDCPs is not magnetically saturated, the equations of motion of the MDCPs are obtained by substituting $\boldsymbol{v}_b$ from Eq. (2.11) into Eq. (2.13) and using Eqs. (2.12) and (2.14), as follows:

$$\frac{dr_a}{dt} = v_{0a}\left(1-\frac{1}{r_a^3}\right)\cos\theta - \frac{\alpha_{fm,p}V_{ma}}{r_a^4}\left[3\left(\frac{K_s}{r_a^3}+1\right)\sin^2\theta\cos^2\varphi + \left(\frac{K_s}{r_a^3}-1\right)\right], \quad (2.15)$$

$$\frac{d\theta}{dt} = -\frac{v_{0a}}{r_a}\left(1+\frac{1}{2r_a^3}\right)\sin\theta + \frac{\alpha_{fm,p}V_{ma}}{r_a^5}\left(1+\frac{K_s}{2r_a^3}\right)\sin 2\theta\cos^2\varphi, \quad (2.16)$$

$$\frac{d\varphi}{dt} = -\frac{\alpha_{fm,p}V_{ma}}{r_a^5}\left(1+\frac{K_s}{2r_a^3}\right)\sin 2\varphi, \quad (2.17)$$

where $v_{0a} = v_0/a$, and $V_{ma} = \dfrac{2R_p^2\omega_{fm,p}K_s\mu_0H_0^2}{3\eta_b a^2}$ is defined as magnetic velocity.

To determine the trajectories of the MDCPs, Eqs. (2.15) - (2.17) are integrated numerically by using the forth-order Runge-Kutta method. The results are analyzed in order to obtain the capture distances then the capture area is determined by numerical integration based on the capture distances.

2.3 Results and Discussions

2.3.1 The New Correlation and Trajectory Analysis Methods for the Capture of MDCPs by Iron Cylindrical Target

The work of Chen et al. [25] was reproduced in order to compare the capture distances obtained by using the new correlation [46], as shown in Appendix A, with the results of this work which used the trajectory analysis method for the capture of MDCPs in arteries by an implanted ferromagnetic cylindrical target. The results based on the

particle trajectories analysis method simulated from the equations of motion, Eqs. (B3) and (B4), are shown in Figs. 2.2 and 2.3 for a single cylindrical target in transverse mode in which a uniform externally applied field and inlet blood flow of potential flow are perpendicular. The effect of the inlet blood flow rate (v_0) on the capture distance divided by the cylindrical target radius (R_c) for the capture of MDCPs by iron cylindrical target of radius 62.5 μm with varying the strength of an externally applied magnetic field ($\mu_0 H_0$) are shown in Fig 2.2. The results using the new correlation and trajectory analysis methods are in good agreement for small R_c, however, for R_c of larger than 4, both results deviate slightly with the discrepancy of less than 4.3% when the $\mu_0 H_0$ is equal to 2.0 T. Ebner and Ritter [46] also reported similar results for the capture of paramagnetic particles of micron size. The deviation was explained by the new correlation method based on the initial positions of the MDCPs, which are not far enough from the target and thus subjected to the influence of the magnetic force [46]. According to the trajectory model, the MDCPs initially move parallel to the blood inlet velocity, where there is no magnetic force. In general, the results of this chapter confirm the reported results of Chen et al. [25], and these also justify the simulation results.

In Fig. 2.2, an increment of R_c by increasing $\mu_0 H_0$ from 0.2 to 0.5 T is larger when compared to that by increasing $\mu_0 H_0$ from 0.5 to 0.8 T even though the difference in the increment of $\mu_0 H_0$ is equal, which is 0.3 T. An increment of R_c decreases after the iron MDCPs reach magnetically saturated at 0.73 T, which is in the range of 0.5-0.8 T. Moreover, increasing $\mu_0 H_0$ from 0.8 to 1.0 T provides an increment of R_c larger than increasing $\mu_0 H_0$ from 1.0 to 2.0 T, even when the ranges of increasing $\mu_0 H_0$ are greatly different, which are 0.2 and 1.0 T, respectively. This is due to the magnetization saturation of the iron cylindrical target, in which the iron is magnetically saturated at 1.1 T.

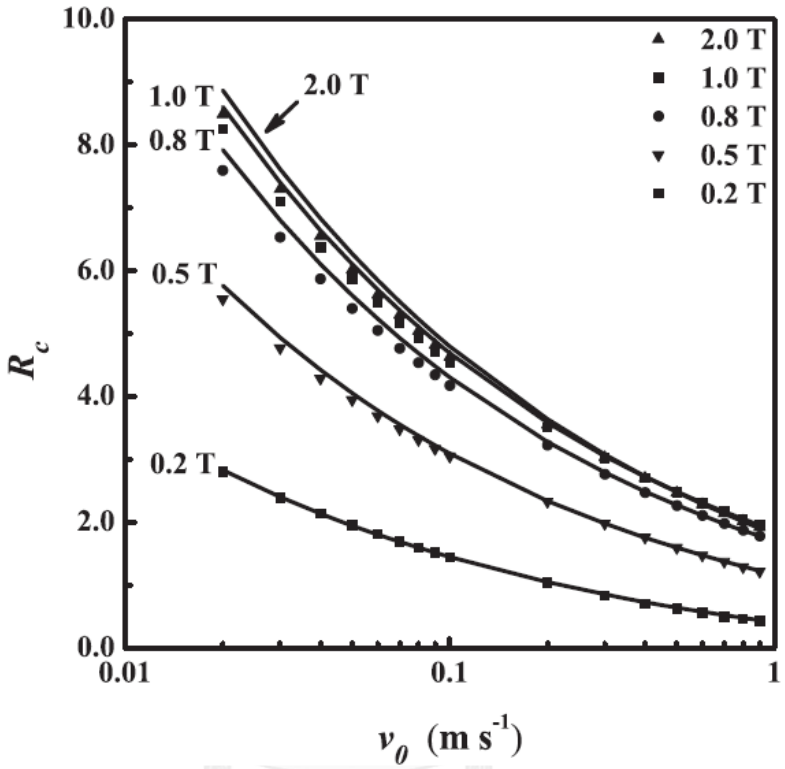

Figure 2.2 Effect of inlet blood flow rate on the dimensionless capture distance (R_c) of MDCPs consisting of iron with 100% weight fraction an average radius of 1 μm and a cylindrical iron target of radius 62.5 μm with an externally applied magnetic field strength $(\mu_0 H_0)$ as parameter. The data points and solid lines represent the simulated results from trajectory analysis and new correlation methods, respectively. The other parameters are given in Table 2.1.

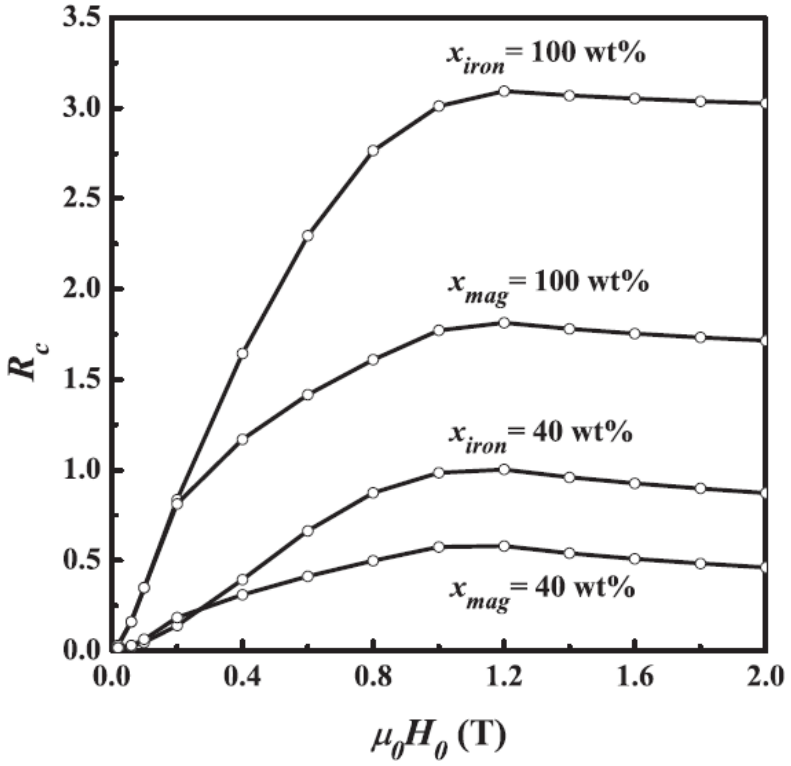

Figure 2.3 Effect of externally applied magnetic field strength $\left(\mu_0 H_0\right)$ on the dimensionless capture distance $\left(R_c\right)$ of MDCPs with an average radius of 1 μm consisting different amounts of iron or magnetite and a cylindrical iron target of radius 62.5 μm, implanted in the vessel with the blood flow rate $\left(v_0\right)$ of 0.3 ms^{-1}. The other parameters are given in Table 2.1.

2.3.2 The Capture Distances for the Capture of MDCPs by the Ferromagnetic Targets

The R_c determined by using the trajectory analysis method for varying $\mu_0 H_0$ are shown in Fig. 2.3. The results revealed that R_c increases with an increase in $\mu_0 H_0$ until the ferromagnetic material in the MDCPs are magnetically saturated which the magnetic field strength required $(\mu_0 H_s)$ for the spherical MDCPs made of iron and magnetite becoming magnetically saturated were 0.73 and 0.19 T, respectively. For the MDCPs and target both made of iron, the R_c increased with less slope after saturation magnetization of the MDCPs which occurred at $\mu_0 H_0$ about 0.8 T. Then it began to decrease slightly at $\mu_0 H_0$ about 1.2 T near the value of $\mu_0 H_s$ = 1.1 T for iron cylindrical target. For MDCPs made of magnetite, the R_c increased with less slope at $\mu_0 H_0$ larger than 0.2 T after the magnetization saturation of the magnetite MDCPs is reached, then it began to decrease slightly at $\mu_0 H_0$ about 1.2 T after the magnetization of iron in the cylindrical target is also reached. These behaviors can be explained by analyzing the effect of varying H_0 on the magnetic term in Eq. (B3). Before the ferromagnetic materials in both target and MDCPs become magnetically saturated, both K_w and $\alpha_{fm,p}$ are independent of H_0. Therefore, the magnetic term in Eq. (B3) is proportional to H_0^2, resulting in a pronounced increase of R_c. After only the ferromagnetic material in the MDCPs are magnetically saturated, $\alpha_{fm,p}$ is proportional to H_0^{-1}, and the magnetic term in Eq. (B3) is proportional to H_0^{-1} resulting in a lower slope of R_c. After the ferromagnetic materials in both the target and MDCPs reach magnetically saturated, both K_s and $\alpha_{fm,p}$ are proportional to H_0^{-1}, resulting in the slight decrease in R_c with increasing $\mu_0 H_0$.

The effect of external magnetic field strength $(\mu_0 H_0)$ on capture distance (R_c) of MDCPs containing different amounts of iron or magnetite for IA-MDT using spherical targets are shown in Fig. 2.4. The R_c was obtained from the numerical integration of Eqs. (2.15) - (2.17) in the main symmetry plane ($\varphi = 0$ in Fig. 3.1), where the R_c is largest compared to those of other planes [49]. The maxima of R_c are

reached when the ferromagnetic materials in MDCPs are magnetically saturated, caused by the magnetic terms in Eqs. (2.15) - (2.17) being reduced by a factor of one-half, as seen by Eqs. (2.18) – (2.20). This behavior is only shown in 3-D result not in the 2-D result of Fig. 2.3. Furthermore, the results indicate that the maximum R_c required $\mu_0 H_0$ of about 0.6 T for the spherical target, which is less than that of about 1.2 T for the cylindrical target results in Fig. 2.3. For MDCPs made of magnetite, R_c increases with the largest slope before saturation magnetization of the MDCPs occur at $\mu_0 H_0$ of about 0.1 T. Then, a small drop of R_c occurs for both 40 and 100 % weight fractions. After that, R_c continues to increase with a less slope as $\mu_0 H_0$ increases until the spherical iron target is magnetically saturated at $\mu_0 H_0$ about 0.8 T. Then, R_c tends to decrease slightly with an increase in $\mu_0 H_0$ due to the saturation magnetization of both target and MDCPs. For MDCPs made of iron, the variation of R_c is similar to that of the magnetite MDCPs. However, the more pronounce drop of the R_c occurs at $\mu_0 H_0$ about 0.4 and 0.6 T for 40 and 100 % weight fractions, respectively. The $\mu_0 H_s$ for MDCPs made of magnetite and iron are 0.19 and 0.73 T, respectively. It can be seen that the maxima of R_c occur at the values of $\mu_0 H_0$ smaller than the values of $\mu_0 H_s$, because the local magnetic field strength $(\mu_0 H)$ at the particle positions are larger than the uniform externally applied magnetic field $(\mu_0 H_0)$, especially when they are near the spherical target surfaces.

The three levels of variation in R_c slope due to the saturation magnetization of the MDCPs and target, can be explained by analyzing the magnetic term in Eq. (2.15) based on the K_s and $\alpha_{fm,p}$ similar to Fig. 2.3. The only difference is that now $\alpha_{fm,p}$ depends on local magnetic field H instead of applied magnetic field H_0 as in the explanation of Fig. 2.3. Before the ferromagnetic materials in both the target and MDCPs became magnetically saturated, the magnetic term in Eq. (2.15) is proportional to H_0^2 because both K_s and $\alpha_{fm,p}$ are independent of H_0, resulting in a pronounced increase in R_c with increasing $\mu_0 H_0$. When only the ferromagnetic material in the MDCPs became magnetically saturated, the magnetic term in Eq. (2.15) is proportional to H_0^2/H, because $\alpha_{fm,p}$ is proportional to H^{-1}, resulting in a lower increase in R_c. After the ferromagnetic materials in both the target and MDCPs became magnetically

saturated, the magnetic term in Eq. (2.15) was proportional to H^{-1} because K_s and $\alpha_{fm,p}$ were proportional to H_0^{-1} and H^{-1}, respectively, resulting in the slight decrease in R_c.

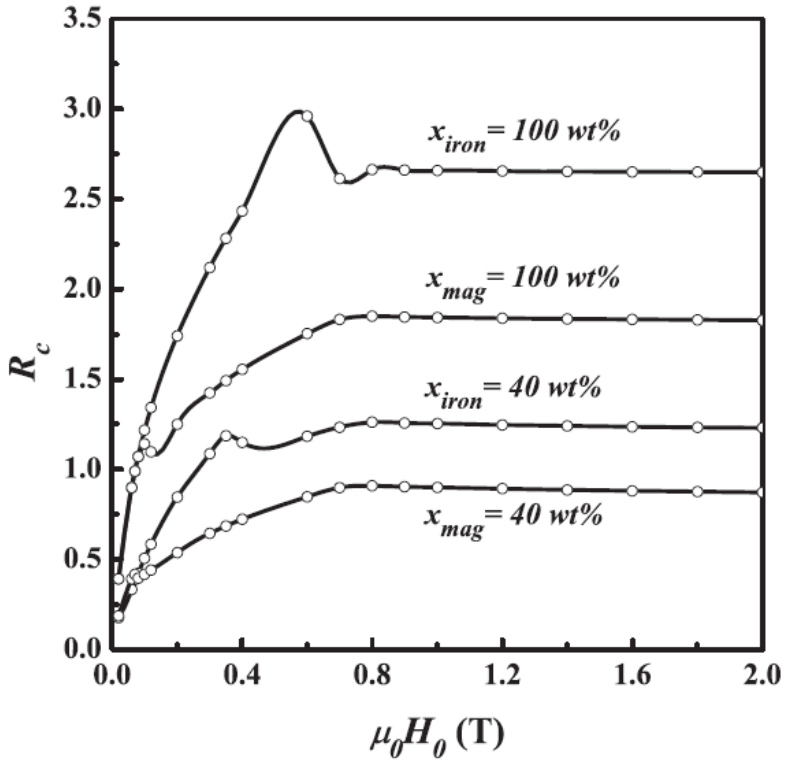

Figure 2.4 Effect of externally applied magnetic field strength $(\mu_0 H_0)$ on the dimensionless capture distance (R_c) of MDCPs with an average radius of 1 μm consisting different amounts of iron or magnetite that are captured by a spherical target, made of iron with average radius 62.5 μm, implanted in the vessel with the blood flow rate (v_0) of 0.3 ms^{-1}. The other parameters are given in Table 2.1.

2.3.3 The Capture Areas for the Capture of MDCPs by Spherical Ferromagnetic Target

The effect of MDCP size on the dimensionless capture area (A_s), which is equal to the capture area divided by the target cross-section area are shown in Figs. 2.5 (a)-(c) for three types of ferromagnetic materials in the target and MDCPs: (a) iron and iron, (b) iron and magnetite, and (c) SS409 and magnetite, respectively. The 3-D model in this chapter yields a kidney-shaped capture area which can be seen in Fig. 3.3 of Chapter III. This has also been demonstrated by Friedlaender et al. [49]. The general behaviors of A_s, which increases monotonically with an increase in R_p, are also shown. The A_s increases with an increase in $\mu_0 H_0$ until the ferromagnetic materials in MDCPs and target become magnetization saturation. Then, the A_s reduces as also shown in Figs. 2.3 and 2.4. However, the reduction in A_s with an increase in $\mu_0 H_0$ above $\mu_0 H_0$ of 0.6 T does not clearly shown for R_p of less than 300 nm, where the magnetic force is weak. The results of the A_s for the targets and MDCPs, both made of iron which the saturation magnetization is largest compared to others, as seen in Fig. 2.5(a), are larger than those of Figs. 2.5(b) and (c), as expected.

In Fig. 2.5(a), the maximum A_s occurs at $\mu_0 H_0$ of about 0.6 T. The saturation magnetization of the iron within MDCPs is reached when the local magnetic field strength $(\mu_0 H)$ is equal to $\mu_0 H_s$ of 0.73 T. However, this requires the $\mu_0 H_0$ only about 0.6 T because the strength of the local magnetic field is larger than the externally uniform applied magnetic field, as noted in the explanation of Fig. 2.4.

In Fig. 2.5(b), the maximum A_s occurs at $\mu_0 H_0$ about 0.8 T when both the iron in the target and magnetite in MDCPs are magnetically saturated. The saturation magnetization of ferromagnetic material in the target depends on the externally applied magnetic field (H_0) instead of the local field strength (H). The saturation magnetization of the ferromagnetic material in the target occurs at $\mu_0 H_s$ equal to $\mu_0 H_0$ according to $\boldsymbol{M}_s = 3K_s \boldsymbol{H}_0$, where $\boldsymbol{M}_s$ is the magnetization of the material in target, in contradiction to that for the MDCPs with $\mu_0 H_s$ equal to $\mu_0 H$ according to

$\boldsymbol{M}_{fm,p} = 3\alpha_{fm,p}\boldsymbol{H}$. Therefore, the maximum A_s occurs at $\mu_0 H_0$ of about 0.8 T, which is close to the value of $\mu_0 H_s$ = 0.73 T for the iron target.

In Fig. 2.5(c), the maximum A_s occurs at $\mu_0 H_0$ of about 0.6 T, close to the value of $\mu_0 H_s$ which is 0.59 T for the spherical SS409 target. The result is similar to that in Fig. 2.5(b) because the saturation magnetization of the ferromagnetic material in the SS409 targets is larger than that of the magnetite MDCPs.

It should be noted that the maximum reported capture areas are less than the blood vessel cross section. The A_s close to the vessel cross section corresponds to capture efficiency approaching 100%. The capture efficiency is defined by the percentage of MDCPs entering the blood vessel that are captured by the target. Therefore, the R_p of less than 1000 μm is large enough for effective targeting.

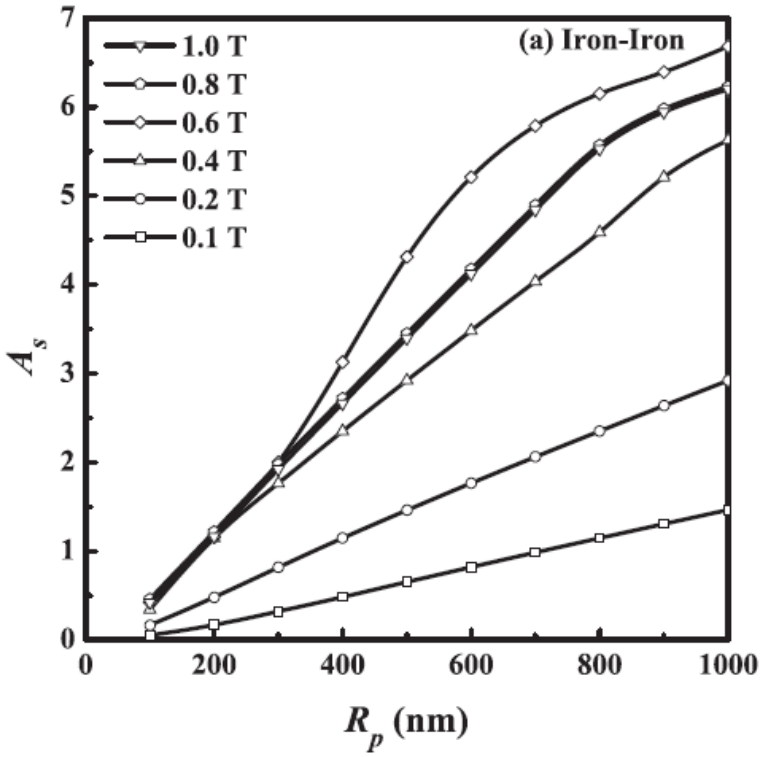

Figure 2.5(a) Effect of MDCP radius $\left(R_p\right)$ on the dimensionless capture area $\left(A_s\right)$ of MDCPs for an inlet blood flow rate $\left(v_0\right)$ of 0.1 ms^{-1} with externally applied magnetic field strength $\left(\mu_0 H_0\right)$ as parameter. The type of ferromagnetic materials in the target and MDCPs is iron and iron. The spherical target with radius of 26 $\mu\mathrm{m}$ and the MDCPs with 80% weight fraction are used. The other parameters are given in Table 2.1.

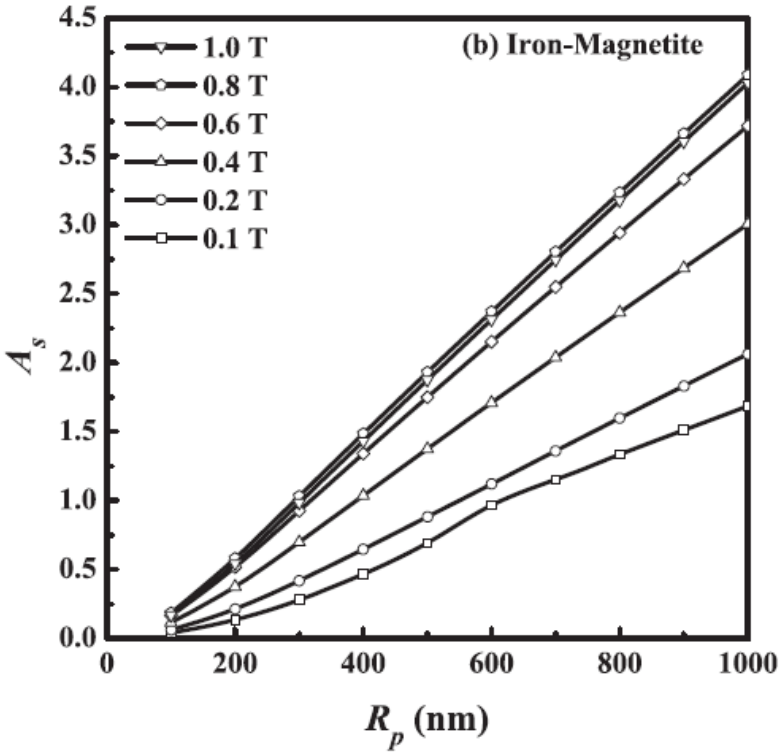

Figure 2.5(b) Effect of MDCP radius $\left(R_p\right)$ on the dimensionless capture area $\left(A_s\right)$ of MDCPs for an inlet blood flow rate $\left(v_0\right)$ of 0.1 ms^{-1} with externally applied magnetic field strength $\left(\mu_0 H_0\right)$ as parameter. The types of ferromagnetic materials in the target and MDCPs is iron and magnetite. The spherical target with radius of 26 $\mu\mathrm{m}$ and the MDCPs with 80% weight fraction are used. The other parameters are given in Table 2.1.

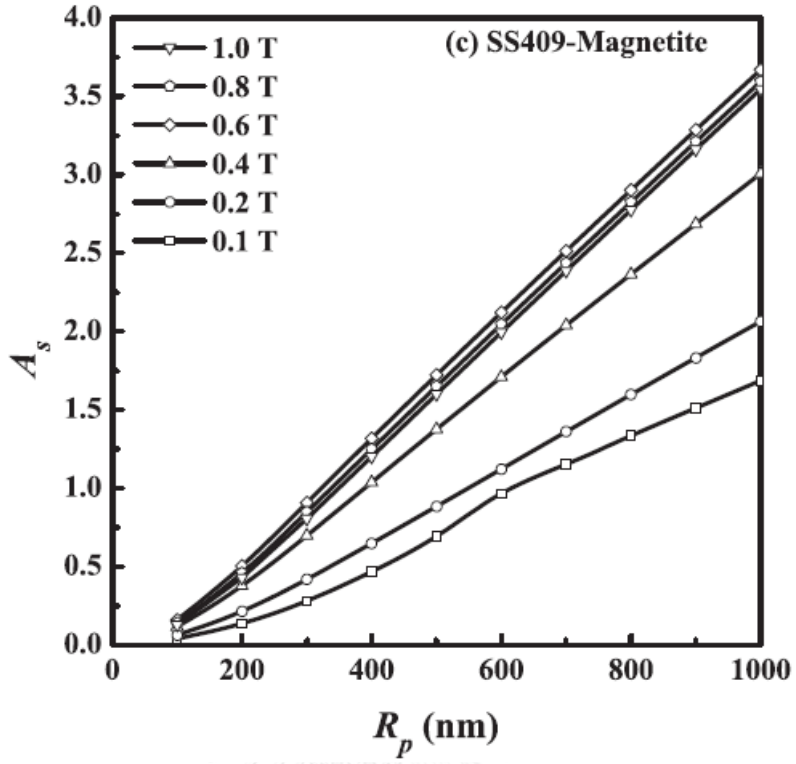

Figure 2.5(c) Effect of MDCP radius $\left(R_p\right)$ on the dimensionless capture area $\left(A_s\right)$ of MDCPs for an inlet blood flow rate $\left(v_0\right)$ of 0.1 ms^{-1} with externally applied magnetic field strength $\left(\mu_0 H_0\right)$ as parameter. The types of ferromagnetic materials in the target and MDCPs is SS409 and magnetite. The spherical target with radius of 26 $\mu\mathrm{m}$ and the MDCPs with 80% weight fraction are used. The other parameters are given in Table 2.1.

2.3.4 The Effects of MDCP Size on the Maximum Capture Areas

The effects of MDCP size on the maximum dimensionless capture area $\left(A_{s,\max}\right)$ for four types of targets and MDCPs are shown in Fig. 2.6, where $A_{s,\max}$ represents the maximum value of the dimensionless capture area (A_s), determined by varying the external magnetic field strength ($\mu_0 H_0$). With these results, the prediction of the appropriate MDCP sizes for the required capture areas or capture efficiencies can be obtained. For example, if the required effectiveness of IA-MDT is equivalent to $A_{s,\max}$ of 3 then MDCPs with an average radii of about 400, 600, 800 and 900 nm are suggested

for the targets and MDCPs types of (a), (b), (c) and (d), respectively. Note that $A_{s,max}$ of 3 and 7 correspond to the particle capture efficiencies 36% and 84%, respectively. Therefore, the corresponding appropriate MDCP sizes are less than 1000, 1500, 2200 and 2500 nm for IA-MDT types (a), (b), (c) and (d), respectively. This study only reports the values of $A_{s,max}$ smaller than 7 that are less than the dimensionless vessel cross-section area, which is about 8 for the blood flow rate that equals to 0.1 $\mathrm{m\,s^{-1}}$ [52].

Figure. 2.7 shows the effects of MDCP size on $A_{s,max}$ for blood flow rates (v_0) equal to 0.1, 0.2 and 0.3 $\mathrm{m\,s^{-1}}$. $A_{s,max}$ increases with increasing R_p, but, as expected, it decreases with increasing v_0. For v_0 of 0.2 and 0.3 $\mathrm{m\,s^{-1}}$, $A_{s,max}$ for R_p of 3000 nm are much lower than the dimensionless vessel cross-sections which are about 10^4 for blood flow rates of 0.2 and 0.3 $\mathrm{m\,s^{-1}}$ [52], respectively. For v_0 of 0.1 $\mathrm{m\,s^{-1}}$, the MDCPs with an average radius of 2500 nm, corresponding to $A_{s,max}$ of 7 and the capture efficiency of about 84%, was suggested as the optimum R_p as explained in the results shown in the explanation of Fig. 6. However $A_{s,max}$ of 7 corresponds to the very small capture efficiency for v_0 of 0.2 and 0.3 $\mathrm{ms^{-1}}$; therefore, the appropriate R_p for v_0 of 0.2 and 0.3 $\mathrm{ms^{-1}}$ is much larger than 3000 nm.

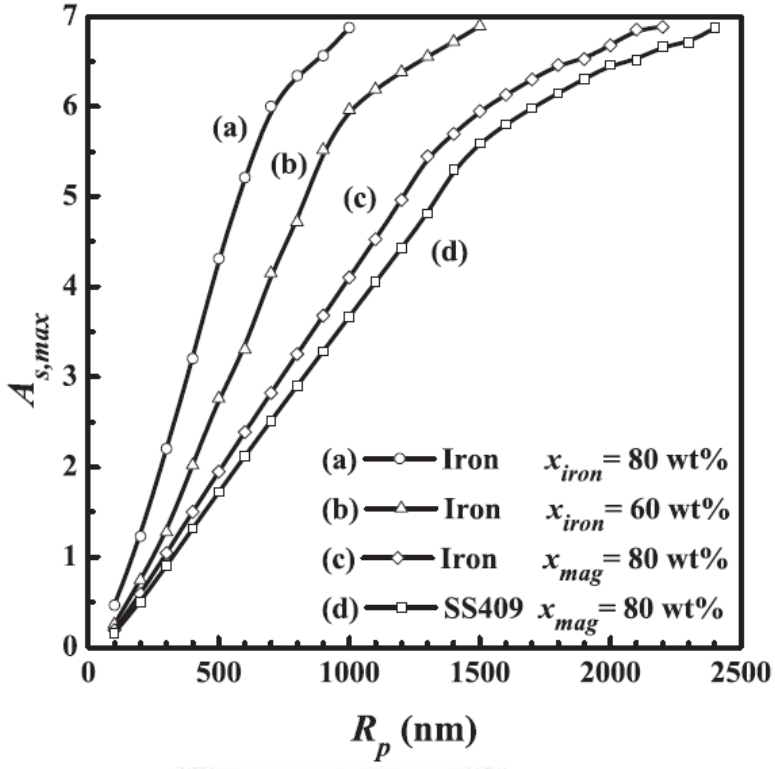

Figure 2.6 Effect of MDCP radius $\left(R_p\right)$ on the maximum dimensionless capture area $\left(A_{\mathrm{s,max}}\right)$ of MDCPs for four types of the target and MDCPs, (a) iron target and iron MDCPs with 80% weight fraction, (b) iron target and iron MDCPs with 60% weight fraction, (c) iron target and magnetite MDCPs with 80% weight fraction and (d) iron SS409 and magnetite MDCPs with 80% weight fraction. The implanted spherical target with radius of 26 $\mu\mathrm{m}$ is in the vessel of inlet blood flow rate $\left(v_0\right)$ of 0.1 ms^{-1}.The other parameters are given in Table 2.1.

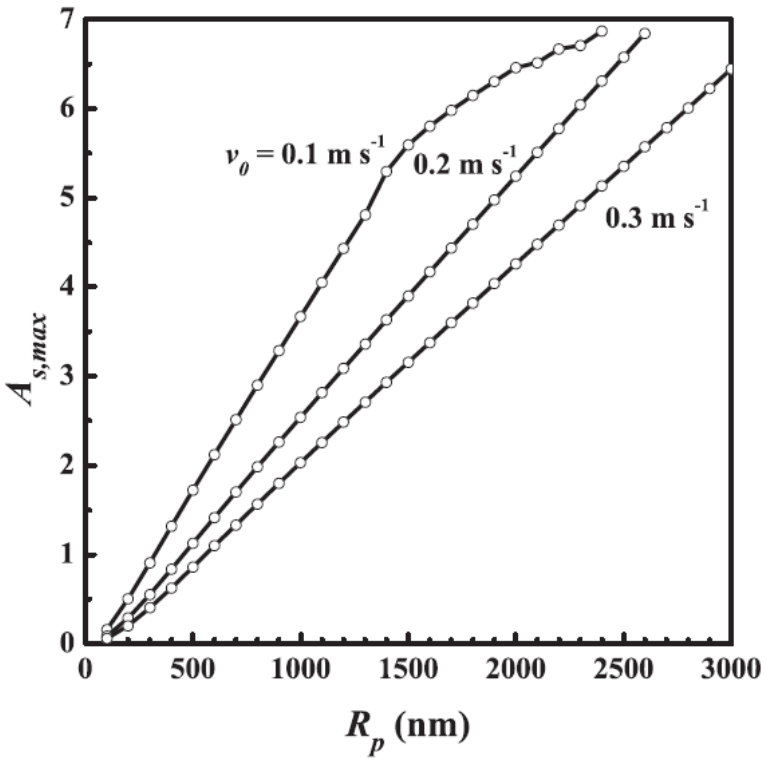

Figure 2.7 Effect of MDCP radius $\left(R_p\right)$ on the maximum dimensionless capture area $\left(A_{\mathrm{s,max}}\right)$ of MDCPs consisting of magnetite with 80% weight fraction that are captured by a spherical target made of SS409 with radius of 26 $\mu\mathrm{m}$ for an inlet blood flow rates $\left(v_0\right)$ of 0.1, 0.2 and 0.3 ms^{-1}. The other parameters are given in Table 2.1.

2.4 Conclusion

In this chapter, 3-D IA-MDT using dilute spherical targets has been investigated. The local magnetic field around the magnetized spherical target as shown in Fig. 2.1 does not have azimuthal symmetry therefore 3-D modelling was used to obtain 3-D particle trajectories depending on the angle of φ. The equations of motion of MDCPs were derived based on the magnetic field and blood velocity around a single spherical target implanted within large blood vessel. The blood flow is categorized by potential flow regime which the effect from the vessel wall is assumed to be negligible, and only the magnetic and hydrodynamic drag forces are the dominant forces acting on the MDCPs. The particle trajectories were simulated based on the equations of motion using the flow chart as shown in the Appendix B [9].

The capture distances were firstly compared with those of previously published works [25, 46] as shown in Figs. 2.2 and 2.3 in order to validate the computational program used in this work. Then, the capture areas of the 3-D IA-MDT were numerically integrated and reported with parameters such as blood flow rates, types of ferromagnetic materials within target and MDCPs, externally uniform applied magnetic field strength, the weight fraction of the ferromagnetic materials in MDCPs and their radii. The simulation results in Fig. 2.4 reveal the different levels of variation of capture distance for varying externally applied magnetic field strengths $\left(\mu_0 H_0\right)$ described by the analysis of the physical effects of magnetization saturation of ferromagnetic materials within MDCPs and targets. Figs. 2.5(a) and (b) reveal that the capture area was substantially reduced by about 40%, when the iron in the MDCPs was replaced by magnetite. While the capture area was only slightly reduced by only 11%, as shown in Figs. 2.5(b) and (c), when the ferromagnetic material in target material was changed from iron to SS409. The use of magnetite MDCPs is a good choice because it is biocompatible and inexpensive. In addition, SS409, which has a high corrosion resistance compared to iron, is more suitable to use than iron as a ferromagnetic material in the targets because the implanted targets must be corrosion resistant for use within blood vessels. The dimensionless capture areas ranging from 2 to 7, were obtained with R_p ranging from 500 to 2500 nm, $\mu_0 H_0$ less than 0.8 T and a blood flow rate of 0.1 ms^{-1}. For blood flow rates of 0.2 and 0.3 $\mathrm{m\,s^{-1}}$, an increase in R_p above 3000 nm provided a larger capture areas and resulted in a more effective IA-MDT system. The target-MDCP materials used are iron-iron, iron-magnetite and SS409-magnetite, respectively. The use of large MDCP sizes could irritate the surrounding tissues, cause thrombosis or embolism in blood vessels and decrease diffusion ability, all of which can affect the distribution of a drug concentration. The results of 3-D IA-MDT in this chapter yield the predictions of MDCP sizes that are appropriate for various designs of IA-MDT systems and could be used for estimating drug dosage in medical treatment

CHAPTER III

THREE-DIMENSIONAL MAGNETIC DRUG TARGETING WITH SPHERICAL TARGET BY BILINIEAR INTERPOLATION FOR DETERMINING THE BLOOD VELOCITY PROFILES

In this chapter, we study the capture of MDCPs by the spherical ferromagnetic targets in 3-D IA-MDT with including the effect from the vessel wall. The dilute spherical targets are implanted within the blood vessels in the size of arterioles. An external uniform magnetic field is applied, perpendicular to inlet blood flow direction, to magnetize the target in order to create the high gradient magnetic field. In this work, the single sphere model is used to determine the magnetic and blood flow fields around the spherical target. The blood flow in the vessel is categorized into laminar flow which the effect from the vessel wall is considered. Then, the blood velocity is obtained by applying bilinear interpolation to the numerical blood flow. The capture areas are determined from the analysis of the particle trajectories simulated from the equations of motion. The 3-D particle trajectories and the capture areas of the MDCPs are shown and the behaviors of MDCPs under the influence magnetic and hydrodynamic drag forces are explained. The effects of externally applied magnetic field strength on the capture area with varying the target-MDCP materials and MDCP size are investigated and the physical effects of magnetization saturation of ferromagnetic materials within MDCPs and targets are analyzed. We also report the effects of MDCP size on the capture areas with varying types of the ferromagnetic materials in targets and MDCPs, weigh fractions of the ferromagnetic materials in MDCPs and average blood flow rates.

3.1 Problem Definition

In this research, the IA-MDT system consists of three main components: (i) the dilute ferromagnetic micro-spheres implanted within a certain length of a blood vessel, (ii) the MDCPs carried by the bloodstream towards the implanted ferromagnetic spherical targets and (iii) an external uniform magnetic field applied across the considered part of the vessel, near the disease site, perpendicular to inlet blood flow direction. This model is similar to the transverse mode of MDT, but without an implanted target, as presented previously [47]. The MDCP is assumed to be a sphere and comprised of ferromagnetic and drug carrier materials. The high gradient magnetic field around the targets creates a strong magnetic force acting on the MDCPs, as explained by the high gradient magnetic separation concept [18, 48]. For the dilute volume packing fraction of the targets in the considered part of the blood vessel, the single sphere model proposes a good approximation for the determination of the magnetic and blood flow fields around the sphere. This work focuses on blood vessels in the size of arterioles which Rotariu and Strachan [17] investigated by using the 2-D MDT with implanting needle magnets. The different types of ferromagnetic materials in the spherical targets and MDCPs (iron, SS409 and magnetite) are considered. Figure 3.1 shows a MDCP of an average radius R_p at the position indicated by the spherical coordinates (r, θ, φ), with the target having an average radius a at the origin, external uniform magnetic field $(\boldsymbol{H}_0)$ in the $\hat{\boldsymbol{x}}$ direction and inlet blood flow velocity in the $-\hat{\boldsymbol{z}}$ direction with an average rate of v_{avg}.

To avoid irritation of the surrounding tissue and embolism in small blood vessels, this study considers MDCPs with an average radii of ≤ 500 nm, as previously suggested [53]. Previously, the IA-MDT system in capillaries considered MDCP sizes in the range of 20-500 nm with spherical implants of an average radii in the range of 100-2000 nm without taking into account the diffusion process [14]. In this chapter, which considers larger vessels, larger MDCP sizes (range of 50 to 500 nm) are considered and so the particle capture by interception is dominant, while the diffusion process is negligible [4, 14]. The target size has to be large enough compared to the size of the MDCPs in order to allow a large retention area on the target surface. Previously, a

target with an average radius of 26 $\mu\mathrm{m}$ was implanted in large blood vessels [9], whereas in this system the radii of the arterioles are about 10 times smaller, and so a target with an average radius of 3 $\mu\mathrm{m}$ is considered as a base value. The target to MDCP size ratio is larger than 6, and so the retention area on the target surface is large enough and that the amount of build-up of MDCPs on the target surface, which reduces the effectiveness of MDT, is not expected to be large enough to adversely affect the system. Other base parameters used in this simulation are the average blood flow rates $\left(v_{avg}\right)$ of 0.01, 0.03 and 0.05 $\mathrm{m\,s^{-1}}$, a blood density $\left(\rho_b\right)$ of 1040 $\mathrm{kg\,m^{-3}}$ and blood viscosity $\left(\eta_b\right)$ of $2.0\times10^{-3}\,\mathrm{kg\,m^{-1}\,s^{-1}}$ [10, 14]. Since the Reynolds number for the blood flow passing the target $\left(\mathrm{Re}=2a\rho_b v_{avg}/\eta_b\right)$ is less than unity, a laminar flow type is applied to the blood flow. The other parameters used in this simulation are given in Table 3.1.

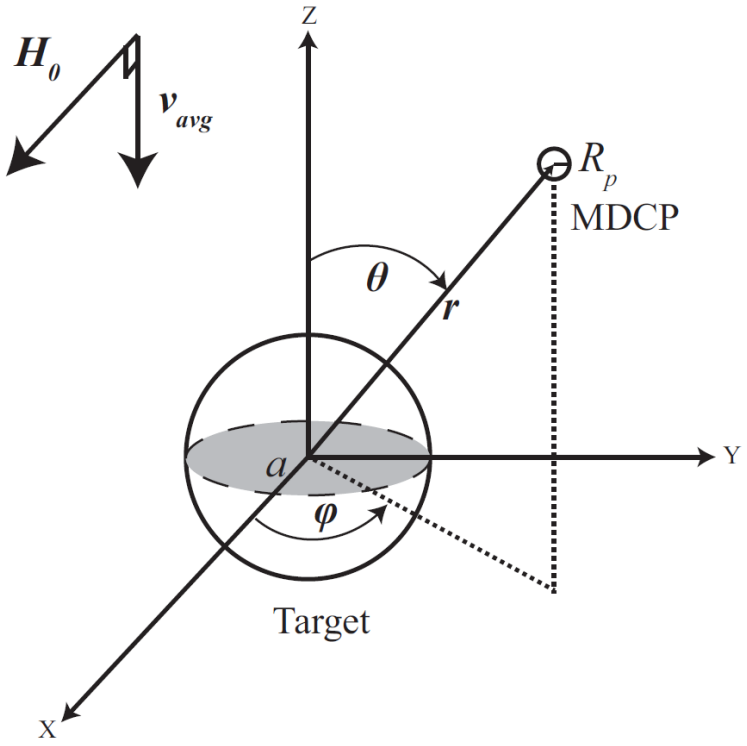

Figure 3.1 A spherical target with radius of a, MDCP with radius R_p, inlet blood velocity in $-\hat{z}$ direction with an average rate of v_{avg} and the external uniform magnetic field (H_0) in the $\hat{x}$ direction are shown.

Table 3.1 The parameters used in this research

Parameters	Symbol	Value(s)	SI Unit
Blood density	ρ_b	1.040×10^{3}	kg m^{-3}
Blood viscosity	η_b	2.0×10^{-3}	kg $m^{-1}s^{-1}$
Inlet average blood flow rates	v_{avg}	0.01, 0.03, 0.05	m s^{-1}
Applied magnetic field strength	$\mu_0 H_0$	0.1 – 2.0	T
Weight fraction of material in MDCPs	$x_{fm,p}$	0.4, 0.6, 0.8	-
Density of materials	$\rho_{fm,p}$	7850[a], 7710[b], 5050[c]	kg m^{-3}
Density of polymer material in MDCPs	$\rho_{pol,p}$	9.5×10^{2}	kg m^{-3}
Saturation magnetization of material in target or MDCPs	$M_{s,s}$ or $M_{fm,p,s}$	1.735×10^{6}[a], 1.397×10^{6}[b], 4.55×10^{5}[c]	A m^{-1}
Target radius	a	26, 62.5	μm
Average radii of MDCPs	R_p	100-3000	nm
Magnetic susceptibility of materials in target or MDCPs at zero magnetic field	$\chi_{s,0}$ or $\chi_{fm,p,0}$	1000[a], 1000[b], 1000[c]	-
Magnetic field strength required for the materials in spherical target becoming magnetically saturated	$\mu_0 H_s$	0.729[a], 0.587[b], 0.191[c]	T

[a] Materials: a = iron.

[b] Materials: b = SS409.

[c] Materials: c = magnetite.

3.2 Theory

3.2.1 Forces on MDCPs

The equations of motion of MDCPs in three dimensions are derived based on the magnetic, fluid drag and initial forces. The force balance on MDCPs as they travel past the magnetized target in the bloodstream, as previously reported in Refs. [4, 7, 14, 18, 20, 23], is shown in Eq. (3.1);

$$\boldsymbol{F}_m + \boldsymbol{F}_d = \boldsymbol{F}_i, \tag{3.1}$$

where $\boldsymbol{F}_m$, $\boldsymbol{F}_d$ and $\boldsymbol{F}_i$ represent the magnetic, drag and inertial forces acting on the MDCPs, respectively. All other forces and effects, such as the gravitational force, diffusion process and collision process are negligible.

The inertial force is neglected for the capture of small magnetic particles in the bloodstream, and so the equations of motion of the MDCPs are created by considering only the influences of the magnetic and fluid drag forces acting on the particle. Therefore, Eq. (3.1) can be written as shown in Eq. (3.2) [4, 7, 14, 18, 20, 23],

$$\boldsymbol{F}_m + \boldsymbol{F}_d = 0. \tag{3.2}$$

The magnetic force acting on the ferromagnetic MDCPs is obtained from Eq. (3.3) [14];

$$\boldsymbol{F}_m = \Omega_{fm,p} V_p \mu_0 \omega_{fm,p} \nabla \left(\boldsymbol{M}_{fm,p} \cdot \boldsymbol{H} \right), \tag{3.3}$$

where V_p is the average volume of the MDCPs, μ_0 is the magnetic permeability of free space, $\omega_{fm,p}$ is the volume fraction occupied by the ferromagnetic material inside the MDCPs, $\boldsymbol{M}_{fm,p}$ is the induced magnetization of the MDCPs, $\boldsymbol{H}$ is the local magnetic field at the particle position around the ferromagnetic target subjected to the external

magnetic field $\boldsymbol{H}_0$, and $\Omega_{fm,p}$ is a delineation factor. When the ferromagnetic material in MDCPs is not magnetically saturated $\Omega_{fm,p}=1/2$, while $\Omega_{fm,p}=1$ when the ferromagnetic material in MDCPs becomes magnetically saturated.

The volume fraction of the ferromagnetic material $\left(\omega_{fm,p}\right)$ in the MDCPs is related to the weight fraction of ferromagnetic material inside the MDCPs $\left(x_{fm,p}\right)$. It can be shown that

$$\omega_{fm,p}=\rho_p\frac{x_{fm,p}}{\rho_{fm,p}}, \tag{3.4}$$

and

$$\rho_p=\frac{1}{\frac{x_{fm,p}}{\rho_{fm,p}}+\frac{1-x_{fm,p}}{\rho_{pol,p}}}, \tag{3.5}$$

where ρ_p represents the average density of the MDCPs, $\rho_{fm,p}$ and $\rho_{pol,p}$ are the density of the ferromagnetic material inside the MDCP and the density of both the polymer and the drug in the MDCP, respectively.

The Stokes drag force $\left(\boldsymbol{F}_d\right)$ acting on the MDCPs is given by Eq. (3.6);

$$\boldsymbol{F}_d=6\pi\eta_b R_p\left(\boldsymbol{v}_b-\boldsymbol{v}_p\right), \tag{3.6}$$

where $\boldsymbol{v}_b$ and $\boldsymbol{v}_p$ are the blood flow and the particle velocities, respectively, R_p is the average radius of the MDCPs and η_b is the viscosity of the blood.

3.2.2 Blood Flow Velocity

This work focuses on the IA-MDT in arterioles, where the blood flow passing the target is considered to be of a laminar flow type. The blood flow velocity $\left(\boldsymbol{v}_b\right)$ satisfies the continuity equation for an incompressible fluid, shown in Eq. (3.7),

$$\nabla \cdot \boldsymbol{v}_b = 0, \tag{3.7}$$

and the Navier-Stokes equation for a Newtonian fluid at steady state, shown in Eq. (3.8),

$$\rho_b \left[\left(\boldsymbol{v}_b \cdot \nabla \right) \boldsymbol{v}_b \right] = -\nabla P + \eta_b \nabla^2 \boldsymbol{v}_b, \tag{3.8}$$

where ρ_b and P are the density and pressure of the blood, respectively.

In order to determine the $\boldsymbol{v}_b$, both Eqs. (3.7) and (3.8) were solved numerically using the CFD software with no-slip boundary conditions, where both the perpendicular and parallel components of blood flow velocity at the target surface and vessel wall vanished. The blood vessel is assumed to be cylindrical and the blood in a laminar flow parallel to the axis of the blood vessel at far away from the target. Then, the parabolic flow velocity, $2\boldsymbol{v}_{avg}\left(1-\left(x^2+y^2\right)/R_v^{\,2}\right)$, was used as an inlet boundary condition [31, 47], where $\boldsymbol{v}_{avg}$ and R_v are the inlet average blood flow velocity in the $-\hat{\boldsymbol{z}}$ direction and the vessel radius, respectively. Because the blood flow within the cylindrical vessel does not has uniform velocity distribution then the average blood velocity $\left(\boldsymbol{v}_{avg}\right)$ is used as parameter in the parabolic profile instead of normal inlet blood velocity which depends on radius of the vessel.

3.2.3 Equations of Motion of MDCPs

By substituting the magnetic force $\left(\boldsymbol{F}_m\right)$ and the drag force $\left(\boldsymbol{F}_d\right)$ from Eqs. (3.3) and (3.6) into Eq. (3.2), and assuming that the MDCPs are spherical with a volume $V_p = 4\pi R_p^3/3$. Then, the particle velocity $\left(\boldsymbol{v}_p\right)$ is obtained from Eq. (3.10),

$$\boldsymbol{v}_p = \boldsymbol{v}_b + \frac{2}{9}\frac{\Omega_{fm,p}\mu_0\omega_{fm,p}R_p^2}{\eta_b}\nabla\left(\boldsymbol{M}_{fm,p}\cdot\boldsymbol{H}\right). \tag{3.9}$$

The magnetization of the MDCPs $\left(\boldsymbol{M}_{fm,p}\right)$ is related to the local magnetic field $\left(\boldsymbol{H}\right)$ as given by Eq. (3.11) [14, 18, 20, 23];

$$\boldsymbol{M}_{fm,p} = 3\alpha_{fm,p}\boldsymbol{H}, \tag{3.10}$$

where $\alpha_{fm,p}$ is the demagnetization factor of the ferromagnetic material within MDCPs. If the ferromagnetic material contained in MDCPs is not magnetically saturated, $\alpha_{fm,p} = \chi_{fm,p,0}/\left(3+\chi_{fm,p,0}\right)$ and $\boldsymbol{M}_{fm,p}$ is linearly proportional to $\boldsymbol{H}$, where $\chi_{fm,p,0}$ is the magnetic susceptibility of the ferromagnetic material in the MDCPs at a zero magnetic field. When the external magnetic field is high enough the ferromagnetic material in the MDCPs becomes magnetically saturated with $\alpha_{fm,p} = M_{fm,p,s}/3H$, where $M_{fm,p,s}$ represents the saturation magnetization of the ferromagnetic material of the spherical MDCPs. In this case, $\boldsymbol{M}_{fm,p} = M_{fm,p,s}\hat{\boldsymbol{H}}$, where the magnitude of $\boldsymbol{M}_{fm,p}$ is constant.

The local magnetic field strength at any position around the target is obtained from the familiar 2-D result with azimuthal symmetry [49] using the coordinate transformation [51] shown in Eq. (3.9);

$$H = H_0\left[1+\left(\frac{K_s^2}{r_a^6}-\frac{2K_s}{r_a^3}\right)+\left(\frac{K_s^2}{r_a^6}+\frac{2K_s}{r_a^3}\right)\left(3\sin^2\theta\cos^2\varphi\right)\right]^{\frac{1}{2}}, \tag{3.11}$$

where $K_s = \chi_{s,0}/\left(3+\chi_{s,0}\right)$ when the ferromagnetic material contained in the target is not magnetically saturated, and where $K_s = M_{s,s}/3H_0$ when it becomes saturated. Note that $\chi_{s,0}$ and $M_{s,s}$ represent the magnetic susceptibility of the ferromagnetic material in the target at a zero magnetic field and the saturation magnetization of the ferromagnetic material in the target, respectively.

The equations of motion of the MDCPs are obtained by substituting Eqs. (3.9) and (3.11) into Eq. (3.10), as shown in Eqs. (3.12) - (3.14):

$$\frac{dr_a}{dt} = \frac{v_{b,r}}{a} - \frac{\alpha_{fm,p} V_{ma}}{r_a^4}\left[3\left(\frac{K_s}{r_a^3}+1\right)\sin^2\theta\cos^2\varphi + \left(\frac{K_s}{r_a^3}-1\right)\right], \tag{3.12}$$

$$\frac{d\theta}{dt} = \frac{v_{b,\theta}}{ar_a} + \frac{\alpha_{fm,p} V_{ma}}{r_a^5}\left(1+\frac{K_s}{2r_a^3}\right)\sin 2\theta\cos^2\varphi, \tag{3.13}$$

$$\frac{d\varphi}{dt} = -\frac{\alpha_{fm,p} V_{ma}}{r_a^5}\left(1+\frac{K_s}{2r_a^3}\right)\sin 2\varphi, \tag{3.14}$$

where $V_{ma} = \dfrac{2R_p^2\omega_{fm,p}K_s\mu_0 H_0^2}{3\eta_b a^2}$ is defined as the magnetic velocity.

The $v_{b,r}$ and $v_{b,\theta}$ are the blood flow velocity components in spherical coordinates at the particle position at any time, and were determined by applying bilinear interpolation [33] to the blood velocity data found from the CFD software, as described in the Appendix D [54]. The blood velocity around the target inside the blood vessel is independent of φ due to its symmetry with respect to the direction of the inlet flow velocity in the $-\hat{\boldsymbol{z}}$ direction, as shown in Fig. 3.1, while $v_{b,\varphi}$ is not shown in Eq. (3.14) since it vanishes.

In order to obtain the trajectories of the MDCPs, Eqs. (3.12) - (3.14) are integrated numerically using the fourth-order Runge-Kutta method. The results are then analyzed to provide the capture distances, from which the capture area is evaluated by numerical integration.

The flow chart for finding the capture area for the IA-MDT using a spherical target under the influence of potential flow are shown in the Appendix C [9], in which the blood velocity with no wall effect results in a much less complicated problem compared to that of the work in this chapter. Nevertheless, the previously presented flow chart [9] is applicable to this work after including the part that is used to determine the blood velocity at any particle position, as shown in the Appendix D [54].

3.3 Results and Discussions

3.3.1 The 3-D Trajectories of MDCPs

The MDCPs carried by the inlet blood flow enter the considered part of the blood vessel and move towards the spherical target under the dominant influences of the magnetic and hydrodynamic forces. The trajectories of the entering MDCPs in the planes with angles φ (as defined in Fig. 3.1) equal to 0°, 45° and 90° are shown in Fig. 3.2. The inspection of particle trajectories by varying the initial position on the plane perpendicular to the inlet blood flow direction yields the capture distance, as indicated by the arrows. The capture distances for the entering MDCPs in the φ planes of 0° and 45° are 4.4 and 3.6, respectively, which are used to report the capture area in Fig. 3.3(c). Since no particles are captured for the entering MDCPs in the φ plane of 90°, then no capture distance is shown on this plane.

The magnitude of the magnetic velocity in the $\hat{\varphi}$ direction, as seen in Eq. (3.14), which is proportional to $\sin 2\varphi$, and is zero, maximum and zero for $\varphi = 0^\circ$, 45° and 90°, respectively. Therefore the particle trajectories remain on the entering planes $\varphi = 0^\circ$ and 90°, while the trajectories of MDCPs entering in the φ plane of 45° shift from the original plane as the particles move towards the target.

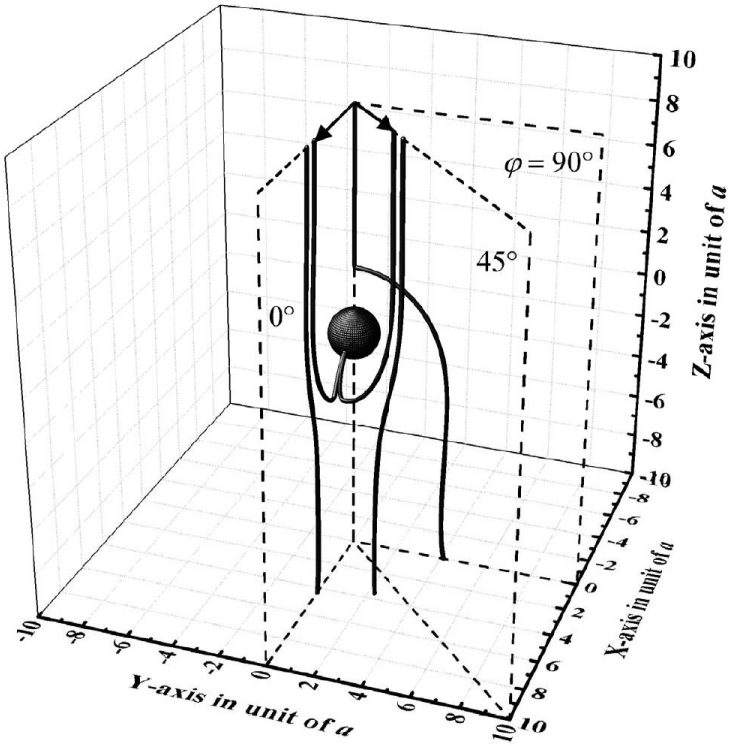

Figure 3.2 The 3-D trajectories of MDCPs with an average radius of 500 nm and 80% weight fraction are shown. A spherical target with a radius of 3 $\mu\mathrm{m}$ is implanted within the blood vessel with an average blood flow rate (v_{avg}) of 0.03 $\mathrm{m\,s^{-1}}$. The target is magnetized by an externally applied uniform magnetic field strength $(\mu_0 H_0)$ of 1.0 T, with all the other parameters as given in Table 3.1.

3.3.2 The Capture Areas of the MDCPs

Figure 3.3 depicts the capture areas of the MDCPs that are plotted on the plane perpendicular to the inlet blood flow for the three types of different ferromagnetic materials in the target and MDCPs. The capture area is obtained from the capture distances for varying φ planes of entering MDCPs. The capture distance is maximal for those MDCPs entering in the main symmetric plane ($\varphi = 0^\circ$) and decreased with increasing φ until no particles are captured for the φ plane of 90°. This is due to the effect of the 3-D local magnetic field around the spherical target, as shown in Eq. (3.11), which does not have azimuthal symmetry. The kidney-shaped capture areas in

Fig. 3.3 are similar to those demonstrated by Friedlaender et al. [49] for the capture of paramagnetic particles by a ferromagnetic sphere under the influence of laminar flow with no wall effect in a transverse configuration. The size of the capture area in case (a) is the largest followed by those in cases (b) and (c), respectively, as expected, which is due to the effects of the saturation magnetization of the ferromagnetic materials contained in the target and MDCPs. Further discussion on this is given in explanation of Fig. 3.4 next.

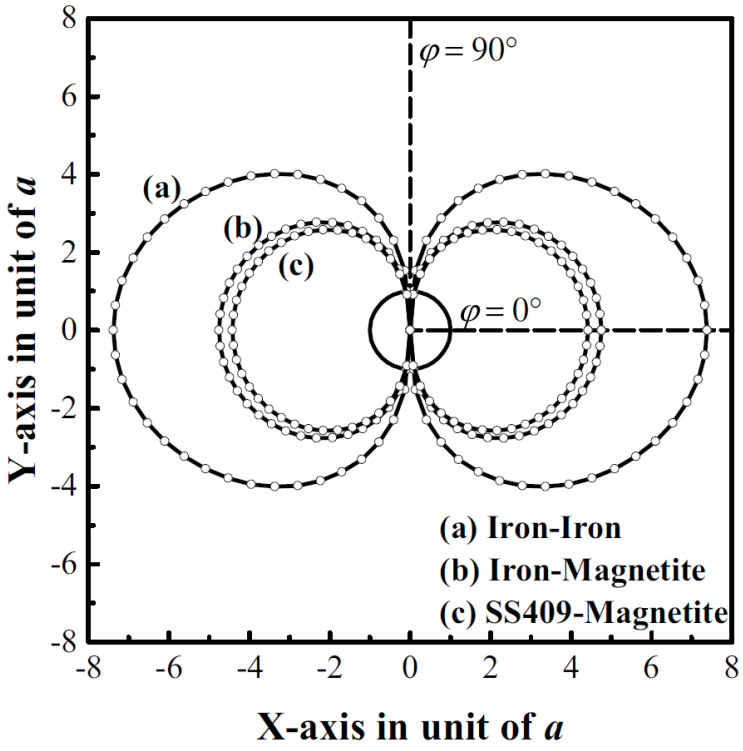

Figure 3.3 The capture areas of MDCPs with an average radius of 500 nm and 80% weight fraction are plotted for three types of target-MDCP materials, (a) iron-iron, (b) iron-magnetite and (c) SS409-magnetite. Data are shown for a spherical target with a radius of 3 $\mu\mathrm{m}$, magnetized by an externally applied uniform magnetic field strength $\left(\mu_0 H_0\right)$ of 1.0 T, and an average blood flow rate (v_{avg}) of 0.03 $\mathrm{m\,s^{-1}}$ is shown, with all the other parameters as given in Table 3.1.

3.3.3 The Effect of Uniform Externally Applied Magnetic Field Strength on the Capture Areas

The effect of the external magnetic field strength ($\mu_0 H_0$) on the dimensionless capture area (A_s), defined as the capture area divided by the target cross-section area, for the three different types of ferromagnetic materials in the targets and MDCPs is shown in Fig. 3.4. The A_s increase with increasing $\mu_0 H_0$ until the ferromagnetic materials in both the target and MDCPs become magnetically saturated at a $\mu_0 H_0$ of about 0.75 T for cases (a) and (b) and at about 0.6 T for case (c), whereupon A_s ceased to increase.

For cases (a), (b) and (c), A_s increase monotonically until the ferromagnetic materials in the MDCPs are magnetically saturated, with a required magnetic field strength ($\mu_0 H_s$) for the spherical MDCPs made of iron and magnetite of 0.73 and 0.19 T, respectively. For cases (b) and (c), after the saturation magnetization of the magnetite MDCPs occurs at a $\mu_0 H_0$ of about 0.2 T, A_s continues to increase but with a less steep slope, and reaches a maximum when the ferromagnetic materials in the targets are magnetically saturated, at a $\mu_0 H_0$ of about 0.75 T for cases (a) and (b) and 0.6 T for case (c). These $\mu_0 H_0$ values are close to the $\mu_0 H_s$ for the spherical targets made of iron and SS409 (0.73 and 0.59 T, respectively).

The variations in the slope of A_s, due to the saturation magnetizations of the ferromagnetic materials in the MDCPs and target, can be explained by analyzing the magnetic term in Eq. (3.12) based on the K_s and $\alpha_{fm,p}$. Before the ferromagnetic materials in both the target and MDCPs become magnetically saturated, the magnetic term in Eq. (3.12) is proportional to H_0^2 because both K_s and $\alpha_{fm,p}$ are constant, resulting in a pronounced increase in A_s with increasing $\mu_0 H_0$. When only the ferromagnetic material in the MDCPs become magnetically saturated, the magnetic term in Eq. (3.12) is proportional to H_0^2 / H, because $\alpha_{fm,p}$ is proportional to H^{-1}, resulting in a lower increase in A_s. After the ferromagnetic materials in both the target and MDCPs become magnetically saturated, the magnetic term in Eq. (3.12) is

proportional to H^{-1} because K_s and $\alpha_{fm,p}$ are proportional to H_0^{-1} and H^{-1}, respectively, resulting in the slight decrease in A_s.

In addition, the A_s of cases (b) and (c) for $\mu_0 H_0 \leq$ 0.6 T are equal because the same type of ferromagnetic materials are contained in the MDCPs. For a $\mu_0 H_0$ larger than 0.6 T, the A_s of case (c) does not increase due to the saturation magnetization of the SS409 target while the A_s of case (b) continues to increase until the iron target was magnetically saturated at a $\mu_0 H_0$ of about 0.75 T. Moreover, the A_s of cases (b) and (c) are larger than that of case (a) at a low magnetic field strength ($\mu_0 H_0$ < 0.25 T) because the density of magnetite is lower than that of iron resulting in the larger $\omega_{fm,p}$, according to Eq. (3.4), and as previously explained [14].

The effect of an externally uniform applied magnetic field strength ($\mu_0 H_0$) on the dimensionless capture area (A_s) with varying MDCP radii and a v_{avg} of 0.03 and 0.05 $\mathrm{m\,s^{-1}}$ is shown in Figs. 3.5(a) and (b), respectively. The general behavior of A_s in Fig. 3.5(a) and (b) was similar to that in Fig. 3.4 case (c) because the target and MDCP materials were the same. The A_s increased as the MDCP radius (R_p) increased. Since, the magnetic force is proportional to R_p^3, then the increments of increasing A_s were increased at larger values of R_p. In addition, an externally applied uniform magnetic field strength of larger than 0.6 T did not increase A_s, because the ferromagnetic materials in both target and MDCPs (SS409 and magnetite, respectively), had already become magnetically saturated.

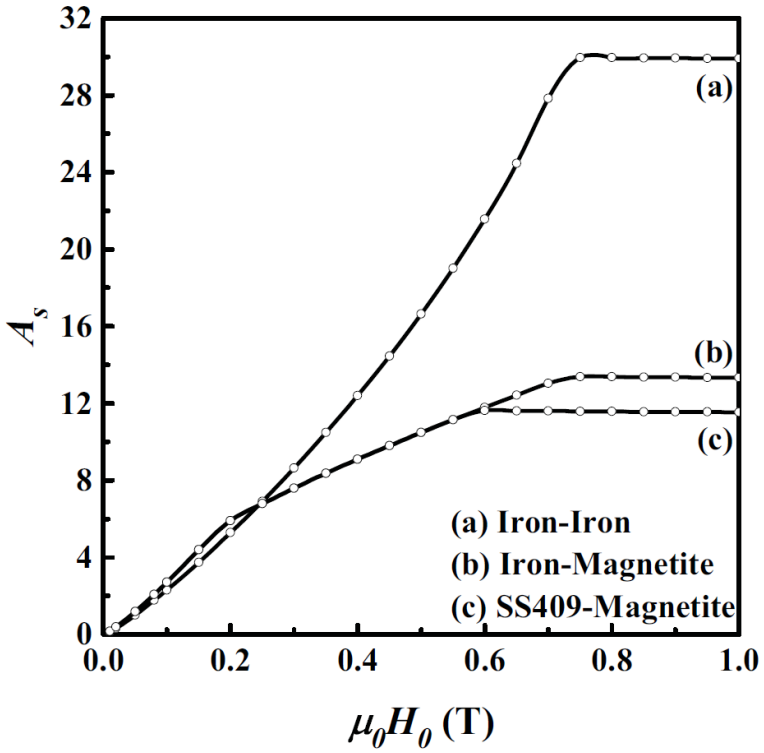

Figure 3.4 Effect of an externally applied magnetic field strength ($\mu_0 H_0$) on the dimensionless capture area (A_s) of MDCPs with a radius of 500 nm and 80% weight fraction for three types of target-MDCP materials: (a) iron-iron, (b) iron-magnetite and (c) SS409-magnetite. Data are shown for a spherical target with a radius of 3 μm and an average blood flow rate (v_{avg}) of 0.03 $\mathrm{m\,s^{-1}}$ is shown, with all the other parameters as given in Table 3.1.

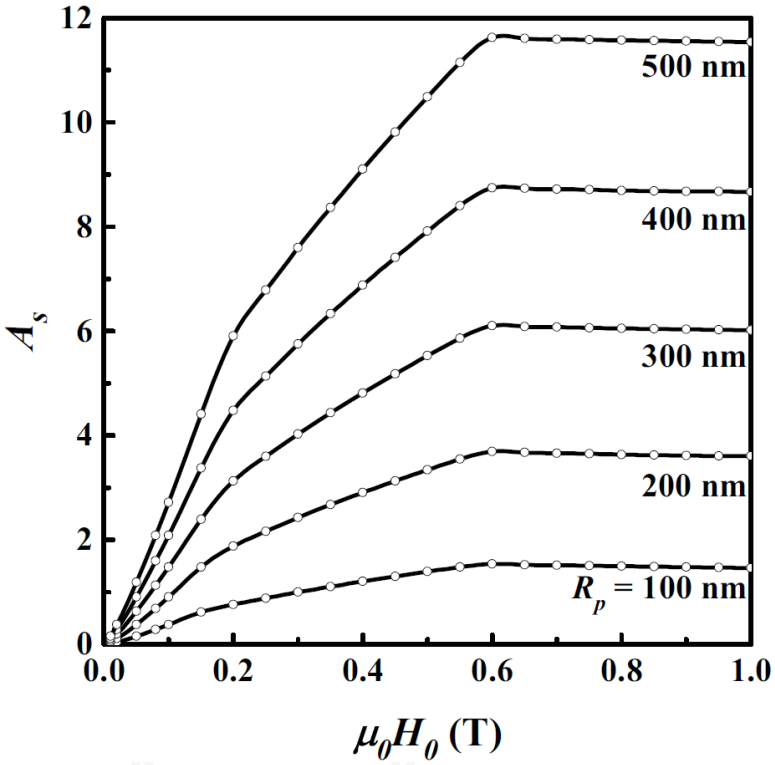

Figure 3.5(a) Effect of an externally applied magnetic field strength ($\mu_0 H_0$) on the dimensionless capture area (A_s) of MDCPs for average blood flow rates (v_{avg}) of 0.03 $\mathrm{m\,s^{-1}}$ for MDCP of different radii (R_p). Data are shown for a spherical target with radius of 3 $\mu\mathrm{m}$ and the MDCPs made of magnetite with 80% weight fraction, with all the other parameters as given in Table 3.1.

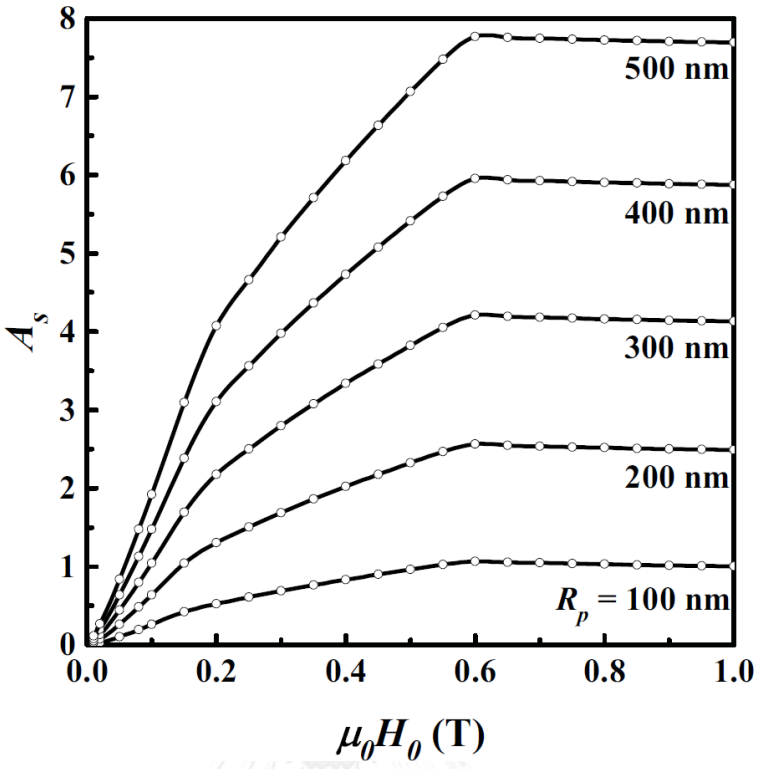

Figure 3.5(b) Effect of an externally applied magnetic field strength ($\mu_0 H_0$) on the dimensionless capture area (A_s) of MDCPs for average blood flow rates (v_{avg}) of 0.05 ms^{-1} for MDCP of different radii (R_p). Data are shown for a spherical target with radius of 3 $\mu\mathrm{m}$ and the MDCPs made of magnetite with 80% weight fraction, with all the other parameters as given in Table 3.1.

3.3.4 The Effect of MDCP size on the Maximum Capture Areas

The effect of the MDCP size on the maximum dimensionless capture area ($A_{s,\max}$) for four types of ferromagnetic materials in the targets and MDCPs with v_{avg} of 0.01 $\mathrm{m\,s}^{-1}$ is shown in Fig. 3.6, where $A_{s,\max}$ represents the maximum value of the dimensionless capture area (A_s), determined by varying the external magnetic field strength ($\mu_0 H_0$), as shown in Fig. 3.5(a) and (b). With these results, the prediction of the appropriate MDCP sizes for the required capture areas or capture efficiencies, as defined by the percentage of MDCPs entering the blood vessel that are captured by

the target, can be obtained. For example, if the required effectiveness of IA-MDT is equivalent to a capture efficiency of 50% ($A_{s,max}$ of 6.6) then MDCPs with an average radii of about 140, 180, 220 and 240 nm are suggested for the targets and MDCPs types of (a), (b), (c) and (d), respectively. It should be noted that the maximum reported capture areas in this work were less than the dimensionless blood vessel cross-section area, which was 13.2 for a v_{avg} of 0.01 $\mathbf{m\,s^{-1}}$ [52]. Therefore, MDCPs with average radii of 300, 350, 400 and 450 nm, which corresponded to a capture efficiency of about 94%, are suggested as the optimum MDCPs sizes for the targets and MDCPs types of (a), (b), (c) and (d), respectively.

The effect of the MDCP size on $A_{s,max}$ with inlet average blood flow rates (v_{avg}) of 0.01, 0.03 and 0.05 $\mathbf{m\,s^{-1}}$ is shown in Fig. 3.7. For a v_{avg} of 0.01 $\mathbf{m\,s^{-1}}$, if the required effectiveness of IA-MDT is equivalent to a capture efficiency of 50% ($A_{s,max}$ of 6.6) then a R_p of about 140 nm is suggested. In addition, MDCPs with an average radius of 250 nm, corresponding to a capture efficiency of about 94%, is suggested as the optimum R_p. For a v_{avg} of 0.03 and 0.05 $\mathbf{m\,s^{-1}}$, an $A_{s,max}$ of about 11.6 and 7.8, respectively, corresponded to capture efficiencies of about 18.2% and 5.1%, respectively, is obtained when R_p is 500 nm. Those $A_{s,max}$ values are much lower than the dimensionless vessel cross-sections, which are 64 and 154 for a v_{avg} of 0.03 $\mathbf{m\,s^{-1}}$ and 0.05 $\mathbf{m\,s^{-1}}$ [52], respectively, resulting in small capture efficiencies. Two more case studies, those for blood flow rates of 0.03 and 0.05 $\mathbf{m\,s^{-1}}$ with MDCP radii of $\mathbf{9.7\times10^{2}}$ and $\mathbf{1.8\times10^{3}}$ nm, respectively, reveals that the corresponding $A_{s,max}$ are 32 and 77, where the capture efficiency in both cases is 50%.

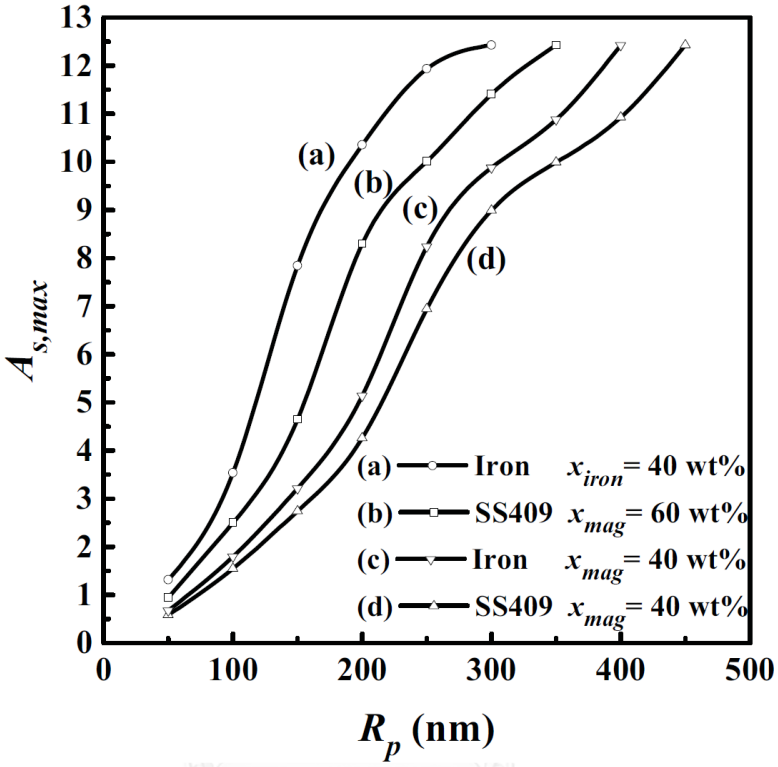

Figure 3.6 Effect of the MDCP radius (R_p) on the maximum dimensionless capture area ($A_{s,max}$) for four types of target and MDCPs: (a) iron target and iron MDCPs with 40% weight fraction, (b) SS409 target and magnetite MDCPs with 60% weight fraction, (c) iron target and magnetite MDCPs with 40% weight fraction and (d) SS409 target and magnetite MDCPs with 40% weight fraction. Data are shown for an implanted spherical target with a radius of 3 μm in the vessel with an average blood flow rate (v_{avg}) of 0.01 $\mathrm{m\,s^{-1}}$, with all the other parameters as given in Table 3.1.

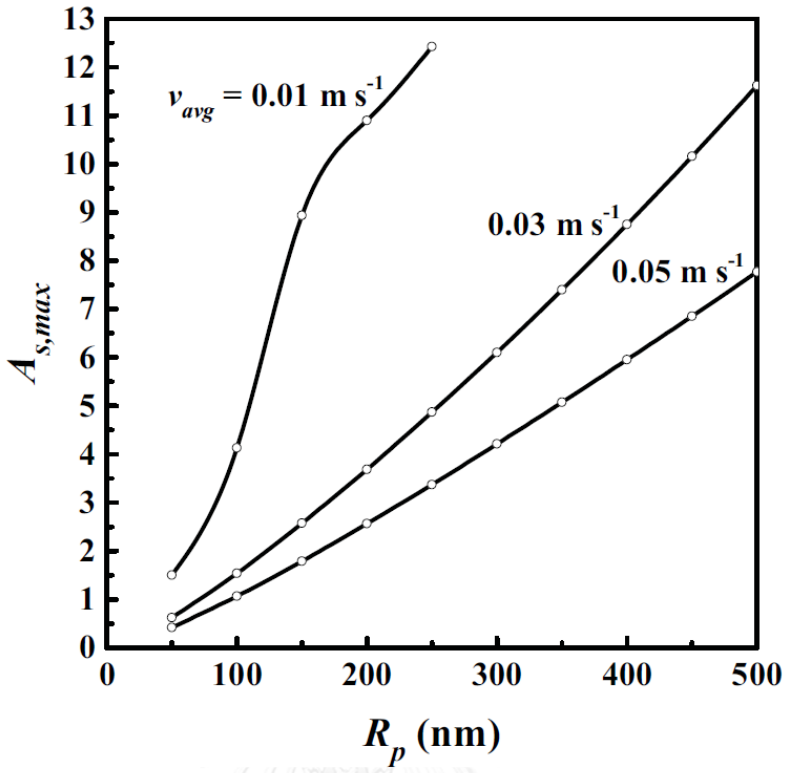

Figure 3.7 Effect of the MDCP radius (R_p) on the maximum dimensionless capture area ($A_{s,max}$) of MDCPs consisting of magnetite with 80% weight fraction that are captured by a spherical target made of SS409 with radius of 3 μm for average blood flow rates (v_{avg}) of 0.01, 0.03 and 0.05 m s^{-1}, with all the other parameters as given in Table 3.1.

3.4 Conclusions

The 3-D IA-MDT using ferromagnetic spherical targets implanted within blood vessels including the vessel wall effect was investigated. The chapter focused on the use of IA-MDT to improve the effectiveness of the MDCP capture in arterioles. The equations of motion of MDCPs, carried by the bloodstream towards a target magnetized by a uniform externally applied magnetic field, were derived based on the magnetic and hydrodynamic drag forces acting on the MDCPs. The blood flow was categorized as a laminar flow, and the blood velocity at any particle position around the target was obtained by applying bilinear interpolation [33] to the numerical blood

velocity data. The trajectories of the MDCPs were simulated from the equations of motion to obtain the capture distances and then the capture area was obtained by numerical integration. The effects of various parameters on the capture areas were determined and reported.

The 3-D particle trajectories and the capture areas (Figs. 3.2 and 3.3, respectively) revealed a kidney-shaped capture area, similar to that previously reported for paramagnetic particle capture by a ferromagnetic sphere under a laminar flow with no wall effect in a transverse configuration [49]. The physical effects of saturation magnetization of the ferromagnetic materials in the target and MDCPs on the dimensionless capture areas (A_s) were determined by varying the externally applied magnetic field strength $(\mu_0 H_0)$. The saturation magnetizations of the iron and SS409 targets occurred at a $\mu_0 H_0$ of 0.75 T and 0.6 T (Fig. 3.4), respectively, and subsequently A_s did not increase with increasing $\mu_0 H_0$ above those reported $\mu_0 H_0$ values. Overall, A_s was substantially reduced when the iron in the MDCPs was replaced by magnetite, while it was only slightly reduced when the target material was changed from iron to SS409. The use of magnetite MDCPs is a good choice because it is biocompatible and inexpensive. In addition, SS409 is more suitable to use than iron as a ferromagnetic material in the targets for implanting in blood vessels because of its higher corrosion resistance. The A_s of the SS409 target and magnetite MDCPs with an average radius of 500 nm were maximal at about 11.6 and 7.8 for an v_{avg} of 0.03 and 0.05 $\mathrm{m\,s^{-1}}$, respectively, as shown in Fig. 3.5(a) and (b). For the SS409 target and magnetite MDCPs, the dimensionless capture areas ranged from 1.5-12.4, 0.6-11.6 and 0.4-7.8, corresponding to a R_p range from 50-500 nm, for average blood flow rates of 0.01, 0.03 and 0.05 $\mathrm{m\,s^{-1}}$, respectively, with a weight fraction of 80% and $\mu_0 H_0$ of 0.6 T (Fig. 3.7). For blood flow rates of 0.03 and 0.05 $\mathrm{m\,s^{-1}}$, an increase in R_p above 500 nm provided a larger A_s and resulted in a more effective IA-MDT system. However, the use of large MDCP sizes could irritate the surrounding tissues, cause thrombosis or embolism in blood vessels and decrease the diffusion ability, all of which can affect the distribution of the drug concentration.

The more general 3-D modelling of IA-MDT using spherical implanted targets in this work is not limited to arterioles, but it is applicable to blood vessels of various sizes for both laminar and potential blood flows. Furthermore, the previously reported IA-MDT using spherical targets and 2-D approaches can be developed into 3-D, using our presented method, in order to yield the capture areas, which could then be used to provide more accurate predictions of the effectiveness of the respective IA-MDT systems.

CHAPTER IV
SIMULATION OF DYNAMIC MAGNETIC DRUG CARRIER PARTICLE CAPTURE AND ACCUMULATION AROUND A FERROMAGNETIC CYLINDRICAL TARGET

In this research, the 2-D dynamic capture and accumulation of MDCPs on a single ferromagnetic cylindrical target is investigated. This dynamic model includes the effect of the accumulation of MDCPs on both the fluid flow and local magnetic field around the target manifested by the volume concentration of MDCPs around the cylindrical target and the magnetization of MDCPs. The effect of the accumulation of MDCPs on the fluid flow is considered by creating the fluid viscosity as a function of the volume concentration of MDCPs, with imposed maximum particle concentration and maximum fluid viscosity limits. The effect of the accumulation of MDCPs on the local magnetic field around the target is considered by including the magnetization of MDCPs. The ferromagnetic cylindrical target is located at the center of the 2-D rectangular control area. The fluid flow within control area is assumed to be laminar flow. The external magnetic field is applied across the control area, perpendicular to the direction of the average inlet fluid velocity, to magnetize the target in order to create the high gradient magnetic field. Only the magnetic, hydrodynamic and diffusion forces are considered in this model. The unsteady-state Navier-Stokes equations for compressible fluid flow, the unsteady-state continuity equations and the Laplace equations of the magnetic potential are solved simultaneously to obtain the velocities and volume concentrations of the fluid. The simulation results reveals the realistic dynamic capture and accumulation of MDCPs around a magnetized ferromagnetic cylindrical target, the mass of MDCPs collected, the breakthrough curves of normalized output solid mass flow rates and the percentage capture efficiency. In this dynamic model, we also investigates the effects of including and excluding the magnetization of MDCPs on the mass of MDCPs collected, the breakthrough curves and the percentage capture efficiency.

4.1 Problem Definition

The configuration of the 2-D rectangular control area defined for the dynamic capture and accumulation of MDCPs by a ferromagnetic cylindrical target is shown in Fig. 4.1. It consists of three main components: a ferromagnetic cylindrical target of radius R_w located at the center of the control area, the fluid flow across the control area with a dynamic viscosity as a function of particle concentration, and a uniform externally applied magnetic field $(\boldsymbol{H}_0)$ which is perpendicular to the direction of the average inlet fluid velocity $(\boldsymbol{u}_0)$. The directions of both $\boldsymbol{u}_0$ and $\boldsymbol{H}_0$ are denoted in the Fig. 4.1. This rectangular control area is created in COMSOL Multiphysics version 5.2, where all the model equations are set up and solved.

The fluid flowing across the channel is composed of the MDCPs and water. The MDCPs are assumed to be spherical particles of radii R_p and comprised of certain volume fractions of ferromagnetic and polymeric drug carrier materials. The properties of these MDCPs are shown in Table 4.1.

Only the magnetic, hydrodynamic and diffusion forces are considered in this model. The gravitational force is negligibly small compared to the magnetic and hydrodynamic drag forces. Particle to particle interactions, such as electrostatic, van der Waals and magnetic dipole-dipole are also neglected because of their inherent complexity. The MDCPs in the fluid experience all these three forces, but the liquid experiences only the hydrodynamic drag force. The unsteady-state Navier-Stokes equations for compressible fluid flow and the unsteady-state continuity equations are used to describe the velocities and volume concentrations of both the MDCPs and water in fluid.

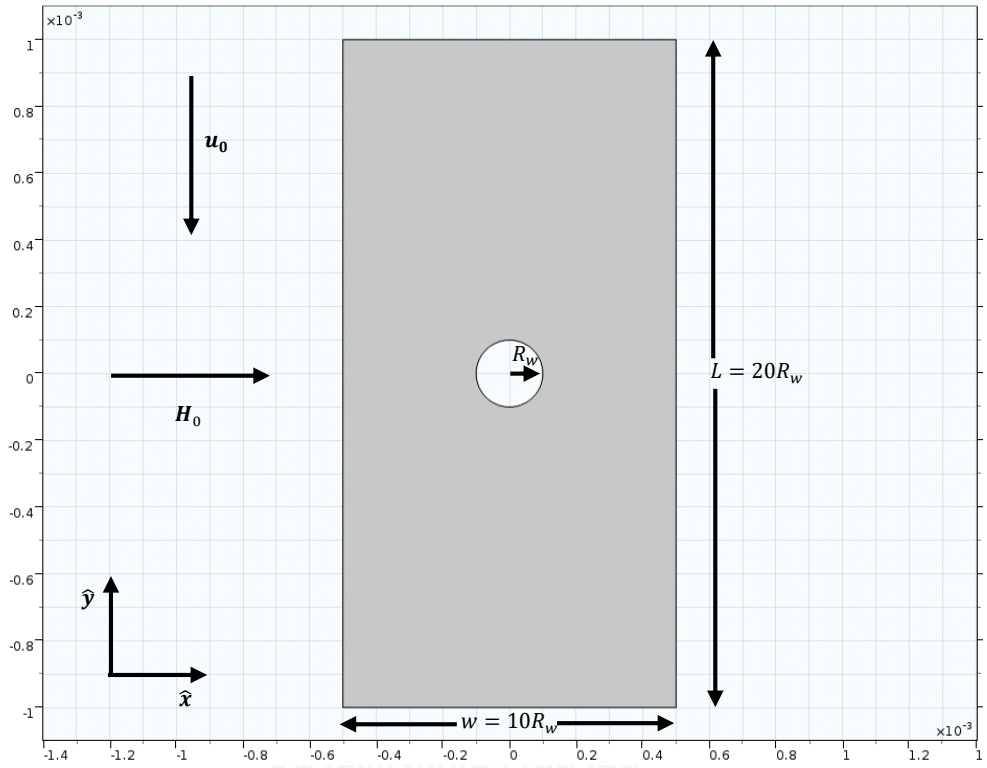

Figure 4.1 Schematic of the 2-D rectangular control area used in the dynamic and trajectory models, where the MDCPs are captured by a ferromagnetic cylindrical target of radius R_w placed at the center of the control area with length $L = 20R_w$ and width $W = 10R_w$. The uniform external magnetic field $(\boldsymbol{H}_0)$ is applied in the direction perpendicular to the average inlet flow velocity $(\boldsymbol{u}_0)$. The parameter values and other model parameters are given in Table 4.1.

Table 4.1 Conditions and parameters used in the dynamic model

Properties	Units	Values
Density of water (ρ_w)	kg m^{-3}	997.1
Viscosity of water (μ_w)	kg $m^{-1}s^{-1}$	8.9×10^{-4}
Average fluid velocity at the inlet (u_0)	m s^{-1}	0.02
Temperature (T)	K	298.15
Initial volume fraction of MDCPs (ϕ_0)	-	0.001
MDCP radius (R_p)	μm	2
Maximum fluid (slurry) viscosity $(\mu_{\max})$	kg $m^{-1}s^{-1}$	$10^8\,\mu_w$
Weight fraction of magnetite in the MDCPs $(x_{fm,p})$	-	0.20
Density of polymer in the MDCPs $(\rho_{p,pol})$	kg m^{-3}	950
Density of magnetite in the MDCPs $(\rho_{fm,p})$	kg m^{-3}	5050
Radius of the iron cylindrical target (R_w)	μm	100
Density of the iron cylindrical target $(\rho_{fm,w})$	kg m^{-3}	7850
Channel width (w)	μm	$10\,R_w$
Channel length (L)	μm	$20\,R_w$
Applied external magnetic field $(\mu_0 H_0)$	μm	0.02, 0.05, 0.1, 0.15
Magnetic susceptibility of magnetite in the MDCPs at $\mu_0 H_0 = 0$ $(\chi_{fm,p,0})$	-	1000
Magnetic susceptibility of the iron cylindrical target at $\mu_0 H_0 = 0$ $(\chi_{w,0})$	-	1000
Saturation magnetization of magnetite in the MDCPs $(M_{fm,p,s})$	A m^{-1}	455×10^3
Saturation magnetization of the iron cylindrical target $(M_{w,s})$	A m^{-1}	1735×10^3

4.2 Theory

4.2.1 Bulk Density of the MDCPs and the Liquid Phase

Let's consider a unit control volume V consisted of both MDCPs and liquid phase. Then, the volume fraction of MDCPs (ϕ) is written as

$$\phi = \frac{V_s}{V}, \tag{4.1}$$

and

$$V = V_s + V_l, \tag{4.2}$$

where V_s and V_l are the volume occupied by solid (MDCPs) and liquid phases, respectively.

Hence, the bulk density of MDCPs (ρ_s) is defined as

$$\rho_s = \phi\rho_p, \tag{4.3}$$

and the bulk density of liquid phase (ρ_l) is defined as

$$\rho_l = (1-\phi)\rho_w, \tag{4.4}$$

where ρ_p and ρ_w are the density of a single MDCP and the density of water, respectively.

4.2.2 Momentum Balance Equations for MDCPs and Liquid Phases

The 2-D unsteady-state Navier-Stokes equations for compressible fluid flow are written as

$$\rho_p\left(\frac{\partial}{\partial t}+(\boldsymbol{v}_s\cdot\nabla)\right)\boldsymbol{v}_s = \nabla\cdot\begin{pmatrix} -\left(p+\frac{2}{3}\mu(\phi)\nabla\cdot\boldsymbol{v}_s\right)+2\mu(\phi)\frac{\partial v_{s,x}}{\partial x} & \mu(\phi)\left(\frac{\partial v_{s,y}}{\partial x}+\frac{\partial v_{s,x}}{\partial y}\right) \\ \mu(\phi)\left(\frac{\partial v_{s,y}}{\partial x}+\frac{\partial v_{s,x}}{\partial y}\right) & -\left(p+\frac{2}{3}\mu(\phi)\nabla\cdot\boldsymbol{v}_s\right)+2\mu(\phi)\frac{\partial v_{s,y}}{\partial y} \end{pmatrix} + \left(\frac{\boldsymbol{F}_m+\boldsymbol{F}_d+\boldsymbol{F}_b}{V_p}\right)\Phi(\phi), \tag{4.5}$$

and

$$\rho_w\left(\frac{\partial}{\partial t}+(\boldsymbol{v}_l\cdot\nabla)\right)\boldsymbol{v}_l = \nabla\cdot\begin{pmatrix} -\left(p+\frac{2}{3}\mu(\phi)\nabla\cdot\boldsymbol{v}_l\right)+2\mu(\phi)\frac{\partial v_{l,x}}{\partial x} & \mu(\phi)\left(\frac{\partial v_{l,y}}{\partial x}+\frac{\partial v_{l,x}}{\partial y}\right) \\ \mu(\phi)\left(\frac{\partial v_{l,y}}{\partial x}+\frac{\partial v_{l,x}}{\partial y}\right) & -\left(p+\frac{2}{3}\mu(\phi)\nabla\cdot\boldsymbol{v}_l\right)+2\mu(\phi)\frac{\partial v_{l,y}}{\partial y} \end{pmatrix} - \frac{\phi\boldsymbol{F}_d}{(1-\phi)V_p}, \tag{4.6}$$

for solid (MDCPs) phase with velocity of $\boldsymbol{v}_s$ and liquid (water) phase with velocity of $\boldsymbol{v}_l$, respectively. $\mu(\phi)$ is a dynamic fluid viscosity which is a function of ϕ and p is the pressure of the fluid. $\boldsymbol{F}_m$, $\boldsymbol{F}_d$ and $\boldsymbol{F}_b$ are the magnetic, hydrodynamic drag and diffusion forces acting on MDCPs, respectively, which are described later. $\Phi(\phi)$ is a constraint function that approaches to zero when ϕ approaches to its maximum allowed value of $\phi_{\max}$.

The MDCP capture and accumulation around the ferromagnetic cylindrical target affects the fluid flow through the dynamic fluid viscosity $\left(\mu\left(\phi\right)\right)$ which depends on the volume fraction of MDCPs. The conditions of $\mu\left(\phi\right)$ are $\mu\left(\phi=0\right)=\mu_w$ and $\mu\left(\phi=\phi_{\max}\right)=\mu_{\max}$, where μ_w and $\mu_{\max}$ are the viscosity of water and the maximum allowed viscosity.

The dynamic fluid viscosity is written as

$$\mu\left(\phi\right)=\frac{\mu_{\max}+\mu_w}{1+e^{\ln\left(\frac{\mu_{\max}}{\mu_w}\right)\left(1-\frac{2\phi}{\phi_{\max}}\right)}}, \tag{4.7}$$

where the maximum MDCP volume fraction $\left(\phi_{\max}\right)$ and the maximum viscosity $\left(\mu_{\max}\right)$ are assumed to be $10^8\mu_w$ and 0.64 [55], respectively. The behavior of dynamic fluid viscosity function, according to Eq. (4.28), is shown in Fig. 4.2.

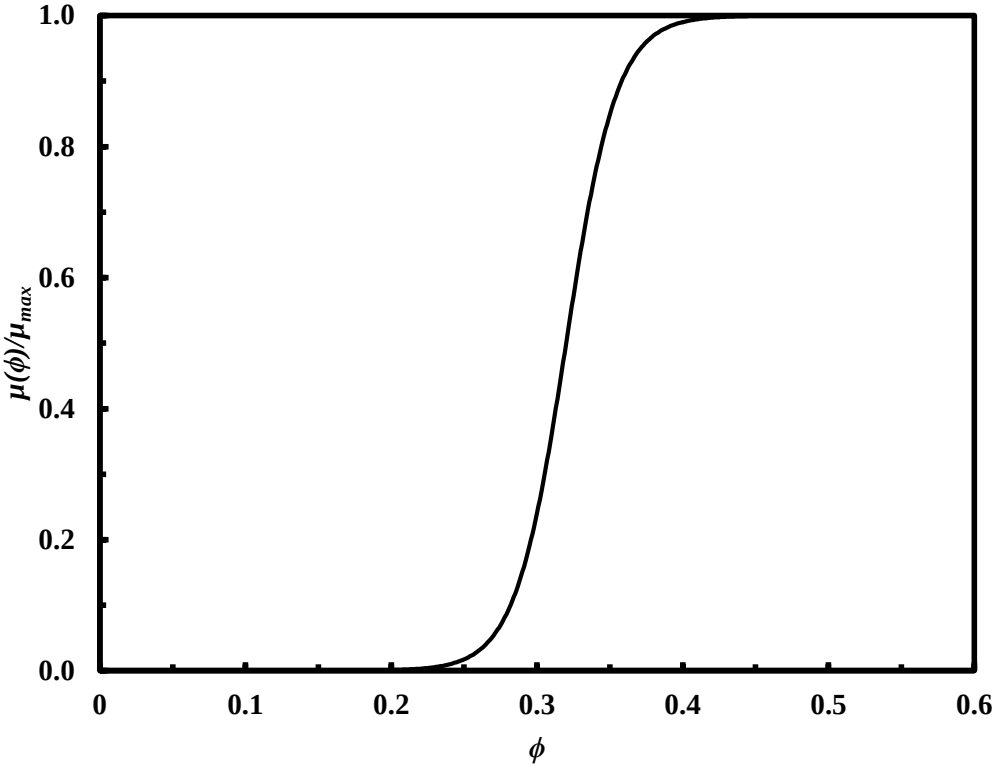

Figure 4.2 Ratio of the dynamic fluid viscosity $\mu\left(\phi\right)$ to the maximum viscosity $\left(\mu_{\max}\right)$ as a function of the magnetic particle volume fraction ϕ according to Eq. (4.28) with imposed $\mu_{\max}$ = $10^8\mu_w$ and $\phi_{\max}$ = 0.64.

In addition, the external force term for solid phase in Eq. (4.5) becomes zero when volume fraction of MDCPs approaches to $\phi_{\max}$ in order to prevent exceeding the maximum concentration of MDCPs. This is achieved by using the constraint function $\Phi(\phi)$, which is assumed to be

$$\Phi(\phi) = \frac{1}{1+e^{2000(\phi-0.62)}}. \tag{4.8}$$

In addition, Eq. (4.5) can be written for $\hat{\boldsymbol{x}}$ direction as

$$\begin{aligned}\rho_p\left(\frac{\partial v_{s,x}}{\partial t}+v_{s,x}\frac{\partial v_{s,x}}{\partial x}+v_{s,y}\frac{\partial v_{s,x}}{\partial y}\right) &= -\frac{\partial p}{\partial x}+\left[\frac{\partial}{\partial x}\left(\mu(\phi)\frac{\partial v_{s,x}}{\partial x}\right)+\frac{\partial}{\partial y}\left(\mu(\phi)\frac{\partial v_{s,x}}{\partial y}\right)\right] \\ &+\frac{1}{3}\left[\frac{\partial}{\partial x}\left(\mu(\phi)\frac{\partial v_{s,x}}{\partial x}\right)+3\frac{\partial}{\partial y}\left(\mu(\phi)\frac{\partial v_{s,y}}{\partial x}\right)-2\frac{\partial}{\partial x}\left(\mu(\phi)\frac{\partial v_{s,y}}{\partial y}\right)\right] \\ &+\left(\frac{F_{m,x}+F_{d,x}+F_{b,x}}{V_p}\right)\Phi(\phi),\end{aligned} \tag{4.9}$$

and for $\hat{\boldsymbol{y}}$ direction as

$$\begin{aligned}\rho_p\left(\frac{\partial v_{s,y}}{\partial t}+v_{s,x}\frac{\partial v_{s,y}}{\partial x}+v_{s,y}\frac{\partial v_{s,y}}{\partial y}\right) &= -\frac{\partial p}{\partial y}+\left[\frac{\partial}{\partial x}\left(\mu(\phi)\frac{\partial v_{s,y}}{\partial x}\right)+\frac{\partial}{\partial y}\left(\mu(\phi)\frac{\partial v_{s,y}}{\partial y}\right)\right] \\ &+\frac{1}{3}\left[3\frac{\partial}{\partial x}\left(\mu(\phi)\frac{\partial v_{s,x}}{\partial y}\right)-2\frac{\partial}{\partial y}\left(\mu(\phi)\frac{\partial v_{s,x}}{\partial x}\right)+\frac{\partial}{\partial y}\left(\mu(\phi)\frac{\partial v_{s,y}}{\partial y}\right)\right] \\ &+\left(\frac{F_{m,y}+F_{d,y}+F_{b,y}}{V_p}\right)\Phi(\phi).\end{aligned} \tag{4.10}$$

As same as Eq. (4.5), Eq. (4.6) can be written for $\hat{\boldsymbol{x}}$ and $\hat{\boldsymbol{y}}$ directions as

$$\rho_w\left(\frac{\partial v_{l,x}}{\partial t}+v_{l,x}\frac{\partial v_{l,x}}{\partial x}+v_{l,y}\frac{\partial v_{l,x}}{\partial y}\right)=-\frac{\partial p}{\partial x}+\left[\frac{\partial}{\partial x}\left(\mu(\phi)\frac{\partial v_{l,x}}{\partial x}\right)+\frac{\partial}{\partial y}\left(\mu(\phi)\frac{\partial v_{l,x}}{\partial y}\right)\right]$$
$$+\frac{1}{3}\left[\frac{\partial}{\partial x}\left(\mu(\phi)\frac{\partial v_{l,x}}{\partial x}\right)+3\frac{\partial}{\partial y}\left(\mu(\phi)\frac{\partial v_{l,y}}{\partial x}\right)-2\frac{\partial}{\partial x}\left(\mu(\phi)\frac{\partial v_{l,y}}{\partial y}\right)\right] \quad (4.11)$$
$$-\left(\frac{\phi F_{d,x}}{(1-\phi)V_p}\right),$$

and

$$\rho_p\left(\frac{\partial v_{s,y}}{\partial t}+v_{s,x}\frac{\partial v_{s,y}}{\partial x}+v_{s,y}\frac{\partial v_{s,y}}{\partial y}\right)=-\frac{\partial p}{\partial y}+\left[\frac{\partial}{\partial x}\left(\mu(\phi)\frac{\partial v_{s,y}}{\partial x}\right)+\frac{\partial}{\partial y}\left(\mu(\phi)\frac{\partial v_{s,y}}{\partial y}\right)\right]$$
$$+\frac{1}{3}\left[3\frac{\partial}{\partial x}\left(\mu(\phi)\frac{\partial v_{s,x}}{\partial y}\right)-2\frac{\partial}{\partial y}\left(\mu(\phi)\frac{\partial v_{s,x}}{\partial x}\right)+\frac{\partial}{\partial y}\left(\mu(\phi)\frac{\partial v_{s,y}}{\partial y}\right)\right] \quad (4.12)$$
$$-\left(\frac{\phi F_{d,y}}{(1-\phi)V_p}\right),$$

respectively. When μ is not equal to function of ϕ, then Eqs. (4.7) - (4.10) can be reduced to the more familiar form of the Navier-Stokes equation.

4.2.3 Mass Balance Equations for Solid (MDCPs) and Liquid Phases

The 2-D unsteady-state continuity equations for the solid phase with bulk density ρ_s are written as

$$\frac{d\rho_s}{dt}+\nabla\cdot(\rho_s\mathbf{v}_s)=0, \quad (4.13)$$

and for the liquid phase with bulk density ρ_l are

$$\frac{d\rho_l}{dt}+\nabla\cdot(\rho_l\mathbf{v}_l)=0, \quad (4.14)$$

where ρ_s and ρ_l can be written in terms of ϕ, ρ_p and ρ_w as shown in Eqs. (4.3) and (4.4), respectively.

4.2.4 Inlet Fluid Velocity Profile

The fluid flow is categorized into a laminar flow regime. The no-slip boundary condition is used at the contact surfaces between the fluid and walls. The fluid velocity profile at the inlet of the control area $\left(\boldsymbol{v}_f\right)$ is assumed to be parabolic flow profile according to

$$\boldsymbol{v}_f = 1.5\boldsymbol{u}_0\left(1-4\left(\frac{x}{w}\right)^2\right) \tag{4.15}$$

where $\boldsymbol{u}_0$ and w are the average inlet fluid flow velocity in the $-\hat{\boldsymbol{y}}$ direction and width of the rectangular control area, respectively.

4.2.5 Forces on Fluid

The magnetic force $\left(\boldsymbol{F}_m\right)$ acting on a single spherical MDCP is given by [20, 23]:

$$\boldsymbol{F}_m = \frac{1}{2}V_p\mu_0\omega_{fm,p}\nabla\left(\boldsymbol{M}_{fm,p}\cdot\boldsymbol{H}\right), \tag{4.16}$$

where μ_0 is the magnetic permeability of free space, $\omega_{fm,p}$ is the volume fraction occupied by the ferromagnetic material inside the MDCP, $\boldsymbol{M}_{fm,p}$ is the induced magnetization of the MDCP, and $\boldsymbol{H}$ is the local magnetic field around the magnetized ferromagnetic target.

The volume fraction of the ferromagnetic material $\left(\omega_{fm,p}\right)$ inside the MDCPs is related to the weight fraction of ferromagnetic material $\left(x_{fm,p}\right)$ inside the MDCPs. It can be shown that

$$\omega_{fm,p} = \rho_p \frac{x_{fm,p}}{\rho_{fm,p}}, \tag{4.17}$$

and

$$\rho_p = \frac{1}{\frac{x_{fm,p}}{\rho_{fm,p}} + \frac{1-x_{fm,p}}{\rho_{pol,p}}}, \tag{4.18}$$

where ρ_p represents the average density of the MDCPs, $\rho_{fm,p}$ and $\rho_{pol,p}$ are the density of the ferromagnetic material inside the MDCP and the density of both the polymer and the drug inside the MDCP, respectively.

The Stokes drag force $\left(\boldsymbol{F}_d\right)$ acting on a single MDCP is defined by

$$\boldsymbol{F}_d = 6\pi\mu(\phi) R_p \left(\boldsymbol{v}_l - \boldsymbol{v}_s\right). \tag{4.19}$$

The diffusion force $\left(\boldsymbol{F}_b\right)$ acting on a single MDCP is given by

$$\boldsymbol{F}_b = -k_B T \frac{\nabla\phi}{\phi}, \tag{4.20}$$

when $\phi > 0$ and

$$\boldsymbol{F}_b = 0, \tag{4.21}$$

when $\phi = 0$. k_B and T are the Boltzmann constant and fluid temperature.

4.2.6 Magnetization of MDCP

The induced magnetization of a MDCP $\left(\boldsymbol{M}_{fm,p}\right)$ is related to the local magnetic field $\left(\boldsymbol{H}\right)$ produced by magnetized ferromagnetic target as given by [14, 18, 20, 23]:

$$\boldsymbol{M}_{fm,p} = 3\alpha_{fm,p}\boldsymbol{H}, \tag{4.22}$$

where $\alpha_{fm,p}$ is the demagnetization factor of the ferromagnetic material within MDCPs. If the ferromagnetic material contained in MDCPs is not magnetically saturated, $\alpha_{fm,p} = \chi_{fm,p,0}/\left(3+\chi_{fm,p,0}\right)$ and $\boldsymbol{M}_{fm,p}$ is linearly proportional to $\boldsymbol{H}$. $\chi_{fm,p,0}$ is the magnetic susceptibility of ferromagnetic material in the MDCPs at zero magnetic field. When the externally applied magnetic field is high enough the ferromagnetic material in MDCPs become magnetically saturated with $\alpha_{fm,p} = M_{fm,p,s}/3H$, where $M_{fm,p,s}$ represents the saturation magnetization of the ferromagnetic material inside the spherical MDCPs. In this case, $\boldsymbol{M}_{fm,p} = M_{fm,p,s}\hat{\boldsymbol{H}}$ where the magnitude of $\boldsymbol{M}_{fm,p}$ is constant. In this case, the magnetic force $\left(\boldsymbol{F}_m\right)$ acting on the MDCP is multiplied by the factor of one-half (due to the mathematical physics), as discussed and shown in the equations of motion in Chapter II, resulting in a substantial decrease in the magnetic force, as also obtained by Chen et al. [23].

4.2.7 Local Magnetic Field and Magnetization of the Cylindrical Target

The local magnetic field around the ferromagnetic cylindrical target located at the center of the rectangular control area is obtained through the magnetic potentials in the Laplace equation:

$$\nabla^2\varphi = 0 \tag{4.23}$$

where φ is the magnetic scalar potential. Since the regions inside and outside the wire have different properties, magnetic potentials for the inside $\left(\varphi_{in}\right)$ and outside $\left(\varphi_{out}\right)$ regions are defined separately. Thus, Eq. (4.18) becomes

$$\nabla^2\varphi_{in} = 0, \tag{4.24}$$

$$\nabla^2 \varphi_{out} = 0. \tag{4.25}$$

The respective magnetic fluxes for the inside $\left(\boldsymbol{B}_{in}\right)$ and outside $\left(\boldsymbol{B}_{out}\right)$ regions are given by

$$\boldsymbol{B}_{in} = \mu_0 \left(\boldsymbol{M}_w + \boldsymbol{H}_0 - \nabla \varphi_{in}\right), \tag{4.26}$$

$$\boldsymbol{B}_{out} = \mu_0 \left(\phi \boldsymbol{M}_{fm,p} + \boldsymbol{H}_0 - \nabla \varphi_{out}\right), \tag{4.27}$$

where $\boldsymbol{H}_0$ is the uniform externally applied magnetic field in $\hat{\boldsymbol{x}}$ direction. $\boldsymbol{M}_w$ is the induced magnetization of the ferromagnetic cylindrical target which is related to $\boldsymbol{H}_0$ through [18, 20, 23]:

$$\boldsymbol{M}_w = 2K_w \boldsymbol{H}_0, \tag{4.28}$$

where K_w is the demagnetization factor of the ferromagnetic material within the ferromagnetic target. $K_w = \chi_{w,0} / \left(2 + \chi_{w,0}\right)$ when the ferromagnetic material contained in the target is not magnetically saturated and $K_w = M_{w,s} / 2H_0$ when it becomes saturated. $\chi_{s,0}$ and $M_{s,s}$ represent the magnetic susceptibility of the ferromagnetic material in the target at zero magnetic field and the saturation magnetization of the ferromagnetic material in the target, respectively.

The local magnetic field $\left(\boldsymbol{H}\right)$ around a ferromagnetic target magnetized by $\boldsymbol{H}_0$ is given by

$$\boldsymbol{H} = \boldsymbol{H}_0 - \nabla \varphi_{out} \tag{4.29}$$

In order to solve Eqs. (4.19) and (4.20), two sets of boundary conditions for φ_{in} and φ_{out} are used. First, the magnetic potential and the normal components of the magnetic flux are both assumed to be continuous across the interface between target and fluid which are $\varphi_{in} = \varphi_{out}$ and $\hat{\boldsymbol{n}} \cdot \boldsymbol{B}_{in} = \hat{\boldsymbol{n}} \cdot \boldsymbol{B}_{out}$, respectively, where $\hat{\boldsymbol{n}}$ is normal

vector perpendicular to the surface of the cylindrical target. Seconds condition is that φ_{out} is assumed to vanish at the border of the rectangular control area.

4.3 The Mass of MDCPs Collected and the Capture Efficiency

The mass of MDCPs collected is calculated by two different methods in order to show the consistency of the results obtained by both methods. The consistency of the results also used to verify the model solutions. These two methods are the input/output mass analysis and the concentration analysis as described below.

4.3.1 The Mass of MDCPs Collected by Input/Output Mass Analysis

In the input/output (IO) mass analysis method, the mass of MDCPs collected is obtained by considering the difference between the solid (MDCPs) mass entering and leaving the control area for collection time $t-t_0$. The solid mass in the unit of mass of target entering $\left(MC_{IO,in}\right)$ and leaving $\left(MC_{IO,out}\right)$ the control area for collection time $t-t_0$ can be expressed as

$$MC_{IO,in}=\frac{\rho_p}{\pi R_w^2\rho_{fm,w}}\int_{t_0}^{t}\dot{m}_{s,in}dt, \tag{4.30}$$

and

$$MC_{IO,out}=\frac{\rho_p}{\pi R_w^2\rho_{fm,w}}\int_{t_0}^{t}\dot{m}_{s,out}dt, \tag{4.31}$$

respectively, where

$$\dot{m}_{s,in}=\int_{-w/2}^{w/2}\phi\left(x,L/2,t\right)v_{s,y,in}dx \tag{4.32}$$

and

$$\dot{m}_{s,out} = \int_{-w/2}^{w/2} \phi\left(x,-L/2,t\right) v_{s,y,out} dx. \tag{4.33}$$

$\dot{m}_{s,\mathrm{in}}$ and $\dot{m}_{s,out}$ represents the solid mass flow rates entering and leaving the control area at time t. $v_{s,y,in}$ and $v_{s,y,out}$ are the inlet and outlet solid mass velocities in the $-\hat{\boldsymbol{y}}$ direction. $\phi\left(x,L/2,t\right)$ is the particle volume fraction at the inlet of control area which is equal to ϕ_0. $\phi\left(x,-L/2,t\right)$ is the time-dependent particle volume fraction at the outlet of the control area. w and L are width and length of the rectangular control area. $\rho_{fm,w}$ is the density of the ferromagnetic cylindrical target.

The uniform external magnetic field is applied across the control area at time $t_0 = 0$ s. Then, the mass of MDCPs collected per mass of target by the IO mass analysis method $\left(MC_{IO}\right)$ can be written as

$$MC_{IO} = \frac{\rho_p}{\pi R_w^2 \rho_{fm,w}} \int_0^t \int_{-w/2}^{w/2} \left(\phi_0 v_{s,y,in} - \phi\left(x,-L/2,t\right) v_{s,y,out}\right) dxdt. \tag{4.34}$$

4.3.2 The Mass of MDCPs Collected by Concentration Analysis

By the concentration analysis (CA) method, the mass of MDCPs collected for collection time Δt is obtained by evaluating the difference between the solid mass inside the control area at time t_0 s to the time t. The solid mass in unit of mass of target inside the control area at time t_0 $\left(MC_{CA,t_0}\right)$ to the time t $\left(MC_{CA,t_0+\Delta t}\right)$ are given by

$$MC_{CA,t_0} = \frac{\rho_p}{\pi R_w^2 \rho_{fm,w}} \int_{-L/2}^{L/2} \int_{-w/2}^{w/2} \phi\left(x,y,t_0\right) dxdy, \tag{4.35}$$

And

$$MC_{CA,t_0+\Delta t} = \frac{\rho_p}{\pi R_w^2 \rho_{fm,w}} \int_{-L/2}^{L/2} \int_{-w/2}^{w/2} \phi\left(x, y, t_0 + \Delta t\right) dxdy, \tag{4.36}$$

respectively.

The uniform external magnetic field is applied across the control area at time $t_0 = 0$ s. Since $\phi\left(x, y, t_0 = 0\right)$ is ϕ_0 then the mass of MDCPs collected per mass of target $\left(MC_{IO}\right)$ by the CA for collection time t can be expressed as

$$MC_{CA} = \frac{\rho_p}{\pi R_w^2 \rho_{fm,w}} \int_{-L/2}^{L/2} \int_{-w/2}^{w/2} \left(\phi\left(x, y, t\right) - \phi_0\right) dxdy, \tag{4.37}$$

4.3.3 The Percentage Capture Efficiency

The percentage capture efficiency $\left(\%CE\right)$ as a function of collection time t is evaluated by considering the ratio of the total solid mass remained inside the control area, according to Eqs. (4.34), to the total input solid mass for collection time t, that is $\int_0^t \int_{-w/2}^{w/2} \phi_0 v_{s,y,in} dxdt$. Then, $\%CE$ can be expressed as

$$\%CE = \left(1 - \frac{\int_0^t \int_{-w/2}^{w/2} \phi\left(x, -L/2, t\right) v_{s,y,out} dxdt}{\int_0^t \int_{-w/2}^{w/2} \phi_0 v_{s,y,in} dxdt}\right) \times 100\%. \tag{4.38}$$

4.4 Results and Discussions

4.4.1 Model Conditions

The dynamic MDCP capture and accumulation around the magnetized ferromagnetic cylindrical target using the fixed rectangular control area shown in Fig 4.1 is simulated and investigated in this chapter. The ferromagnetic cylindrical target

located at the center of the rectangular control area is made of iron with radius (R_w) of 100 μm. The spherical MDCPs with average radii (R_p) of 2 μm, comprised of magnetite with 20% weight fraction and polymeric drug carrier materials with 80% weight fraction, are used. The width and length of the rectangular control area are 10 and 20 of R_w, respectively. The initial volume fraction of the MDCPs (ϕ_0) inside the control area is 0.001. The feed volume fraction of MDCPs at the inlet of the control area is also 0.001 with the average inlet fluid flow velocity $(\boldsymbol{u}_0)$ of 0.02 $\mathbf{ms}^{-1}$. The uniform externally applied magnetic field strengths $(\mu_0 H_0)$ are 0.02, 0.05, 0.1, and 0.15 T. These and all other model conditions and parameters are given in Table 4.1.

The Navier-Stokes and continuity equations according to Eqs. (4.5) - (4.6) and (4.11) - (4.12), respectively, for the solid (MDCPs) and liquid (water) phases, and the Laplace equations of the magnetic potential according to Eqs. (4.19) and (4.20) are solved simultaneously in COMSOL Multiphysics version 5.2. The corresponding solutions provides the time-dependent velocities ($\boldsymbol{v}_s$ and $\boldsymbol{v}_l$) and the volume fractions (ϕ_s and ϕ_l) of both the solid and liquid phases, as well as the local magnetic field $(\boldsymbol{H})$ through magnetic potentials for inside (φ_{in}) and outside (φ_{out}) the ferromagnetic cylindrical target. Therefore, the dynamic behaviors of MDCP capture and accumulation around the ferromagnetic cylindrical target in real-time are revealed. It is noted that when the uniform external magnetic field $(\boldsymbol{H}_0)$ is applied across the rectangular control area, its strength $(\mu_0 H_0)$ is increased smoothly from 0 T at time $t = 0$ to the final value at $t = 0.1$ s. The increase in $\boldsymbol{H}_0$ is controlled by the second derivative smooth step function in COMSOL Multiphysics version 5.2.

4.4.2 Dynamic Capture and Accumulation of MDCPs around the Ferromagnetic Cylindrical Target

Figures. 4.3(a)-(l) show the volume fraction of MDCPs collected around the iron cylindrical target and the directions of both the solid (Figs. 4.3(a), (c), (e), (g), (i) and (k)) and liquid (Figs. 3(b), (d), (f), (h), (j) and (l)) fluxes represented by trajectory lines and arrows in the case of without applying the external magnetic field (Figs. 4.3(a) and (b))

and after applying the external magnetic field of 0.15 T for 1 s (Figs. 4.3(c) and (d)), 2 s (Figs. 4.3(e) and (f)), 5 s (Figs. 4.3(g) and (h)), 10 s (Figs. 4.3(i) and (j)) and 20 s (Figs. 4.3(k) and (l)). In Figs. 4.3(a) and (b), before the external magnetic field is applied, both the solid and liquid fluxes are exactly the same because there is no magnetic force acting on MDCPs and the MDCPs in the fluid stream are dominated by the hydrodynamic force. In Figs. 4.3(c) - (l), after the external magnetic field is applied, the MDCPs in the fluid stream are affected by the magnetic force which depends on both the local magnetic field and its gradient around the magnetized iron cylindrical target as seen by Eq. (4.14). Then, the MDCPs are separated from the fluid stream under the influences of the attractive magnetic forces acting on them and finally captured by the iron target. This can be observed by the arrows of the solid fluxes around the iron target in Figs. 4.3(a), (c), (e), (g), (i) and (k). The collection zones of MDCPs continue to grow in time, which can be seen by the contour plots of volume fractions of MDCPs in Figs. 4.3(c)-(k), due to the capture and accumulation of the MDCPs around the iron cylindrical target under the influence of the magnetic force.

This dynamic model indicates that the MDCP collection zones increases with an increase in the collection time. These particle collection shapes from the model results express quite similarity to the experimental results from the literature [37, 39]. Therefore, the dynamic model in this work yields very realistic dynamic behavior of the MDCPs and particle collection zone shapes due to the capture and accumulation of MDCPs around the target.

It is noted that the MDCP collection zones only occur in certain regions, which are perpendicular to the fluid flow field, around the ferromagnetic cylindrical target. These are the magnetically attractive regions that are necessarily aligned parallel to the uniform externally applied magnetic field $\left(H_0\hat{\boldsymbol{x}}\right)$. In addition, the clean regions on the ferromagnetic cylindrical target are the magnetically repulsive regions that are naturally perpendicular to the direction of the uniform externally applied magnetic field.

In the early stages of capture process, the accumulation of MDCPs grows in the direction parallel to a uniform externally applied magnetic field $\left(H_0\hat{\boldsymbol{x}}\right)$, which is perpendicular to the fluid flow $\left(-\hat{\boldsymbol{y}}\right)$. After that, the particle accumulation cannot

continue to grow in that direction because of the weakening short-range magnetic force and the strengthening influence of hydrodynamic force due to the space narrowing between the edges of the MDCP collection zones and the walls of rectangular control area. Then, the particle collection zones continue to grow in downstream because the collection zones themselves obstructs the fluid flow resulting in the weakened hydrodynamic force in downstream of the narrowed region. This asymmetry caused by the hydrodynamic drag force pushing the MDCP collection zones in the direction of the fluid flow can be observed in Figs. 4.3(i) and (k). It is also observed and explained using the experimental results in the work of Magnet et al. [39].

The liquid phase in the fluid stream, which is not dominated by the magnetic force, travels around the MDCP collection zones instead of penetrating through them while it moves past the middle zone of the control area where the iron target is located at the center. This is due to an impermeable viscous phase with finite size forms around the iron target. The dynamic fluid viscosity, which depends on the volume fractions of MDCPs as shown in Eq. (4.25) and Fig. 4.2, increases because of an accumulation process of the MDCPs around the target. This interesting phenomenon can be seen by the directions of the liquid flux in Figs. 4.3(b), (d), (f), (h), (j) and (l).

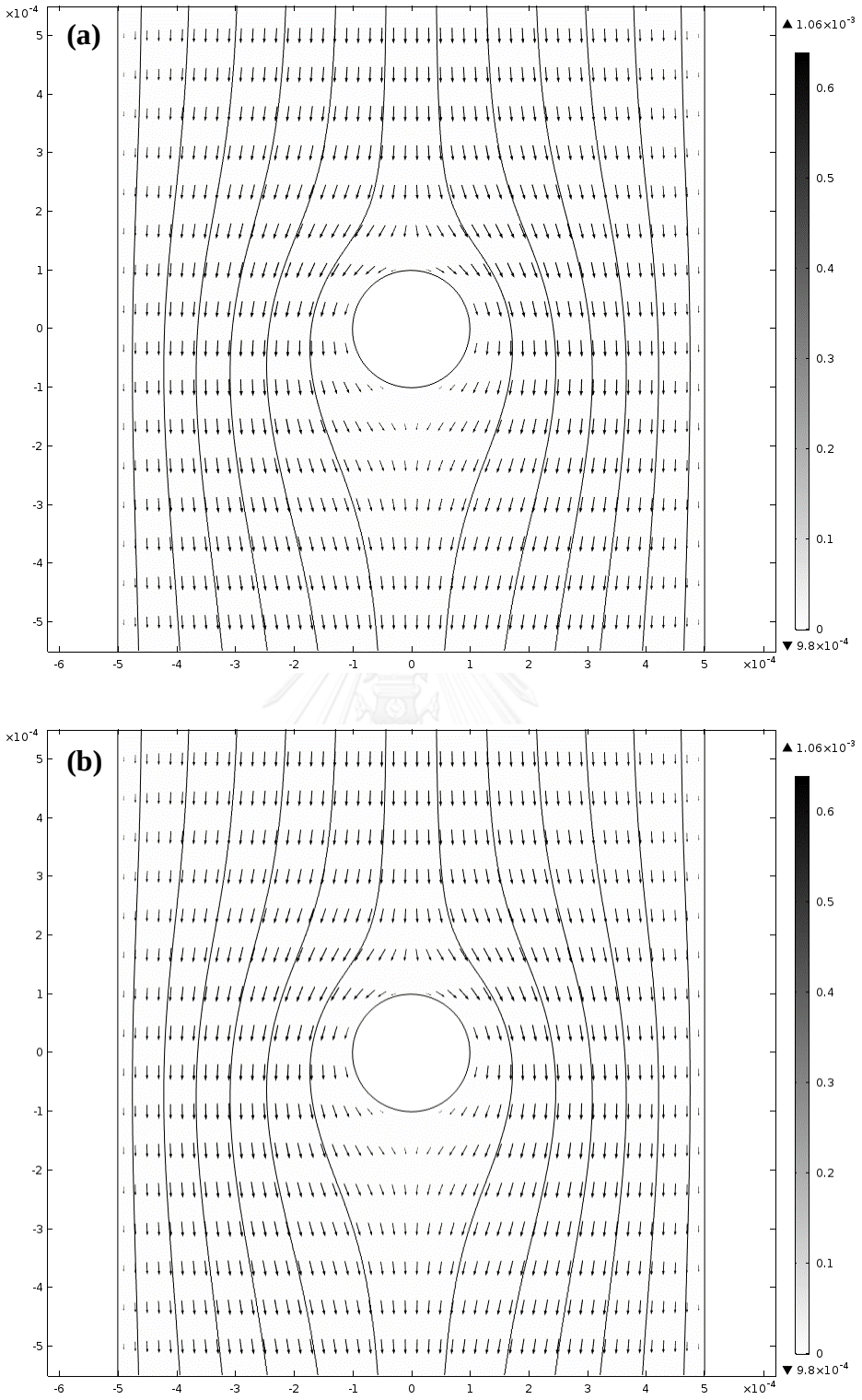

Figures 4.3(a) and (b) Contour plots of the volume fractions of MDCPs around the target and the fluxes of (a) solid and (b) liquid represented by trajectories and arrows with $\mu_0 H_0$ of 0 T are shown. The other model parameters are given in Table 4.1.

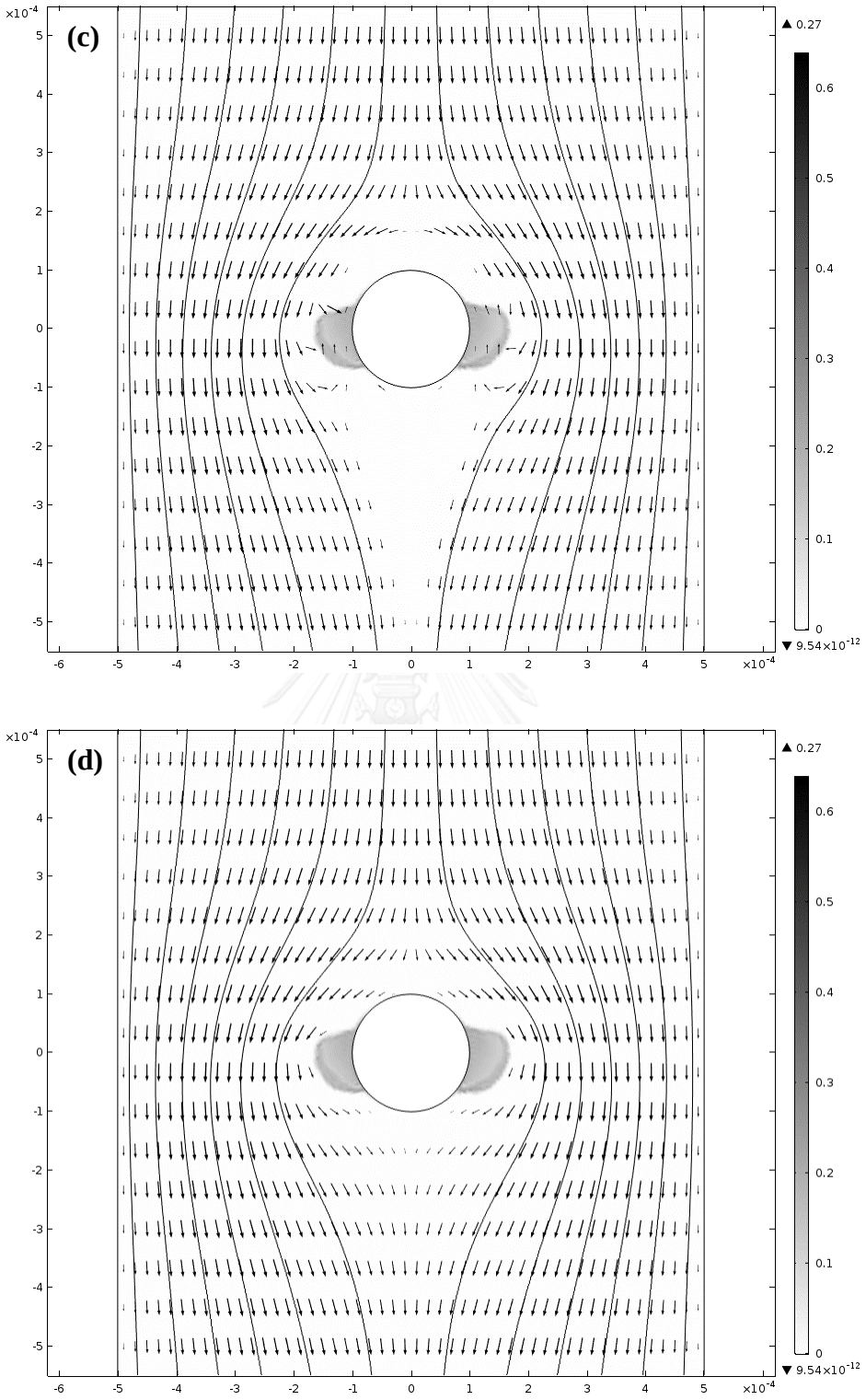

Figures 4.3(c) and (d) Contour plots of the volume fractions of MDCPs around the target and the fluxes of (c) solid and (d) liquid represented by trajectories and arrows with $\mu_0 H_0$ of 0.15 T at time t = 1 s are shown. The other model parameters are given in Table 4.1.

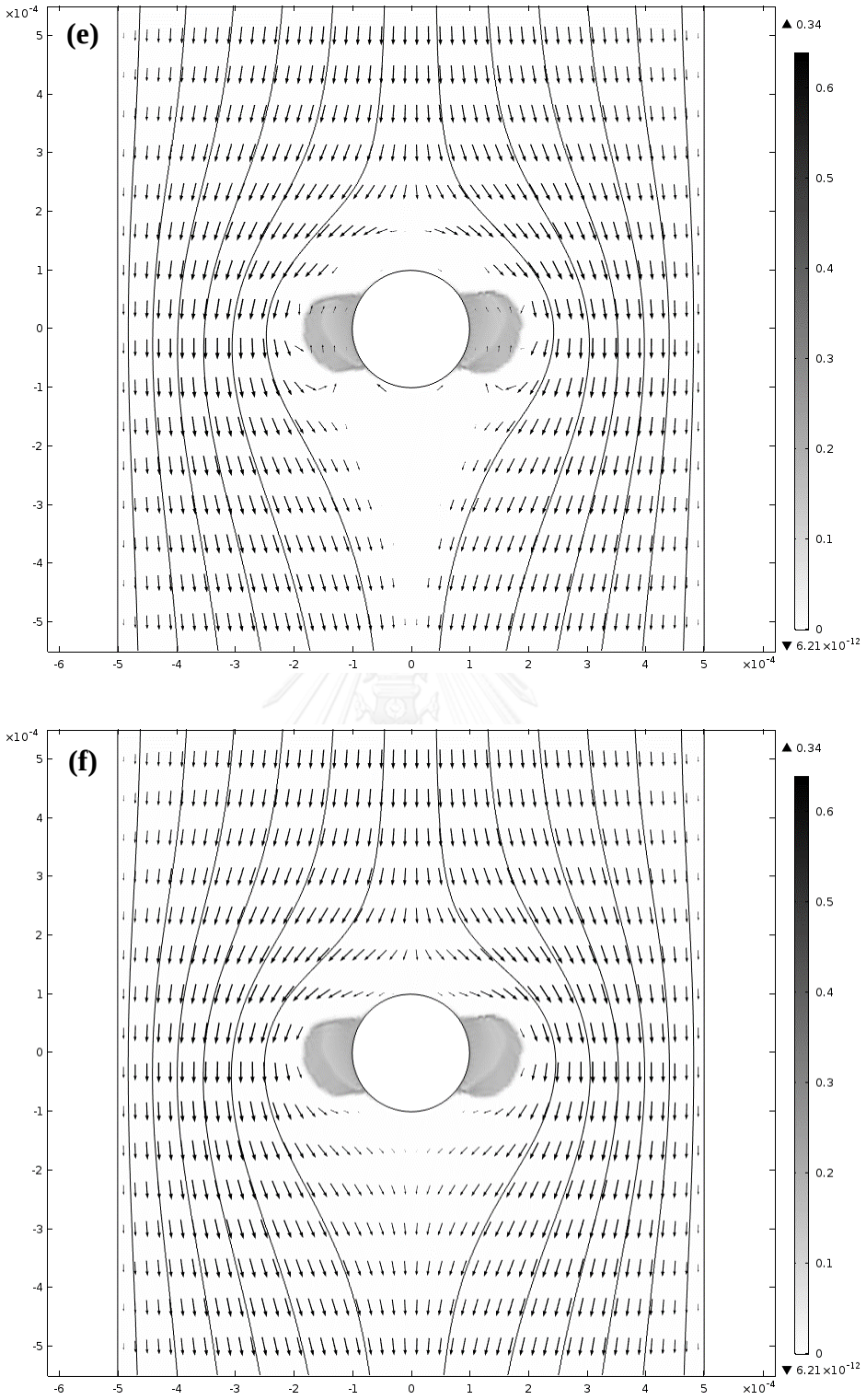

Figures 4.3(e) and (f) Contour plots of the volume fractions of MDCPs around the target and the fluxes of (e) solid and (f) liquid represented by trajectories and arrows with $\mu_0 H_0$ of 0.15 T at time t = 2 s are shown. The other model parameters are given in Table 4.1.

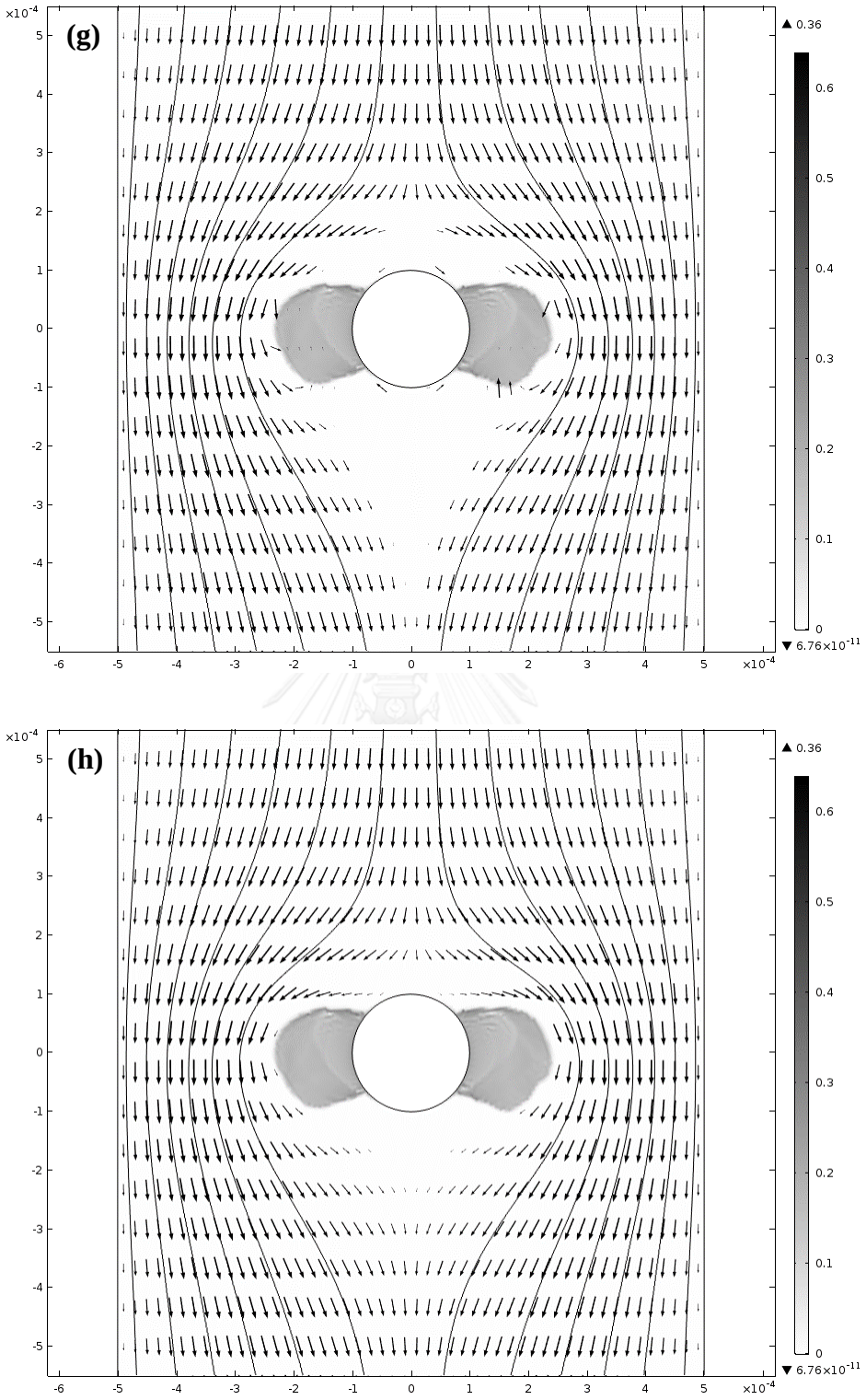

Figures 4.3(g) and (h) Contour plots of the volume fractions of MDCPs around the target and the fluxes of (g) solid and (h) liquid represented by trajectories and arrows with $\mu_0 H_0$ of 0.15 T at time t = 5 s are shown. The other model parameters are given in Table 4.1.

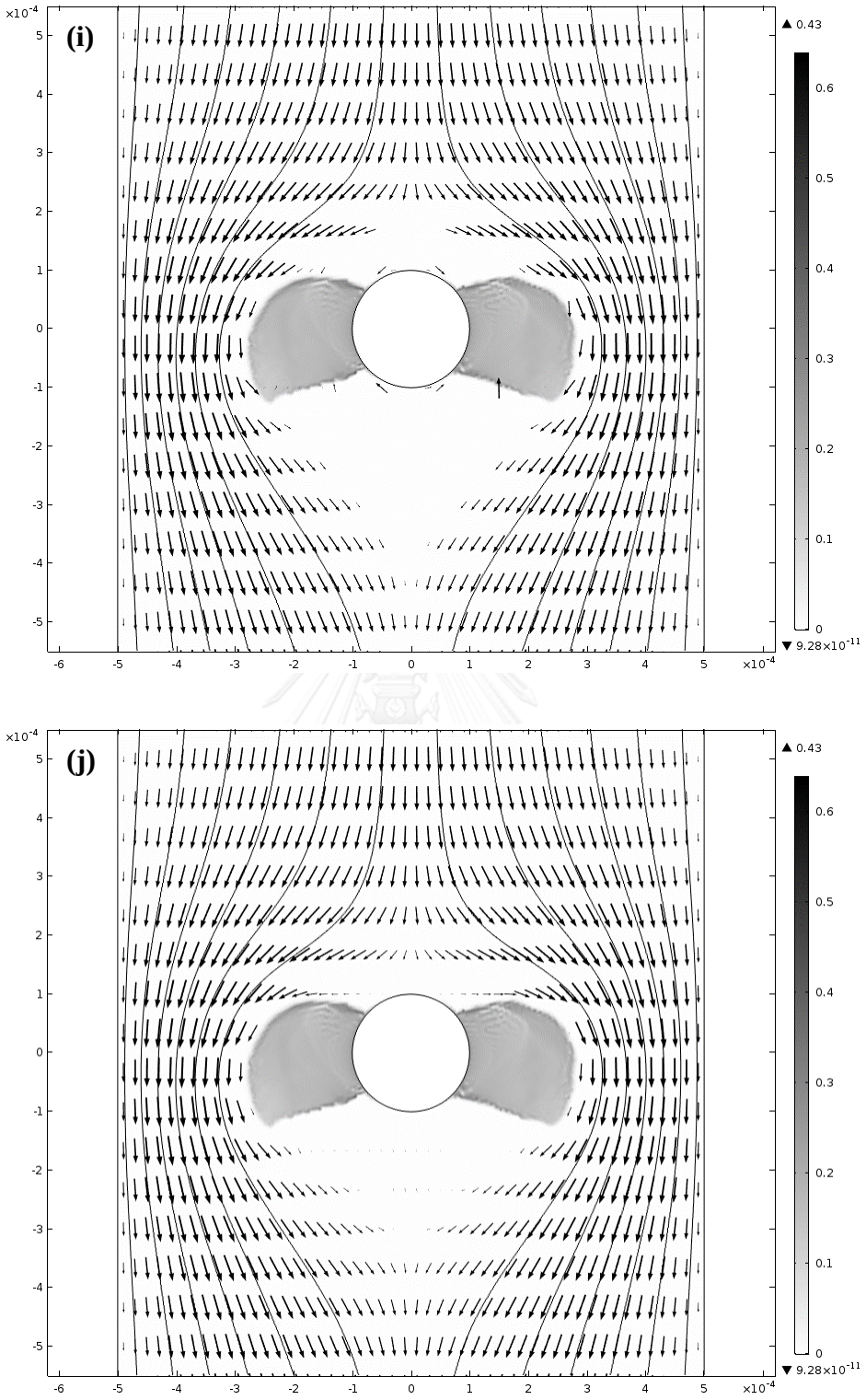

Figures 4.3(i) and (j) Contour plots of the volume fractions of MDCPs around the target and the fluxes of (i) solid and (j) liquid represented by trajectories and arrows with $\mu_0 H_0$ of 0.15 T at time t = 10 s are shown. The other model parameters are given in Table 4.1.

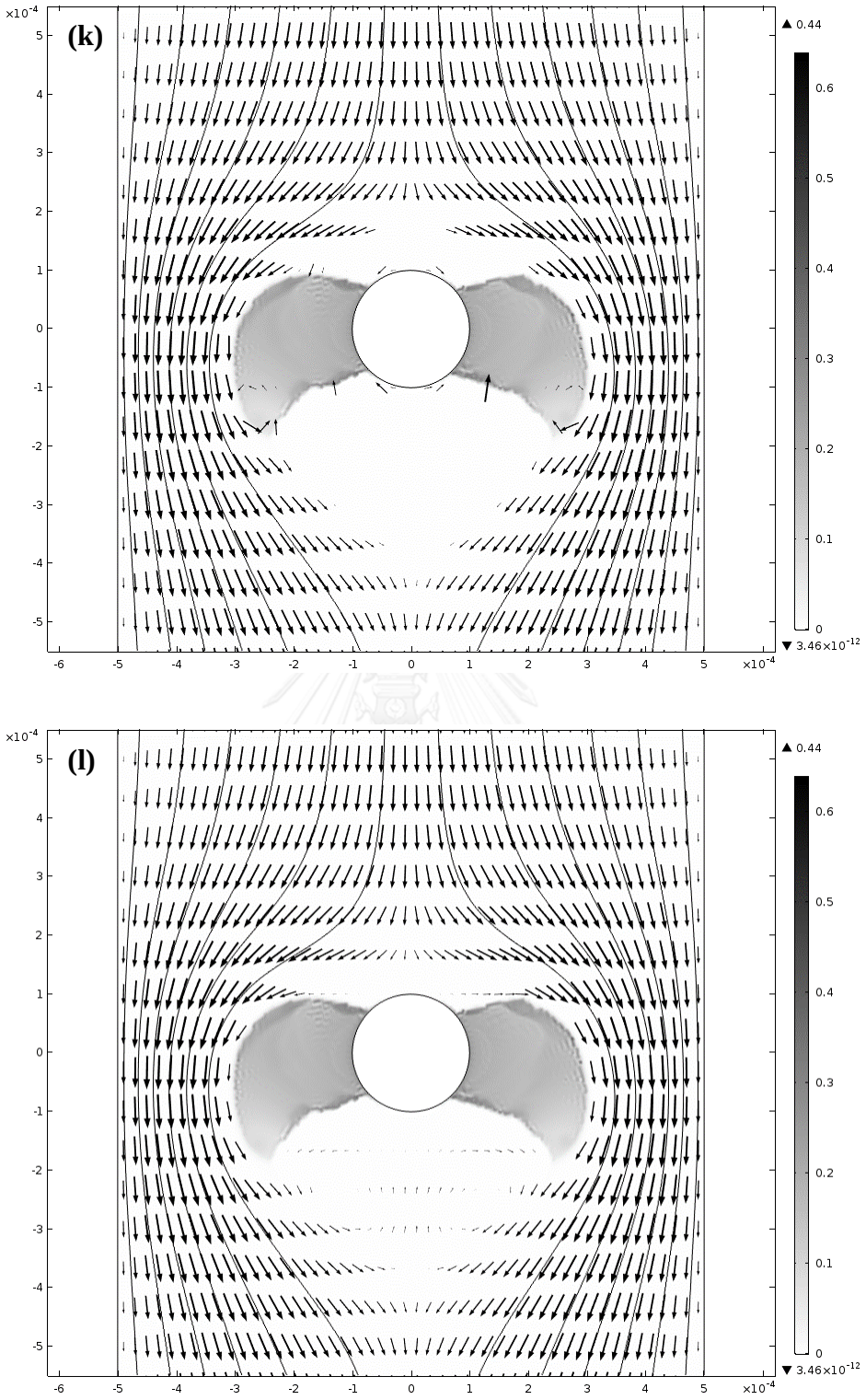

Figures 4.3(k) and (l) Contour plots of the volume fractions of MDCPs around the target and the fluxes of (k) solid and (l) liquid represented by trajectories and arrows with $\mu_0 H_0$ of 0.15 T at time t = 20 s are shown. The other model parameters are given in Table 4.1.

4.4.3 Comparison of Mass MDCPs Collected per Mass of Target Calculated by Input/Output Mass Analysis and Concentration Analysis

The comparison of the mass of MDCPs collected (MC) for $\mu_0 H_0$ of 0.15 T calculated by two different methods, which are the input/output mass analysis and concentration analysis as seen by Eqs. (4.34) and (4.37), respectively are shown in Table 4.2. The data in Table 4.2 corresponds to Figs. 4.3(b) - (k). The percentage differences of the MC between those two methods are very small. This suggests that the MC calculated by the two methods are consistent and it also verifies the model results produced by COMSOL Multiphysics version 5.2.

From the results in Table 4.2, it is seen that the MC increases when the collection time increases. The percentage mass differences in increment of collection time from 1 to 2 (1 s), 2 to 5 (3 s), 5 to 10 (5 s) and 10 to 20 s (10 s) are 86.2, 50.4, 35.0 and 18.3%, respectively. The decreasing percentage mass difference indicates that the capture ability decreases with an increase in correction time. On the other hand, the capture ability decreases with the growth of particle collection zones around the target. The is because of the influence of magnetic force decreases with distance away from the target as the collection zones grow while the influence of the hydrodynamic drag force increases in the narrow gaps between the walls of control area and the edges of the particle collection zones as discussed in the explanation of the results in Figs. 4.3(a) – (k).

Moreover, in this dynamic model, the drug dosages in the MDCP collection zones can be easily estimated through the mass of drug carrier materials collected by multiplying MC with the weight fraction of drug carrier materials inside the MDCPs $\left(1-x_{fm,p}\right)$. Therefore, in this case, the mass of drug carrier materials collected according to the MC in Table 4.2 are 7.22×10^{-3}, 1.34×10^{-2}, 2.71×10^{-2}, 4.18×10^{-2} and 5.12×10^{-2} per mass of target for collection times of 1, 3, 5, 10 and 20 s, respectively. Then, knowing the amount of the drug contained in the drug carrier materials inside the MDCPs provides the delivered drug dose to the target site.

The comparison of mass of MDCP collected per mass of target (MC) between the IO mass analysis and CA methods, as seen by Eqs. (4.34) and (4.37), respectively, for $\mu_0 H_0$ of 0.05 T and the collection time of 20 s are shown in Fig. 4.4. The results also reveal the consistency of the solutions obtained by two methods and verify the model solutions as same as the results in Table 4.2.

The MC increase with large slope at the early stages of the capture process $(t<10)$, then the slopes of MC decrease dramatically at the latter stages of the capture process. This suggests that the capture ability decreases as time increases and it finally approaches to zero at infinite time. Because the edges of collection zone, which are the areas that the MDCPs are captured from the fluid stream, are away from the target due to the expansions of the collection zones with an increase in time where the magnetic force is weak and cannot capture more MDCPs, as already described.

Table 4.2 Comparison of mass of MDCPs collected per mass of target (MC) calculated by the input/output (IO) mass analysis and concentration analysis (CA) for $\mu_0 H_0$ of 0.15 T. The data correspond to Figs 3.2(b) to 3.2 (f). The other parameters are given in Table 4.1.

Collection Time	**Mass of MDCPs Collected per Mass of Target**		**%**
t **(s)**	**IO Mass Analysis**	**CA**	**Difference**
1	9.028×10^{-3}	9.037×10^{-3}	0.098
2	1.681×10^{-2}	1.682×10^{-2}	0.055
5	3.390×10^{-2}	3.389×10^{-2}	0.021
10	5.224×10^{-2}	5.223×10^{-2}	0.020
20	6.396×10^{-2}	6.411×10^{-2}	0.224

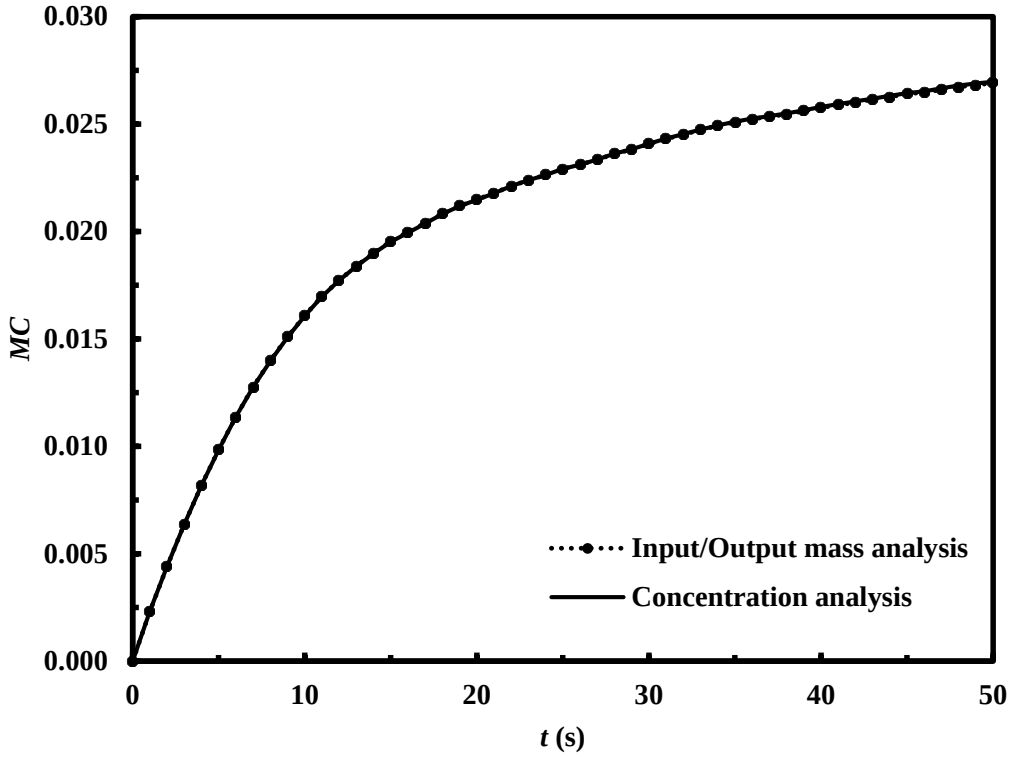

Figure 4.4 Comparison of the mass of MDCPs collected per mass of target (MC) calculated by the input/output mass analysis and concentration analysis as a function of collection time t with $\mu_0 H_0$ of 0.05 T. The other model parameters are given in Table 4.1.

4.4.4 The Breakthrough Curves of the Normalized Output Solid Mass Flow Rates

Figures. 4.5(a) and (b) show the dynamic breakthrough curves of the normalized output solid mass flow rates for various $\mu_0 H_0$ as a function of time after applying the uniform external magnetic field. The normalized output solid mass flow rate is defined by the ratio of the solid mass flow rate leaving to that entering the control area, that is $\dot{m}_{s,out}/\dot{m}_{s,in}$, where $\dot{m}_{s,in}$ and $\dot{m}_{s,out}$ are defined by Eqs. (4.32) and (4.33), respectively.

Before the magnetic field is applied across the control area in order to magnetize the target, the initial volume concentration of MDCPs $\phi(t=0)$ in the fluid stream within the rectangular control area is uniform and equal to the concentration being fed to the control area at the inlet at all times, that is ϕ_0 of 0.001. The external magnetic field is applied to magnetize the target at $t=0$ s and then smoothly increases until the final value is reached at $t=0.1$ s. These operational scenarios affect the changes in these breakthrough curves which is described below.

In Figs. 4.5(a) and (b), all breakthrough curves begin with $\dot{m}_{s,out}/\dot{m}_{s,in}$ of 1.0 at $t=0$ s. The $\dot{m}_{s,out}/\dot{m}_{s,in}$ stay at 1.0 for a very short period of time then it decreases dramatically to a minimum. After that, $\dot{m}_{s,out}/\dot{m}_{s,in}$ increases gradually and finally approaches to 1.0 at infinite time which means that $\dot{m}_{s,in}$ and $\dot{m}_{s,out}$ are equal then none of MDCPs is captured from the fluid stream. The trends of $\dot{m}_{s,out}/\dot{m}_{s,in}$ are more pronounced with an increase in $\mu_0 H_0$. This interesting dynamic behavior observed in the breakthrough curves is chromatographic-type effect. It should be noted that the retention time for the fluid to pass through the control area is 0.1 s. This explains that the $\dot{m}_{s,out}/\dot{m}_{s,in}$ is 1.0 at the early collection time ($t \leq$ about 0.05 s) before the breakthrough curves begin to drop down because the retention time associated with the fluid at downstream of the ferromagnetic target containing an initial uniform volume concentration of MDCPs that must leave the control area at the outlet before the chromatographic effect is observed. In other words, all of the MDCPs within the fluid that stays at downstream of the magnetized target escape the effect of high gradient magnetic field. After that, $\dot{m}_{s,out}/\dot{m}_{s,in}$ begins to drop, as expected, due to the next quantity of the fluid that is leaving the rectangular control area, which is closest to the target, is depleted of some of the MDCPs because of the strong magnetic force acting on the MDCPs creating a significant MDCP build-up on the target surface. The $\dot{m}_{s,out}/\dot{m}_{s,in}$ continues to drop as the fluid passes the magnetized target due to additional accumulation of MDCPs on the target until the minimums in the $\dot{m}_{s,out}/\dot{m}_{s,in}$ are reached, which occurs within about 0.1 to 0.3 s. The minimums of breakthrough curves occur at $\dot{m}_{s,out}/\dot{m}_{s,in}$ of 0.987, 0.961, 0.910 and 0.855 at 0.276, 0.170, 0.141 and 0.120 s for $\mu_0 H_0$ = 0.02, 0.05, 0.10 and 0.15 T, respectively. This initial and rapid drop

of breakthrough curves exhibit because of the dominance of the magnetic force acting on the MDCPs over the hydrodynamic force locally around the target at initial collection time. Then, the breakthrough curves begins to increase because of the strengthening of the hydrodynamic force and the weakening of the magnetic force as the collection zones grow, consequently resulting in no further MDCP accumulation at infinite times. This is when $\dot{m}_{s,out}/\dot{m}_{s,in}$ reaches 1.0 and the target is completely saturated with the MDCPs therefore no more MDCPs are captured within the control area.

4.4.5 The Mass of MDCPs Collected Per Mass of the Cylindrical Target

The mass of MDCPs collected (MC) as a function of collection time (t) for various cases of $\mu_0 H_0$ are shown in Fig 4.6. The general behavior of MC is the same as that already described in the explanation of Fig 4.4. MC increases as both $\mu_0 H_0$ and t increases. The changes in MC with an increment of $\mu_0 H_0$ by 0.05 T from 0 to 0.15 T at t = 20 s are 2.15×10^{-2} (from 0 T to 0.05 T), 2.33×10^{-2} (from 0.05 T to 0.1 T) and 1.92×10^{-2} (from 0.1 T to 0.15 T), respectively. This suggests that the capture ability increases with an increase in uniform externally applied magnetic field strength for $\mu_0 H_0 \leq$ 0.1 T and it decreases with a further increase in uniform externally applied magnetic field strength between 0.1 T < $\mu_0 H_0$ ≤ 0.15 T. This may be due to the effects of both accumulation of MDCPs on the target surface and the saturation magnetization of the ferromagnetic material inside MDCPs.

The magnetization of magnetite inside the MDCPs becomes magnetically saturated when magnetite experiences a magnetic field larger than 0.19 T. After the saturation of magnetite MDCP, the magnetic forces acting on the MDCPs are reduced, as discussed in the Theory and Chapter II, resulting in a reduction of the capture ability of the target. Moreover, the MDCP collection zones increase with an increase in $\mu_0 H_0$ which also reduces the capture ability as explained previously by the strengthening hydrodynamic and weakening magnetic forces.

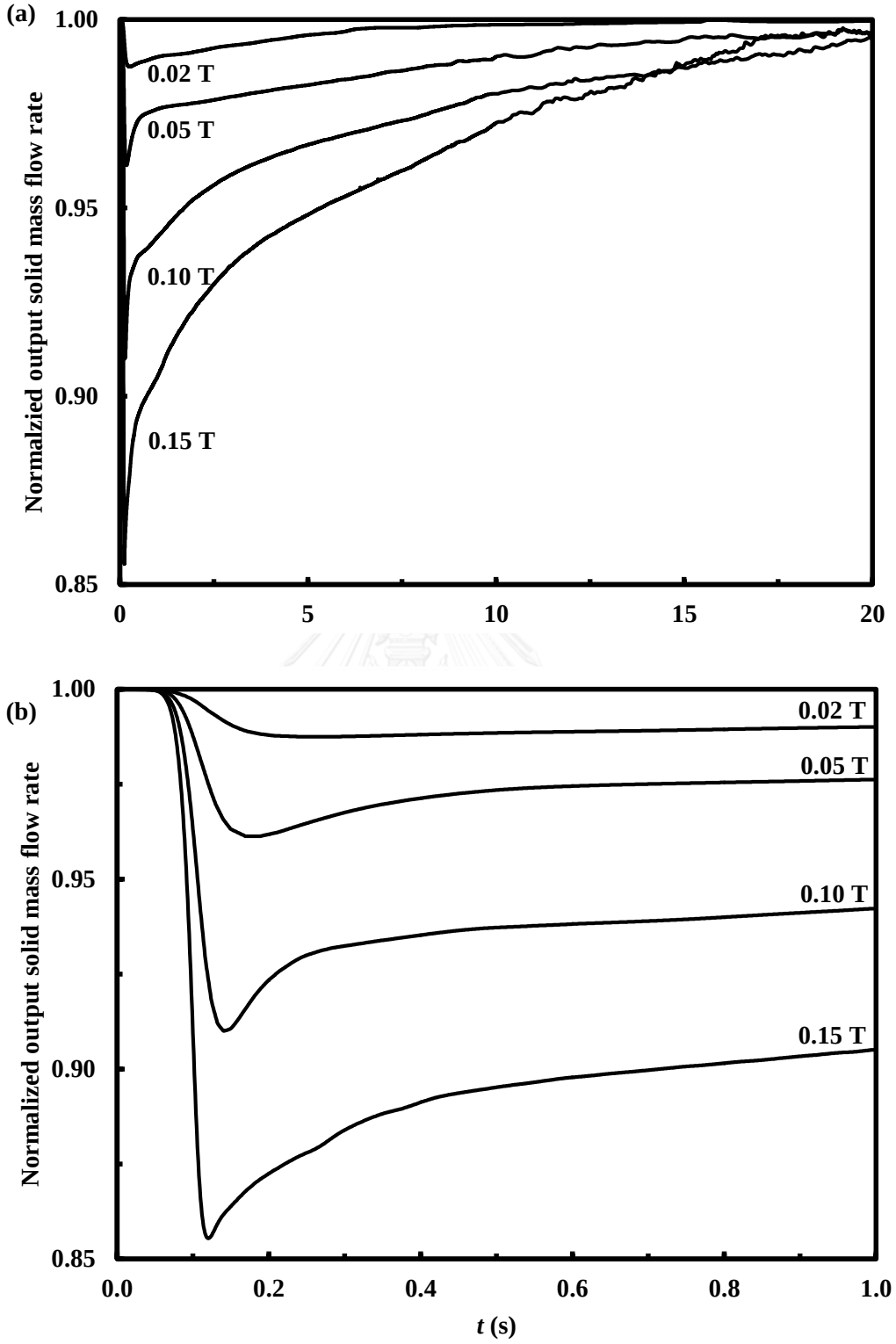

Figure 4.5(a) and (b) Breakthrough curves of the normalized output solid mass flow rate as a function of collection time t between (a) 0 to 20 s and (b) 0 to 1 s for different $\mu_0 H_0$. The other models parameters are given in Table 4.1.

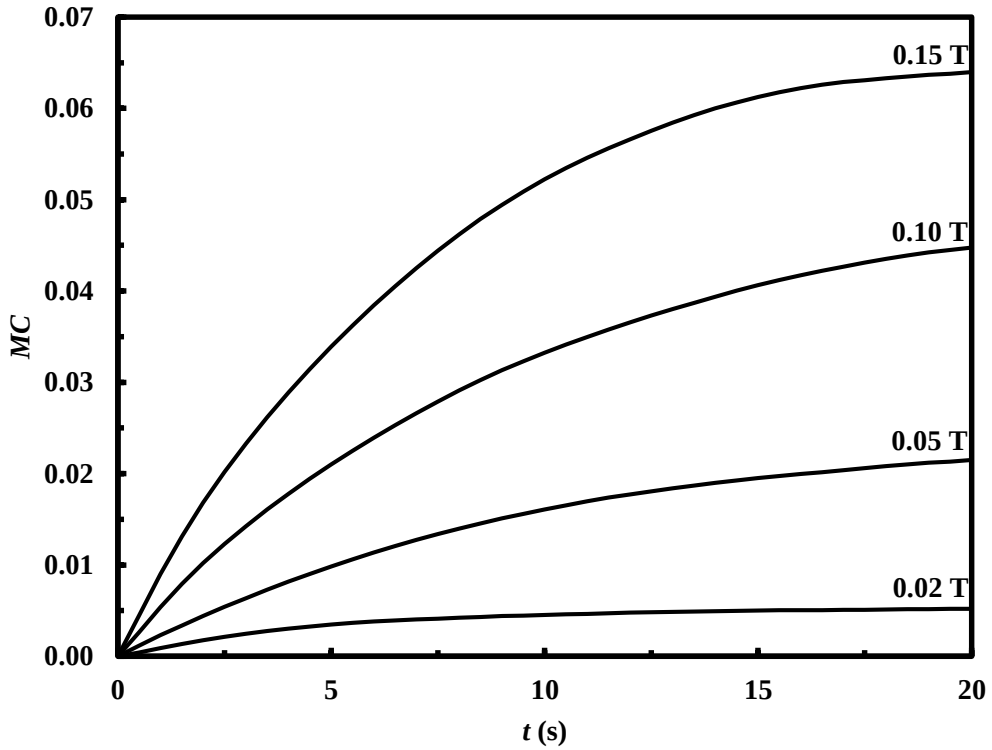

Figure 4.6 The mass of MDCPs collected per mass of target (MC) as a function of collection time t for different $\mu_0 H_0$. The other parameters are given in Table 4.1.

4.4.6 The Percentage Capture Efficiencies

The percentage capture efficiencies $(\%CE)$ as a function of collection time (t) for various $\mu_0 H_0$ are shown in Fig. 4.7**.** The solid and dashed lines represent the $\%CE$ evaluated from the dynamic model in this chapter and the trajectory model described in the Appendix E [56] which is used in Chapter II and III. The trends of $\%CE$ between both models are qualitatively consistent that is decreasing $\mu_0 H_0$ resulting in smaller $\%CE$. However, all of the $\%CE$ curves predicted from the dynamic model at different $\mu_0 H_0$ show a maximum, while those from the trajectory model are all constant in time, as expected. The maximum $\%CE$ predicted from the dynamic model are closest to the constant $\%CE$ predicted from the trajectory model. This is

very interesting and it suggests that the $\%CE$ predicted from the trajectory model are close to those from the dynamic model, which is more accurate, only at a short period of collection times when the accumulation of MDCPs is still low (early stages of capture process) resulting in making the assumption of the clean target more valid. This simulation result verifies that the clean target model, which is used in trajectory analysis, is applicable only at the very early stages of the MDCP capture process.

The errors between the maximum $\%CE$ predicted by the dynamic model and the $\%CE$ predicted by the trajectory model are 21.0, 43.1, 47.6 and 9.5 % for $\mu_0 H_0$ of 0.02, 0.05, 0.10 and 0.15 T, respectively. For $\mu_0 H_0 \leq$ 0.10 T, the errors increase with increasing $\mu_0 H_0$ but then the error dramatically decreases at $\mu_0 H_0$ of 0.15 T. This can be caused by the effect of saturation magnetization of the ferromagnetic materials in MDCPs. In both models, a reduction in the $\%CE$ occurs when the magnetite inside the MDCPs become magnetically saturated. The maximum $\%CE$ from the dynamic model increases by a factor of 1.68 from $\mu_0 H_0$ of 0.1 to 0.15 T, but it increases by only a factor of 1.35 for the trajectory model. This suggests that the capture efficiency of the trajectory model is reduced more by the effect of saturation magnetization of the ferromagnetic materials in MDCPs compared to that of the dynamic model, which reduces the error in $\%CE$ between the dynamic and trajectory models.

The $\%CE$ curves predicated from the dynamic model provide the maxima due to the chromatographic-type effect as described in the explanation of Fig. 4.5. The corresponding strengthening hydrodynamic and weakening magnetic forces after the maxima reveal their effects in terms of the changes of $\%CE$ in time. For $\mu_0 H_0$ of 0.15 T, the maximum $\%CE$ is 9.85 at t = 0.8 s and it drops to 3.48 at t = 20 s. That is the $\%CE$ reduced by 64.7% from its maximum within only about 19 s. In fact, all of the $\%CE$ curves go to zero at infinite time that is when the MDCPs in the fluid stream are no longer captured by the magnetized cylindrical target. The decrease in the capture efficiency with an increase in collection time predicted from the dynamic model corresponds to a realistic situation, while the steady-state solutions predicted from the trajectory model cannot predict this behavior. The dramatic decrease in the capture

efficiency as the accumulation of MDCPs increases is also revealed in the work of Chen et al. [35].

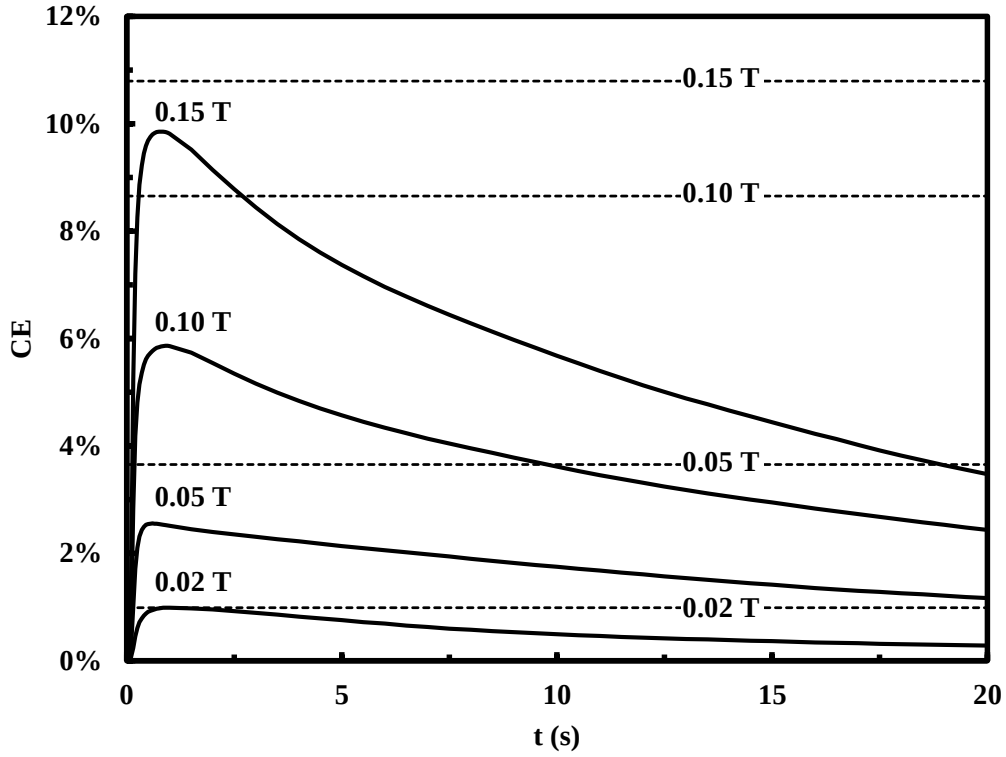

Figure 4.7 The capture efficiency $(\%CE)$ as a function of collection time t for different $\mu_0 H_0$. The solid lines with symbols are from the dynamic model. The dashed lines are from the trajectory model. The other parameters are given in Table 4.1.

4.4.7 Inclusion and Exclusion the Effect of MDCP Magnetization

The fluid and MDCP fluxes and the volume fraction of MDCPs around the magnetized cylindrical target at time t = 10 s, the breakthrough curves, the mass of MDCP collected curves and the percentage capture efficiency for $\mu_0 H_0$ of 0.05 and 0.15 T with different cases of MDCP magnetization effect are shown in Figs. 4.8, 4.9, 4.10 and 4.11, respectively. The first case considers the effect of magnetization of the MDCPs in the collection zones and the fluid stream on the local magnetic field. This is the more realistic case that is considered in all the previous results. The second case does not consider the effect of magnetization of the MDCPs in the collection zones and the fluid stream on the local magnetic field. This is done by simply removing the first term in the right hand side of Eq. (4.22), that is $\phi \boldsymbol{M}_{fm,p}$. Then, Eq. (4.22) becomes $\boldsymbol{B}_{out} = \mu_0 \left(\boldsymbol{H}_0 - \nabla \varphi_{out} \right)$. The interesting results in Figs. 4.8 - 4.11 reveal that the collection zones are smaller when the magnetization of MDCPs contributes to the magnetic field around the magnetized iron target. On the other hand, when the magnetization of the MDCPs is included in the dynamic model the MDCPs are captured and accumulated less than that compared to when it is excluded from the model. This is an expected result from the dynamic model in this chapter which the more explanation is given further with the results in Fig 4.12 - 4.14.

Moreover, Fig. 4.8 also shows very clearly that the significant effect of the uniform externally applied magnetic field strength on the shape and size of the collection zones. Increasing the uniform externally applied magnetic field strength from 0.05 to 0.15 T does not only provide more MDCP capture and accumulation, but it also causes the shape of the collection zone to change. This is true whether MDCP magnetization is included or excluded in the dynamic model.

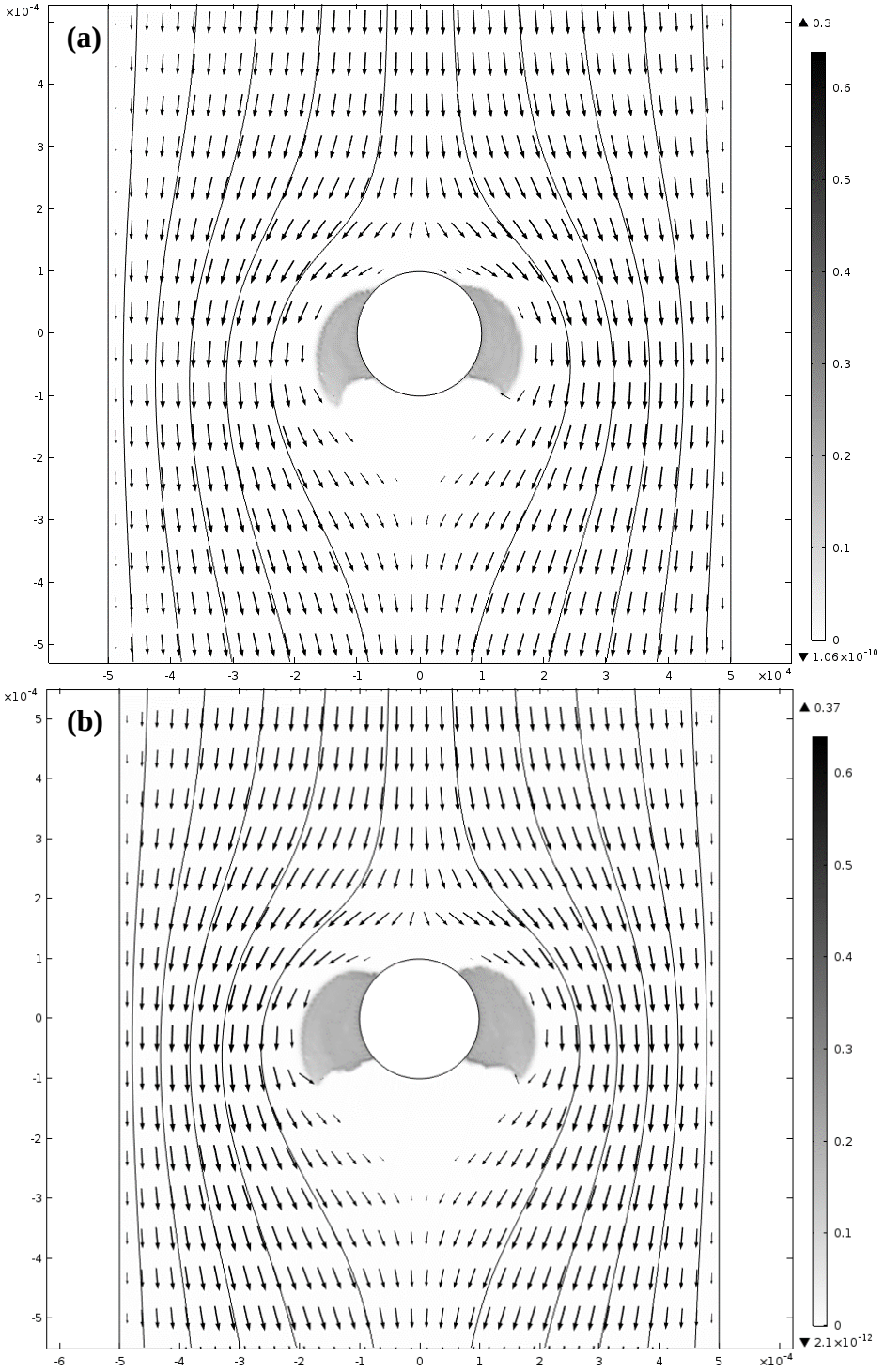

Figure 4.8(a) and (b) Contour plots of the volume fractions of MDCPs around the target and the fluxes of solid represented by trajectories and arrows when (a) including and (b) excluding the effect of the MDCPs on the magnetic field with $\mu_0 H_0$ of 0.05 T at t = 10 s. The other parameters are given in Table 4.1.

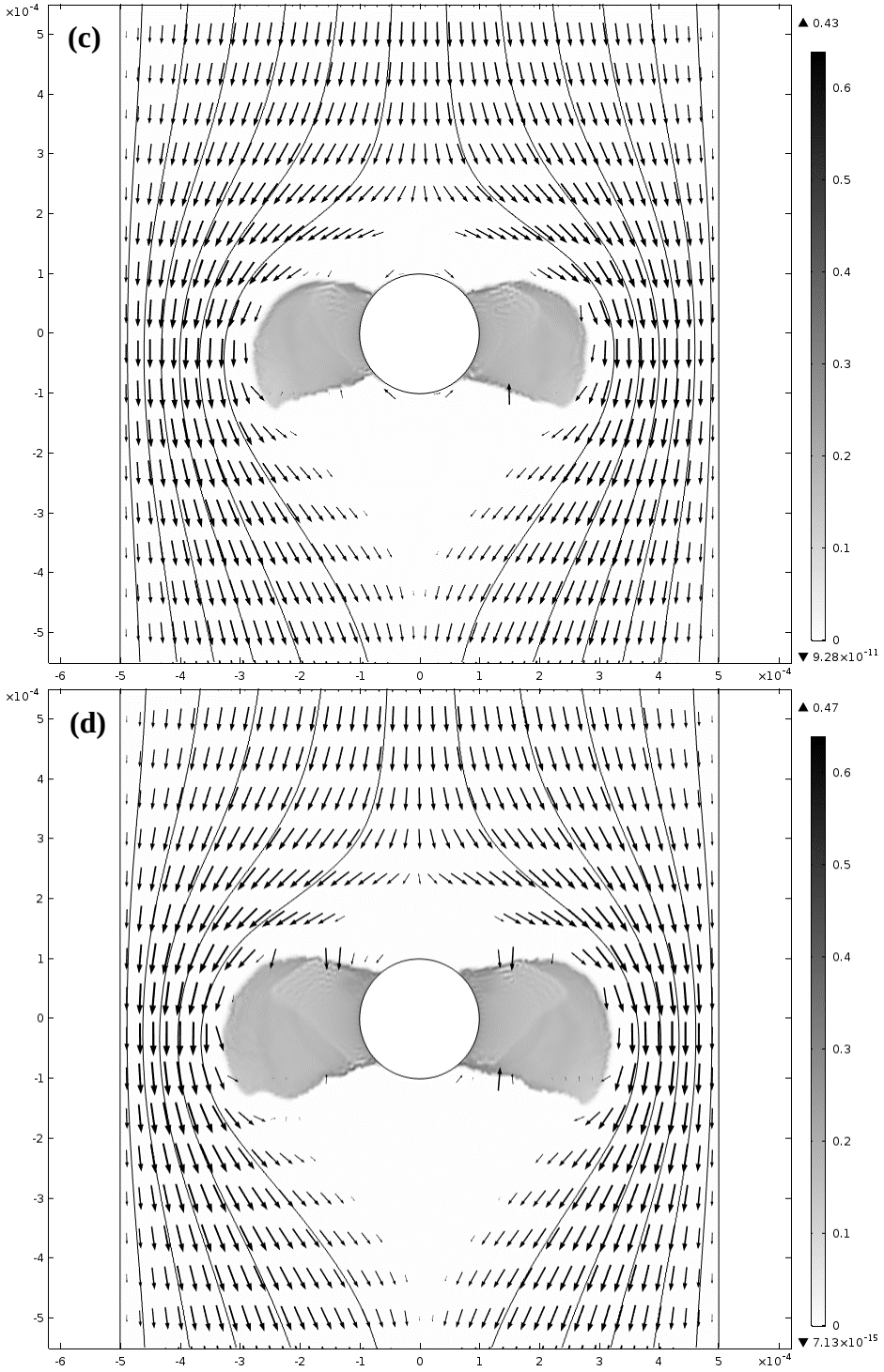

Figure 4.8(c) and (d) Contour plots of the volume fractions of MDCPs around the target and the fluxes of solid represented by trajectories and arrows when (c) including and (d) excluding the effect of the MDCPs on the magnetic field with $\mu_0 H_0$ of 0.15 T at t = 10 s. The other parameters are given in Table 4.1.

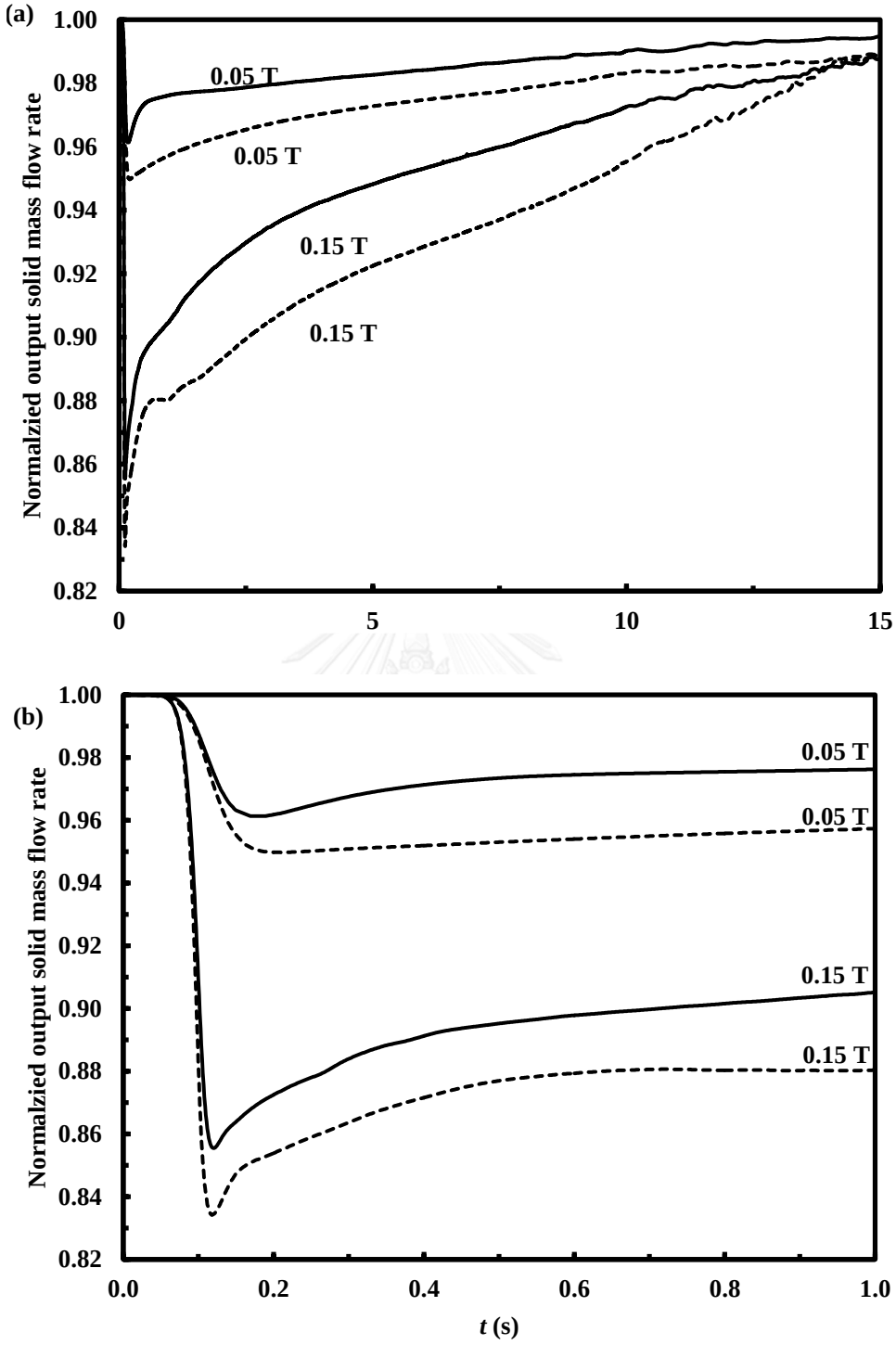

Figure 4.9 Breakthrough curves of the normalized output solid mass flow rate as a function of collection time t between (a) 0 and 15 s and (b) 0 and 1 s for different $\mu_0 H_0$ when including (solid lines) and excluding (dashed lines) the effect of the MDCPs on the magnetic field. The other parameters are given in Table 4.1.

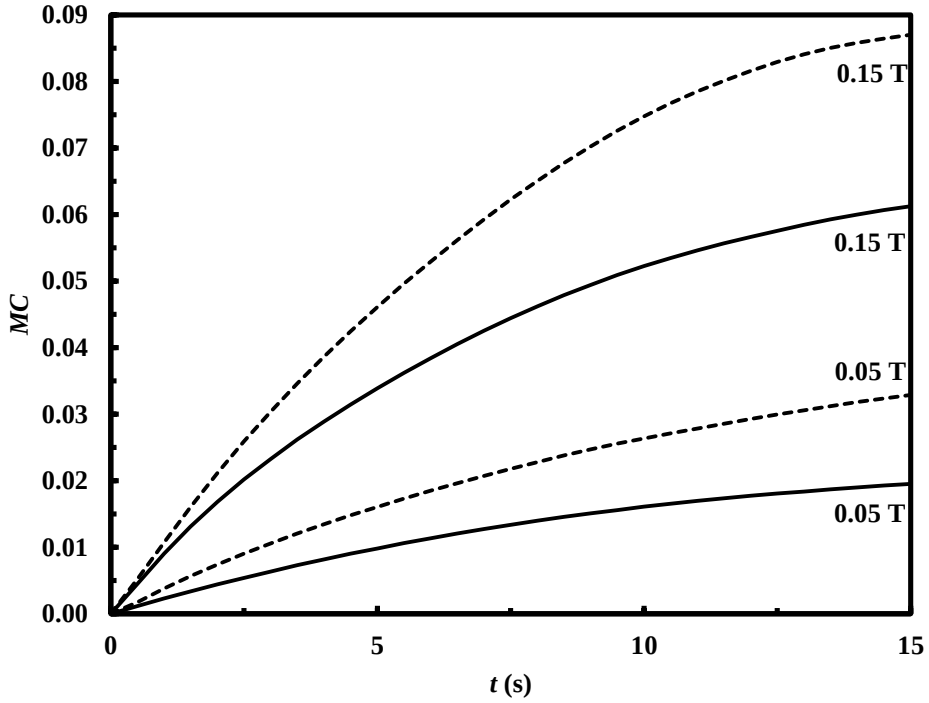

Figure 4.10 Mass of MDCPs collected per mass of target (MC) as a function of collection t for different $\mu_0 H_0$ when including (solid lines) and excluding (dashed lines) the effect of the MDCPs on the magnetic field. The other parameters are given in Table 4.1.

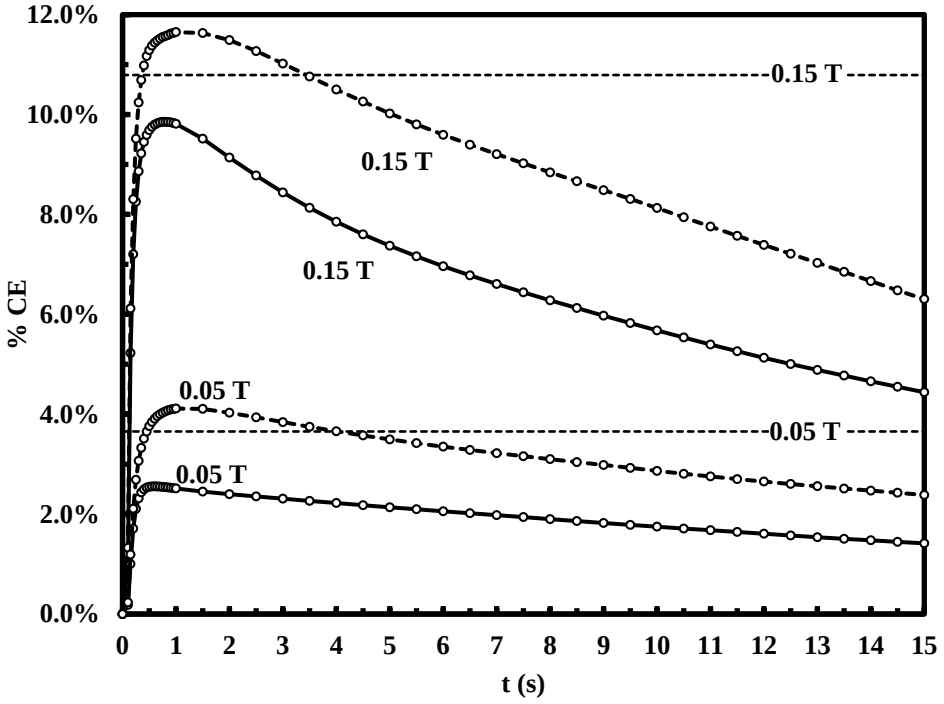

Figure 4.11 Mass of MDCPs collected per mass of target (MC) as a function of collection time t for different $\mu_0 H_0$ when including (solid lines) and excluding (dashed lines) the effect of the MDCPs on the magnetic field. The other parameters are given in Table 4.1.

4.4.8 Contour Plots of the Local Magnetic Field Strength $(\mu_0 H_f)$, Radial Gradient of H_f $(\partial H_f / \partial r)$ and the Magnetic Force (F_m) around the Target

The contour plots of the local magnetic field strength $(\mu_0 H_f)$, the radial gradient of H_f $(\partial H_f / \partial r)$ and the magnitude of magnetic force (F_m) around the magnetized cylindrical target at time t = 10 s and $\mu_0 H_0$ of 0.05 T are shown in Figs. 4.12, 4.13 and 4.14, respectively. The effect of MDCP magnetization, that is the effect of the MDCPs on the local magnetic field around the iron target, is included in the model for Figs. 4.12 - 4.14 case (a), and it is excluded from the model for Figs. 4.12 -

4.14 case (b). The results clearly reveals that the magnetization of the MDCPs around the target significantly reduces the $\mu_0 H_f$, $\partial H_f / \partial r$ and F_m around the magnetized cylindrical target. With magnetic flux being continuous across the target-fluid interface, that is $\boldsymbol{B}_1$ from Eq. (4.21) is equals to $\boldsymbol{B}_2$ from Eq. (4.22), this effect is manifested through the decrease in the magnetic flux around the target when including the effect of magnetization of MDCPs in the model. The decrease in magnetic flux in this case effectively decreases the attractive regions around the magnetized target and the collection zones, therefore the smaller collection zones are created instead, as observed in Fig. 4.8, resulted in smaller MC and $\%CE$ as shown in Figs. 4.9 - 4.11.

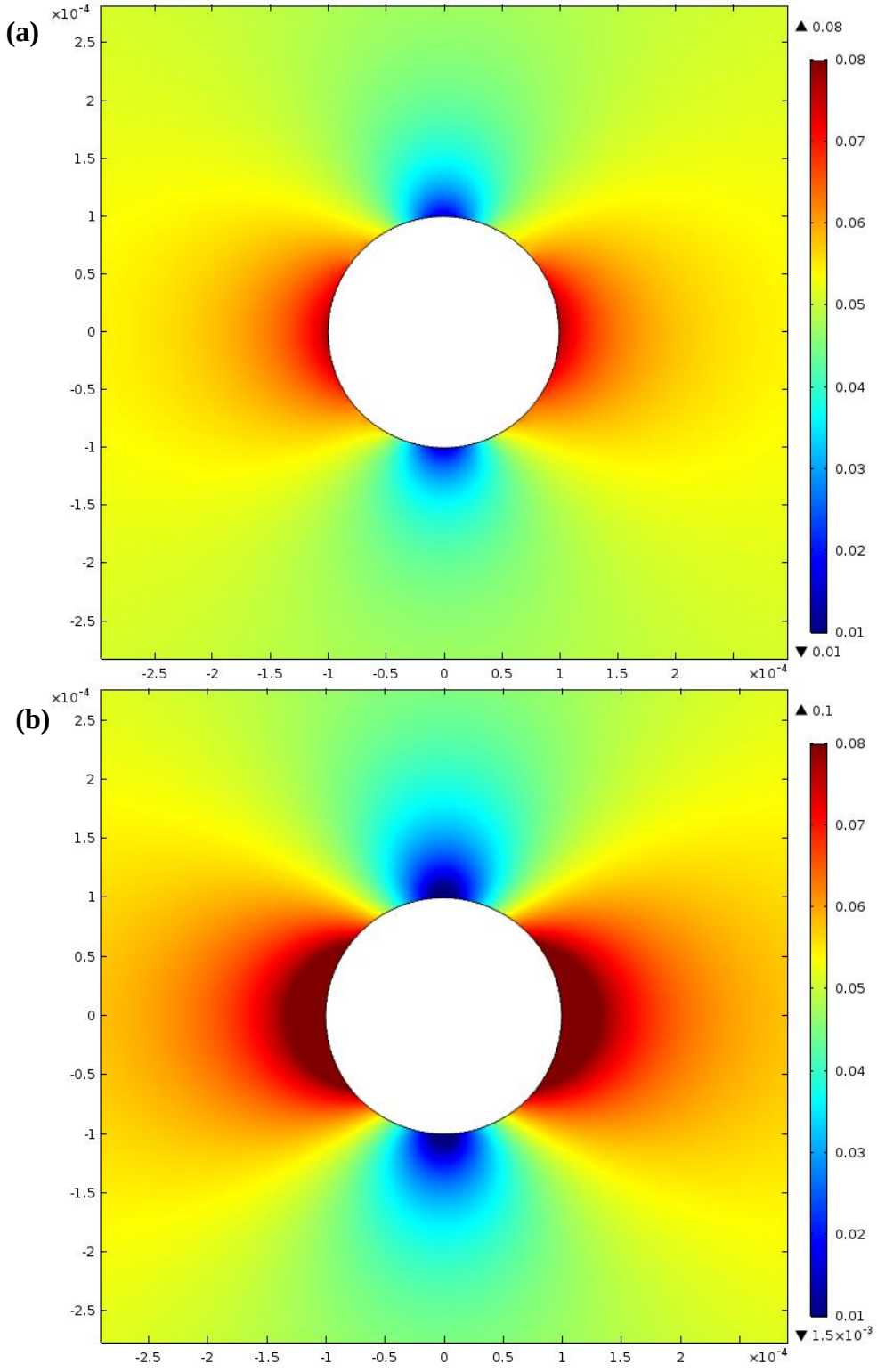

Figure 4.12 Contour plots of $\mu_0 H_f$ around the cylindrical target when (a) including and (b) excluding the effect of the MDCPs on the magnetic field with $\mu_0 H_0$ = 0.05 T at t = 10 s. The other parameters are given in Table 4.1.

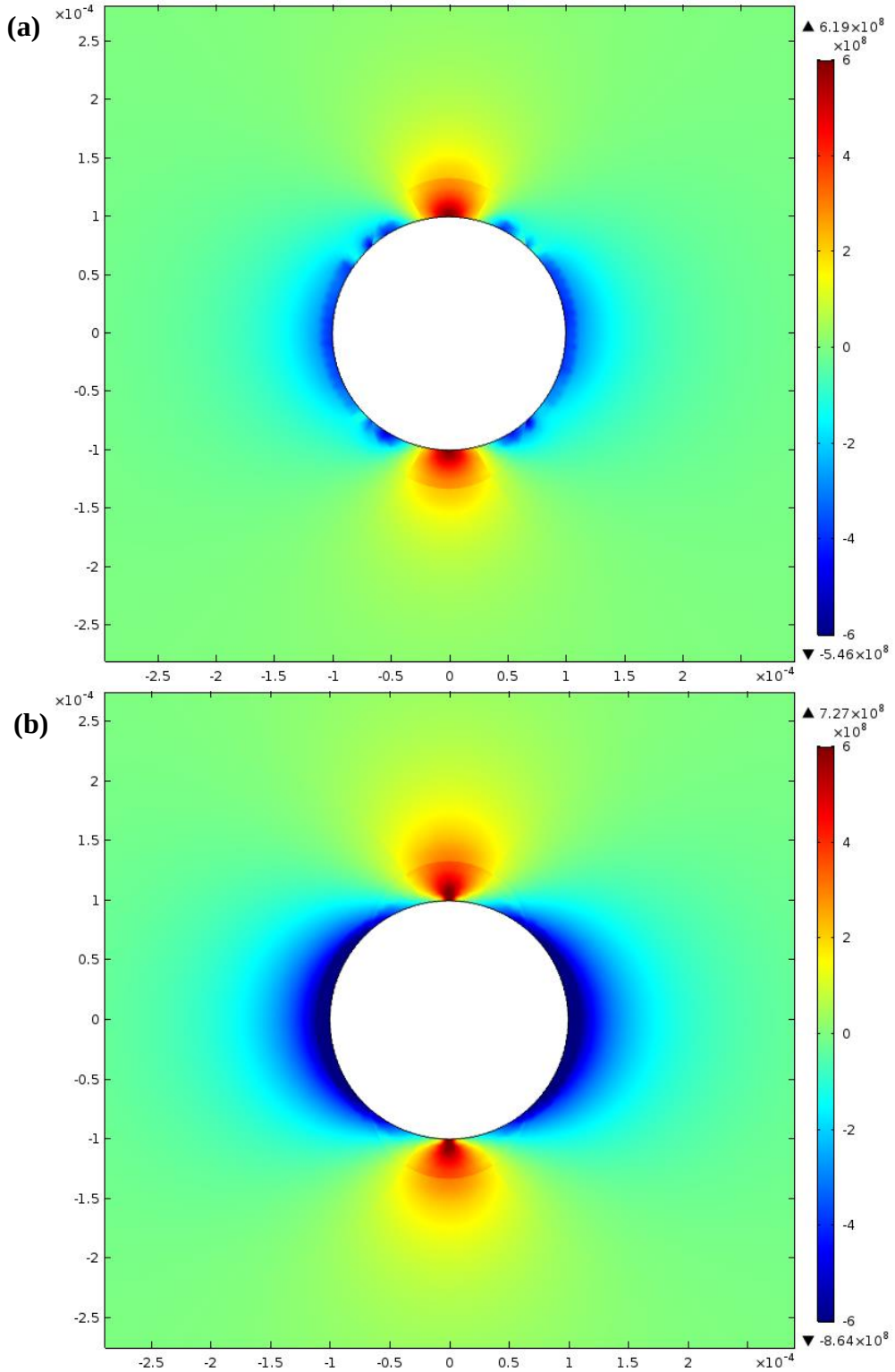

Figure 4.13 Contour plots of $\partial H_f / \partial r$ around the cylindrical target when (a) including and (b) excluding the effect of the MDCPs on the magnetic field with $\mu_0 H_0$ = 0.05 T at t = 10 s. The other parameters are given in Table 4.1.

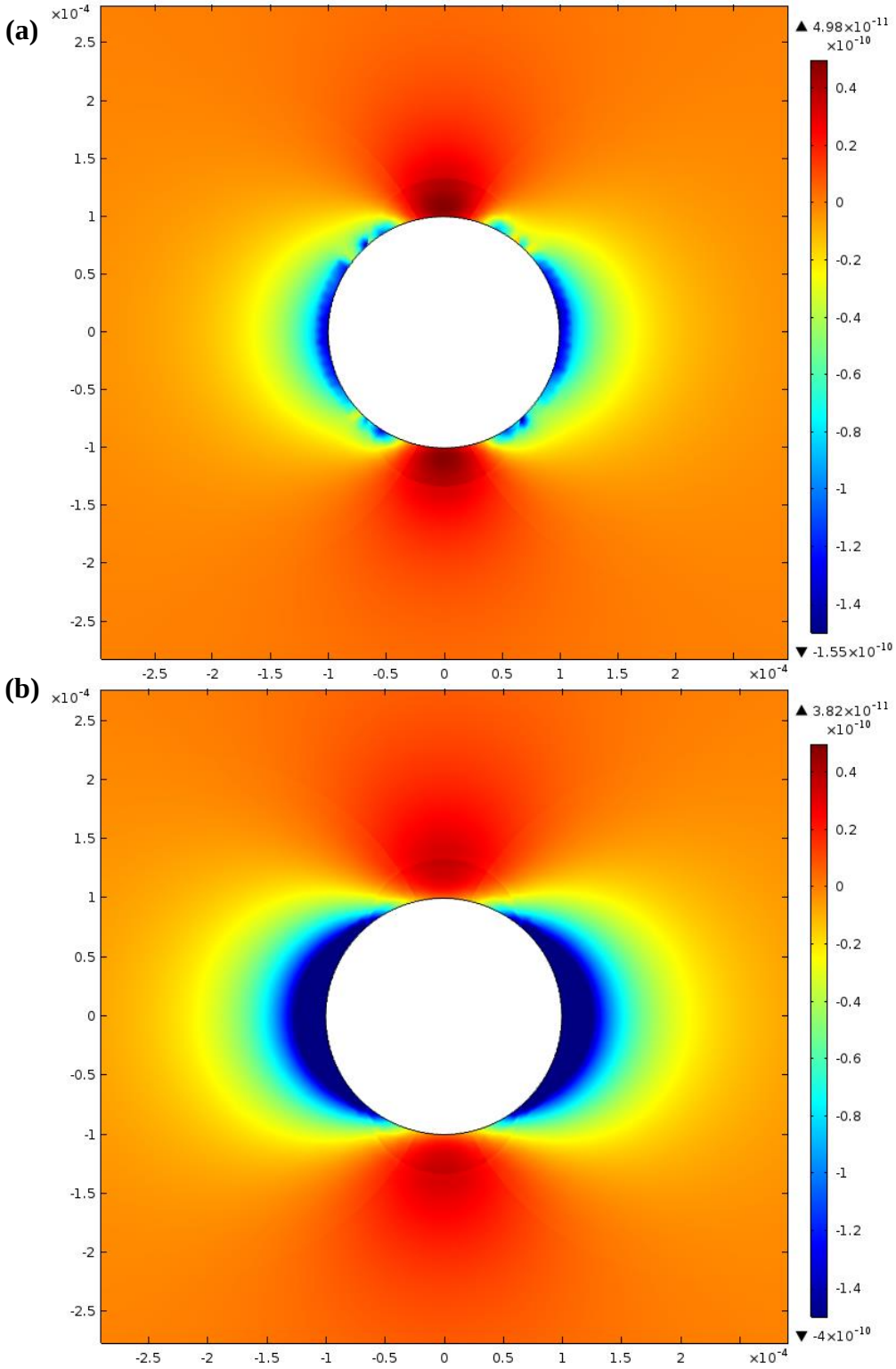

Figure 4.14 Contour plots of F_m around the cylindrical target when (a) including and (b) excluding the effect of the MDCPs on the magnetic field with $\mu_0 H_0$ = 0.05 T at t = 10 s. The other parameters are given in Table 4.1.

4.5 Conclusion

A dynamic modeling of time-dependent capture and accumulation of MDCPs by a ferromagnetic cylindrical target was developed. The effect of MDCP accumulation on both the fluid flow and local magnetic field around the magnetized cylindrical target is included in this dynamic model. This 2-D mathematical model considers the fluid viscosity as a function of the volume concentration of MDCPs in the fluid, with imposed maxima on both the particle volume concentration and fluid viscosity to prevent infinite limits. This model involved solving simultaneously in 2-D the unsteady-state Navier-Stokes equations for compressible fluid flow and the unsteady-state continuity equations applied separately to the MDCPs and water in the fluid, along with the Laplace equations for the magnetic potential applied separately to the inside and outside regions of the ferromagnetic cylindrical target. All of the equations were solved in COMSOL Multiphysics version 5.2. The solution provided the corresponding velocities and volume concentrations of MDCPs and water around the magnetized cylindrical target in a rectangular control area.

The simulation results from the dynamic model in this chapter were analyzed in terms of fluid flow and MDCP flux around the magnetized cylindrical target, breakthrough curve of the normalized output solid mass flow rate, mass of MDCPs collected, and capture efficiency. The mass of MDCPs collected (MC) were obtained and verified by using two different methods. One method considered the mass of MDCPs entering and leaving the control area and the other one considered the concentration of MDCPs within the control area. The MC from both methods agreed very well with each other. Therefore, this supported the consistency of the MC calculated by the two different methods and it also verified the model results.

The results from this dynamic model, in terms of fluid flow and MDCP flux, revealed very realistic magnetically attractive and repulsive regions forming around the magnetized cylindrical target in real time during the dynamic accumulation process of MDCPs. The analysis of breakthrough curve revealed a chromatographic effect that showed the removal of the MDCPs from the fluid stream by the dominant effect of

the magnetic force on MDCPs. This effect of magnetic force decreased with an increase in time as the collection zones grew and the hydrodynamic force began to dominate the MDCPs over the magnetic force, as shown by the results of the mass of MDCPs collected and the percentage capture efficiencies. Eventually, in all cases the collection zones ceased to grow after reaching a certain size when no more MDCPs could be captured by the target because of the strong hydrodynamic force and weak magnetic force. The results from these analyses revealed that it might be the first time that a 2-D mathematical model was shown to be capable of tracking the dynamic behavior of MDCP capture and accumulation process on the ferromagnetic cylindrical target in real time for IA-MDT systems.

The following behaviors were observed from the simulation results of this dynamic model. The collection zones around the cylindrical target increased and changed in shape with an increase in the uniform externally applied magnetic field strength. The collection zones were smaller when the effect of MDCP magnetization was included (realistic) in the dynamic model compared to that when it was not included (unrealistic) from the model. This was due a significant decrease in the magnetic flux around the magnetized target caused by magnetization of the MDCPs. Also, the capture ability decreased with an increase in size of the collection zones. This was due to a weakening magnetic force with increasing distance from the target and a strengthening hydrodynamic drag force in the narrowing gap between the edge of the collection zone and the rectangular control area wall.

The results in terms of percentage capture efficiency $\left(\%CE\right)$ as a function of the collection time from the dynamic model in this chapter were also compared to those obtained from a general steady-state, clean target, trajectory model. The results from the dynamic model exhibited a maximum in the $\%CE$ curve over time, which approaches to zero at infinite time. In contrast, the trajectory model, which provides a constant $\%CE$ over time, could not predict this realistic behavior. Moreover, the results of $\%CE$ suggested that the $\%CE$ predicted from the trajectory model are close to those from the dynamic model, which is more accurate, only in a short period of collection times when the accumulation of MDCPs is still low at the early collection time of the collection process because the assumption of the clean target was more

valid at that time. In addition, the results from both dynamic and trajectory models are also close to each other at the higher uniform externally applied magnetic field strength. This could be due to the saturation magnetization having a larger effect on the trajectory model than the dynamic model.

CHAPTER V
CONCLUSIONS

This three main topics of our investigations which were reported in this thesis are concluded as follows.

5.1 Three-Dimensional Trajectory Model for Magnetic Drug Targeting Using Micro-Spheres Implanted Within Large Blood Vessels

In Chapter II, implant assisted magnetic drug targeting (IA-MDT) using ferromagnetic spherical targets with dilute volume packing fraction implanted within large blood vessels and subjected to a uniform externally applied magnetic field has been investigated and reported. The equations of motion of MDCPs carried by the bloodstream were derived based on the magnetic field and blood velocity around a single spherical target implanted within large blood vessel. The blood flow is categorized into potential flow regime which the effect from the vessel wall is assumed to be negligible, and only the magnetic and hydrodynamic drag forces are the dominant forces acting on the MDCPs. The capture areas (A_s) of magnetic drug carrier particles (MDCPs) were obtained from the analysis of particle trajectories simulated from equations of motion. Then, the effects of various parameters, such as types of ferromagnetic materials in the targets and MDCPs, blood flow rates, mass fraction of the ferromagnetic material in the MDCPs, average radii of MDCPs (R_p) and the externally applied magnetic field strength $(\mu_0 H_0)$ on the A_s were determined. Furthermore, the effects of saturation magnetization of the ferromagnetic materials in the MDCPs and within the targets on the A_s were analyzed. After this, the appropriate $\mu_0 H_0$ and R_p for IA-MDT designs were reported. Dimensionless A_s, ranging from 2 to 7, was obtained with R_p ranging from 500 to 2500 nm, weight fraction of 80%, the $\mu_0 H_0$ of less than 0.8 T and a blood flow rate of 0.1 ms^{-1}. The target-MDCP materials considered are iron-iron, iron-magnetite and SS409-magnetite, respectively. The

simulation results in this chapter yield the predictions of MDCP sizes that are appropriate for various designs of IA-MDT systems.

5.2 Three-Dimensional Magnetic Drug Targeting With Spherical Targets by Bilinear Interpolation for Determining the Blood Velocity Profiles

In Chapter III, the three-dimensional (3-D) implant assisted-magnetic drug targeting (IA-MDT) using ferromagnetic spherical targets, including the effect from the vessel wall on the blood flow, has been presented. The targets were implanted within arterioles and subjected to an externally uniform applied magnetic field in order to increase the effectiveness of targeting magnetic drug carrier particles (MDCPs). The equations of motion of MDCPs, carried by the bloodstream towards a target magnetized by a uniform externally applied magnetic field, were derived based on the magnetic and hydrodynamic drag forces acting on the MDCPs. The blood flow was categorized as a laminar flow and the blood flow velocities at any particle position around the target were obtained by applying bilinear interpolation to the numerical blood velocity data. The capture area $\left(A_s\right)$ of the MDCPs was determined by inspection of the particle trajectories simulated from the particle equations of motion. The effects of the type of ferromagnetic materials in the targets and MDCPs, average blood flow rates, mass fraction of the ferromagnetic material in the MDCPs, average radii of MDCPs $\left(R_p\right)$ and the externally applied magnetic field strength $\left(\mu_0 H_0\right)$ on the A_s were evaluated and reported. Furthermore, the appropriate $\mu_0 H_0$ and R_p for the IA-MDT design is suggested. In the case of the SS409 target and magnetite MDCPs, dimensionless capture areas ranging from 4.1-12.4 and corresponding to particle capture efficiencies of 31-94% were obtained with R_p ranging from 100-500 nm, weight fraction of 80%, $\mu_0 H_0$ of 0.6 T and an average blood flow rate of 0.01 $\mathrm{m\,s^{-1}}$. In addition, the more general 3-D modelling of IA-MDT in this work is applicable to IA-MDT using spherical targets implanted within blood vessels of various sizes for both laminar and potential blood flows including the wall effect.

5.3 Simulation of Dynamic Magnetic Drug Carrier Particle Capture and Accumulation around a Ferromagnetic Cylindrical Target

In Chapter IV, a 2-D mathematical model for high gradient magnetic separation (HGMS)-type systems, such as IA-MDT, during the time-dependent (dynamic) capture and accumulation of MDCPs by a ferromagnetic cylindrical target was developed. This dynamic model assumes the fluid viscosity depends on the volume concentration of MDCPs in the fluid, with imposed maxima on both the particle concentration and fluid viscosity to avoid infinite limits. The unsteady-state Navier-Stokes equations for compressible fluid flow and the unsteady-state continuity equations applied separately to the liquid (water) and solid (MDCPs) phases in the fluid were solved simultaneously, along with the Laplace equations for the magnetic potential applied separately to the inside and outside regions of the ferromagnetic cylindrical target, in order to obtain the velocities and volume concentrations around the magnetized target within a rectangular control area. The simulation results from this dynamic model revealed very realistic magnetically attractive and repulsive zones dynamically forming around the cylindrical target. These collection zones created their own impermeable viscous phase during the accumulation process that has magnetism impact on both the fluid flow and local magnetic fields around the target, respectively. These collection zones increased with an increase in an uniform externally applied magnetic field. The results indicated that the capture ability increased and reached the maximum then it decreased to zero at infinite time during accumulation of MDCPs in the collection zones on the target. The predictions of the capture efficiency from a steady-state, clean collector, trajectory model could not exhibit this realistic behavior. The trajectory model were close to the dynamic model only at the early stages of collection process and at a higher externally applied magnetic field. In addition, the sizes of collection zones decreased when the magnetizations of MDCPs were included to the dynamic model compared to that when they were not included to the model. According to the simulation results, this dynamic model was revealed to be capable

of realistically predicting the dynamic behaviors of MDCP capture and accumulation around a ferromagnetic cylindrical target in HGMS-type systems.

REFERENCES

[1] Zheng, X., Wang, Y., and Lu, D. A realistic description of influence of the magnetic field strength on high gradient magnetic separation. Minerals Engineering 79 (2015): 94-101.

[2] Watson, J.H.P. Magnetic filtration. Journal of Applied Physics 44(9) (1973): 4209-4213.

[3] Hournkumnuard, K. and Natenapit, M. Diffusive Capture of Magnetic Particles by an Assemblage of Random Cylindrical Collectors. Separation Science and Technology 43(13) (2008): 3448-3460.

[4] Cregg, P.J., Murphy, K., and Mardinoglu, A. Inclusion of interactions in mathematical modelling of implant assisted magnetic drug targeting. Applied Mathematical Modelling 36(1) (2012): 1-34.

[5] Cregg, P.J., Murphy, K., Mardinoglu, A., and Prina-Mello, A. Many particle magnetic dipole–dipole and hydrodynamic interactions in magnetizable stent assisted magnetic drug targeting. Journal of Magnetism and Magnetic Materials 322(15) (2010): 2087-2094.

[6] Mardinoglu, A., Cregg, P.J., Murphy, K., Curtin, M., and Prina-Mello, A. Theoretical modelling of physiologically stretched vessel in magnetisable stent assisted magnetic drug targetingapplication. Journal of Magnetism and Magnetic Materials 323(3–4) (2011): 324-329.

[7] Haverkort, J.W., Kenjereš, S., and Kleijn, C.R. Computational Simulations of Magnetic Particle Capture in Arterial Flows. Annals of Biomedical Engineering 37(12) (2009): 2436-2448.

[8] Lunnoo, T. and Puangmali, T. Capture Efficiency of Biocompatible Magnetic Nanoparticles in Arterial Flow: A Computer Simulation for Magnetic Drug Targeting. Nanoscale Research Letters 10(1) (2015): 1-11.

[9] Choomphon-anomakhun, N. and Natenapit, M. 3-D trajectory model for MDT using micro-spheres implanted within large blood vessels. Journal of Magnetism and Magnetic Materials 413 (2016): 49-56.

[10] Hournkumnuard, K. and Natenapit, M. Magnetic drug targeting by ferromagnetic microwires implanted within blood vessels. Medical Physics 40(6) (2013): 062302.

[11] Sharma, S., Singh, U., and Katiyar, V.K. Modeling and in vitro study on capture efficiency of magnetic nanoparticles transported in an implant-assisted cylindrical tube under magnetic field. Microfluidics and Nanofluidics 19(5) (2015): 1061-1070.

[12] Torchilin, V.P. Targeting of drugs and drug carriers within the cardiovascular system. Advanced Drug Delivery Reviews 17(1) (1995): 75-101.

[13] Torchilin, V.P. Drug targeting. European Journal of Pharmaceutical Sciences 11, Supplement 2(0) (2000): S81-S91.

[14] Avilés, M.O., Ebner, A.D., and Ritter, J.A. Ferromagnetic seeding for the magnetic targeting of drugs and radiation in capillary beds. Journal of Magnetism and Magnetic Materials 310(1) (2007): 131-144.

[15] Lübbe, A.S., Alexiou, C., and Bergemann, C. Clinical Applications of Magnetic Drug Targeting. Journal of Surgical Research 95(2) (2001): 200-206.

[16] Rudge, S.R., Kurtz, T.L., Vessely, C.R., Catterall, L.G., and Williamson, D.L. Preparation, characterization, and performance of magnetic iron–carbon composite microparticles for chemotherapy. Biomaterials 21(14) (2000): 1411-1420.

[17] Rotariu, O. and Strachan, N.J.C. Modelling magnetic carrier particle targeting in the tumor microvasculature for cancer treatment. Journal of Magnetism and Magnetic Materials 293(1) (2005): 639-646.

[18] Ritter, J.A., Ebner, A.D., Daniel, K.D., and Stewart, K.L. Application of high gradient magnetic separation principles to magnetic drug targeting. Journal of Magnetism and Magnetic Materials 280(2–3) (2004): 184-201.

[19] Larimi, M.M., Ramiar, A., and Ranjbar, A.A. Numerical simulation of magnetic nanoparticles targeting in a bifurcation vessel. Journal of Magnetism and Magnetic Materials 362 (2014): 58-71.

[20] Avilés, M.O., Ebner, A.D., Chen, H., Rosengart, A.J., Kaminski, M.D., and Ritter, J.A. Theoretical analysis of a transdermal ferromagnetic implant for retention

of magnetic drug carrier particles. Journal of Magnetism and Magnetic Materials 293(1) (2005): 605-615.

[21] Bose, S. and Banerjee, M. Effect of non-Newtonian characteristics of blood on magnetic particle capture in occluded blood vessel. Journal of Magnetism and Magnetic Materials 374 (2015): 611-623.

[22] Wang, S., Zhou, Y., Tan, J., Xu, J., Yang, J., and Liu, Y. Computational modeling of magnetic nanoparticle targeting to stent surface under high gradient field. Computational Mechanics 53(3) (2014): 403-412.

[23] Chen, H., Ebner, A.D., Kaminski, M.D., Rosengart, A.J., and Ritter, J.A. Analysis of magnetic drug carrier particle capture by a magnetizable intravascular stent—2: Parametric study with multi-wire two-dimensional model. Journal of Magnetism and Magnetic Materials 293(1) (2005): 616-632.

[24] Cregg, P.J., Murphy, K., and Mardinoglu, A. Inclusion of magnetic dipole–dipole and hydrodynamic interactions in implant-assisted magnetic drug targeting. Journal of Magnetism and Magnetic Materials 321(23) (2009): 3893-3898.

[25] Chen, H., Ebner, A.D., Rosengart, A.J., Kaminski, M.D., and Ritter, J.A. Analysis of magnetic drug carrier particle capture by a magnetizable intravascular stent: 1. Parametric study with single wire correlation. Journal of Magnetism and Magnetic Materials 284(0) (2004): 181-194.

[26] Forbes, Z.G., Yellen, B.B., Halverson, D.S., Fridman, G., Barbee, K.A., and Friedman, G. Validation of High Gradient Magnetic Field Based Drug Delivery to Magnetizable Implants Under Flow. IEEE Transactions on Biomedical Engineering 55(2) (2008): 643-649.

[27] Avilés, M.O., Chen, H., Ebner, A.D., Rosengart, A.J., Kaminski, M.D., and Ritter, J.A. In vitro study of ferromagnetic stents for implant assisted-magnetic drug targeting. Journal of Magnetism and Magnetic Materials 311(1) (2007): 306-311.

[28] Avilés, M.O., Ebner, A.D., and Ritter, J.A. Implant assisted-magnetic drug targeting: Comparison of in vitro experiments with theory. Journal of Magnetism and Magnetic Materials 320(21) (2008): 2704-2713.

[29] Avilés, M.O., Ebner, A.D., and Ritter, J.A. In vitro study of magnetic particle seeding for implant assisted-magnetic drug targeting. Journal of Magnetism and Magnetic Materials 320(21) (2008): 2640-2646.

[30] Cregg, P.J., Murphy, K., and Mardinoglu, A. Calculation of nanoparticle capture efficiency in magnetic drug targeting. Journal of Magnetism and Magnetic Materials 320(23) (2008): 3272-3275.

[31] Forbes, Z.G., Yellen, B.B., Barbee, K.A., and Friedman, G. An approach to targeted drug delivery based on uniform magnetic fields. Magnetics, IEEE Transactions on 39(5) (2003): 3372-3377.

[32] Yellen, B.B., et al. Targeted drug delivery to magnetic implants for therapeutic applications. Journal of Magnetism and Magnetic Materials 293(1) (2005): 647-654.

[33] Chapra, S. and Canale, R. Numerical Methods for Engineers. McGraw-Hill Education, 2009.

[34] Davies, L.P. and Gerber, R. 2-D simulation of ultra-fine particle capture by a single-wire magnetic collector. Magnetics, IEEE Transactions on 26(5) (1990): 1867-1869.

[35] Chen, F., Smith, K.A., and Hatton, T.A. A dynamic buildup growth model for magnetic particle accumulation on single wires in high-gradient magnetic separation. AIChE Journal 58(9) (2012): 2865-2874.

[36] Liu, Y.A. and Oak, M.J. Studies in magnetochemical engineering. Part II: Theoretical development of a practical model for high-gradient magnetic separation. AIChE Journal 29(5) (1983): 771-779.

[37] Friedlaender, F.J., Takayasu, M., Rettig, J., and Kentzer, C. Particle flow and collection process in single wire HGMS studies. Magnetics, IEEE Transactions on 14(6) (1978): 1158-1164.

[38] Ebner, A.D. and Ritter, J.A. Retention of Iron Oxide Particles by Stainless Steel and Magnetite Magnetic Matrix Elements in High-Gradient Magnetic Separation. Separation Science and Technology 39(12) (2004): 2863-2890.

[39] Magnet, C., et al. Behavior of nanoparticle clouds around a magnetized microsphere under magnetic and flow fields. Physical Review E 89(3) (2014): 032310.

[40] Friedlaender, F. and Takayasu, M. A study of the mechanisms of particle buildup on single ferromagnetic wires and spheres. Magnetics, IEEE Transactions on 18(3) (1982): 817-821.

[41] Nesset, J. and Finch, J. The static (buildup) model of particle accumulation on single wires in high gradient magnetic separation: Experimental confirmation. Magnetics, IEEE Transactions on 17(4) (1981): 1506-1509.

[42] Moeser, G.D., Roach, K.A., Green, W.H., Alan Hatton, T., and Laibinis, P.E. High-gradient magnetic separation of coated magnetic nanoparticles. AIChE Journal 50(11) (2004): 2835-2848.

[43] Fletcher, D. Fine particle high gradient magnetic entrapment. Magnetics, IEEE Transactions on 27(4) (1991): 3655-3677.

[44] Fletcher, D. and Parker, M.R. Contribution of interparticle forces to the buildup of ultrafine colloidal particles around a magnetized fiber. Journal of Applied Physics 57(8) (1985): 4289-4291.

[45] Cowen, C., Friedlaender, F.J., and Jaluria, R. Single wire model of high gradient magnetic separation processes I. Magnetics, IEEE Transactions on 12(5) (1976): 466-470.

[46] Ebner, A.D. and Ritter, J.A. New correlation for the capture cross section in high-gradient magnetic separation. AIChE Journal 47(2) (2001): 303-313.

[47] Furlani, E.J. and Furlani, E.P. A model for predicting magnetic targeting of multifunctional particles in the microvasculature. Journal of Magnetism and Magnetic Materials 312(1) (2007): 187-193.

[48] Natenapit, M. and Sanglek, W. Capture radius of magnetic particles in random cylindrical matrices in high gradient magnetic separation. Journal of Applied Physics 85(2) (1999): 660-664.

[49] Friedlaender, F.J., Gerber, R., Kurz, W., and Birss, R. Particle motion near and capture on single spheres in HGMS. Magnetics, IEEE Transactions on 17(6) (1981): 2801-2803.

[50] Moyer, C., Natenapit, M., and Arajs, S. Particle capture by an assemblage of spheres in high-gradient magnetic separation. Journal of Applied Physics 55(6) (1984): 2589-2591.

[51] Jackson, J.D. Classical electrodynamics. 3rd ed. New York, NY: Wiley, 1999.

[52] Berger, S.A., Goldsmith, E.W., and Lewis, E.R. Introduction to Bioengineering. OUP Oxford, 2000.

[53] Cherry, E.M., Maxim, P.G., and Eaton, J.K. Particle size, magnetic field, and blood velocity effects on particle retention in magnetic drug targeting. Medical Physics 37(1) (2010): 175-182.

[54] Choomphon-anomakhun, N. and Natenapit, M. Three-dimensional magnetic drug targeting with spherical targets by bilinear interpolation. Journal of Magnetism and Magnetic Materials in revision (2017).

[55] Brouwers, H.J.H. Viscosity of a concentrated suspension of rigid monosized particles. Physical Review E 81(5) (2010): 051402.

[56] Choomphon-anomakhun, N., Ebner, A.D., Natenapit, M., and Ritter, J.A. Simulation of dynamic magnetic particle capture and accumulation around a ferromagnetic wire. Journal of Magnetism and Magnetic Materials 428 (2017): 493-505.

[57] Gerber, R. Magnetic Separation. in Gerber, R., Wright, C.D., and Asti, G. (eds.),Applied Magnetism, pp. 165-220: Springer Netherlands, 1994.

[58] Jackson, J. Classical Electrodynamics Third Edition. Wiley, 1998.

APPENDIX

APPENDIX A

THE NEW CORRELATION FOR THE CAPTUER CROSS-SECTION IN HGMS

The new correlation method developed by Ebner and Ritter [46] assumes that the cylindrical target is clean, the blood flowing past the target is categorized into potential flow regime, the effects of the vessel wall on both the blood flow and MDCPs are neglected and the magnetic and hydrodynamic drag forces are the only forces acting on MDCPs.

The dimensionless capture distance $\left(R_c\right)$, which is the capture distance divided by the target radius, is evaluated from [25, 46]

$$\ln R_c = \frac{-B-\sqrt{B^2-4C}}{2}, \tag{A1}$$

where

$$B = -\left(\left(d_1+d_2\right)\left(\ln K_w - \ln K_{w,0}\right)+\left(e_1+e_2\right)\right) \tag{A2}$$

and

$$C = \left(d_1\left(\ln K_w - \ln K_{w,0}\right)+e_1\right)\left(d_2\left(\ln \alpha_w - \ln K_{w,0}\right)+e_2\right)-c_1. \tag{A3}$$

c_1 , d_1 , d_2 , e_1 and e_2 are constants in the correlation. K_w is demagnetization factor of the ferromagnetic material inside the wire. $K_w = 1$ if the ferromagnetic material contained in the cylindrical target is not magnetically saturated and $K_w = M_{w,s}/2H_0$ when the ferromagnetic material is saturated. $M_{w,s}$ are the saturation magnetization of the ferromagnetic material in the target, respectively. $K_{w,0}$ is a function defined in the correlation and evaluated according to [25, 46]

$$\ln K_{w,0} = \frac{-B_0 - \sqrt{B_0^2 - 4C_0}}{2} \tag{A4}$$

where

$$B_0 = -\left(\left(a_1 + a_2\right)\ln \beta_w + \left(b_1 + b_2\right)\right), \tag{A5}$$

and

$$C_0 = \left(a_1 \ln \beta_w + b_1\right)\left(a_2 \ln \beta_w + b_2\right) - c_2. \tag{A6}$$

a_1, a_2, b_1, b_2 and c_2 are constants in the correlation, and β_w is defined as

$$\beta_w = \frac{2\omega_{fm,p} R_w \mu_0 H_0^2 \alpha_{fm,p} R_p^2}{\eta_b u_b R_w}, \tag{A7}$$

where η_b, u_b, R_w, R_p, μ_0 and H_0 represent the viscosity of the blood, the velocity of the blood, the radius of the wire, the radius of the MDCP, the permeability of free space and the uniform externally applied magnetic field. $\omega_{fm,p}$ is the volume fraction of the ferromagnetic material inside the MDCPs as given in Eq. (2.4). $\alpha_{fm,p}$ is the demagnetization factor of the ferromagnetic material in MDCPs. If the ferromagnetic material contained in MDCPs is not magnetically saturated, $\alpha_{fm,p} = 1$. When the external magnetic field is high enough, the ferromagnetic material inside the spherical MDCPs becomes magnetically saturated with $\alpha_{fm,p} = M_{fm,p,s} / 3H_0$, where $M_{fm,p,s}$ represents the saturation magnetization.

The capture distance of the wire is evaluated from the single wire HGMS correlation [46] for the transverse configuration using Eqs. (A1) – (A7). The correlation constants are given in Table A1.

Table A1 The parameters for the single wire HGMS capture cross-section correlation under the transversal configuration [25, 46]

Parameters	Value
a_1	-0.48990
a_2	-1.02248
b_1	0.52197
b_2	1.50099
c_1	0.36778
c_2	1.66374
d_1	0.34487
d_2	2.07542
e_1	0.77117
e_2	2.07217

APPENDIX B
THE EQUATIONS OF MOTION FOR THE MDCPS CAPTUER BY THE CYLINDRICAL TARGET

The equations of motion of MDCPs for a single cylindrical target model which were used for simulations to acquire the results in Figs. 2.2 and 2.3, are derived in transverse mode with a uniform externally applied magnetic field $(\boldsymbol{H}_0)$ and inlet bloodstream of potential flow $(\boldsymbol{v}_0)$ are perpendicular and both the $\boldsymbol{H}_0$ and $\boldsymbol{v}_0$ are normal to the cylindrical target axis.

The magnetic field strength (H) around the cylindrical target of radius a subjected to the field H_0 which is in the $\hat{\boldsymbol{x}}$ direction was obtained in polar coordinates as follows [57, 58]:

$$H = H_0\left(1+\frac{K_w^2}{r_a^4}+\frac{2K_w}{r_a^2}\cos 2\theta\right)^{\frac{1}{2}}, \tag{B1}$$

where $r_a = r/a$ and $K_w = \chi_{w,0}/(2+\chi_{w,0})$ if the ferromagnetic material contained in the cylindrical target is not magnetically saturated and $K_w = M_{w,s}/2H_0$ when the ferromagnetic material is saturated. $\chi_{w,0}$ and $M_{w,s}$ are the magnetic susceptibility of the ferromagnetic material in the target at zero magnetic field and the saturation magnetization of the ferromagnetic material in the target, respectively.

The blood flow velocity around the cylindrical target is expressed as follows [57]:

$$\boldsymbol{v}_b = v_0\left(1-\frac{1}{r_a^2}\right)\sin(\theta)\hat{\boldsymbol{r}} + v_0\left(1+\frac{1}{r_a^2}\right)\cos(\theta)\hat{\boldsymbol{\theta}}, \tag{B2}$$

for the uniform inlet blood flow velocity $\boldsymbol{v}_0$ in $\hat{\boldsymbol{y}}$ direction. $\hat{\boldsymbol{r}}$ and $\hat{\boldsymbol{\theta}}$ are unit vectors in polar coordinates.

By substituting v_b from Eq. (A2) and $\boldsymbol{M}_{fm,p} = 3\alpha_{fm,p}\boldsymbol{H}$ into Eq. (2.13) and using Eq. (A1), the equations of motion of the MDCPs can be expressed as

$$\frac{dr_a}{dt} = v_{0a}\left(1-\frac{1}{r_a^2}\right)\sin(\theta) - \frac{V_{ma}}{r_a^3}\left[\frac{K_w}{r_a^2} + \cos 2\theta\right], \tag{B3}$$

$$\frac{d\theta}{dt} = \frac{v_{0a}}{r_a}\left(1+\frac{1}{r_a^2}\right)\cos(\theta) - \frac{V_{ma}}{r_a^4}\sin 2\theta, \tag{B4}$$

where $v_{0a} = v_0/a$, and $V_{ma} = \dfrac{4R_p^2\omega_{fm,p}K_w\alpha_{fm,p}\mu_0 H_0^2}{3\eta_b a^2}$ is magnetic velocity. For the ferromagnetic material contained in MDCPs at before and after magnetic saturation, $\alpha_{fm,p}$ equals to $\chi_{fm,p,0}/(3+\chi_{fm,p,0})$ and $M_{fm,p,s}/3H_0$, respectively [25].

APPENDIX C

THE FLOW CHART FOR THE SIMULATION OF THE MDCPS CAPTUER BY THE SPHERICAL TARGET

The flow chart including explanation in this simulation is provided in Appendix of Ref. [9] as follows.

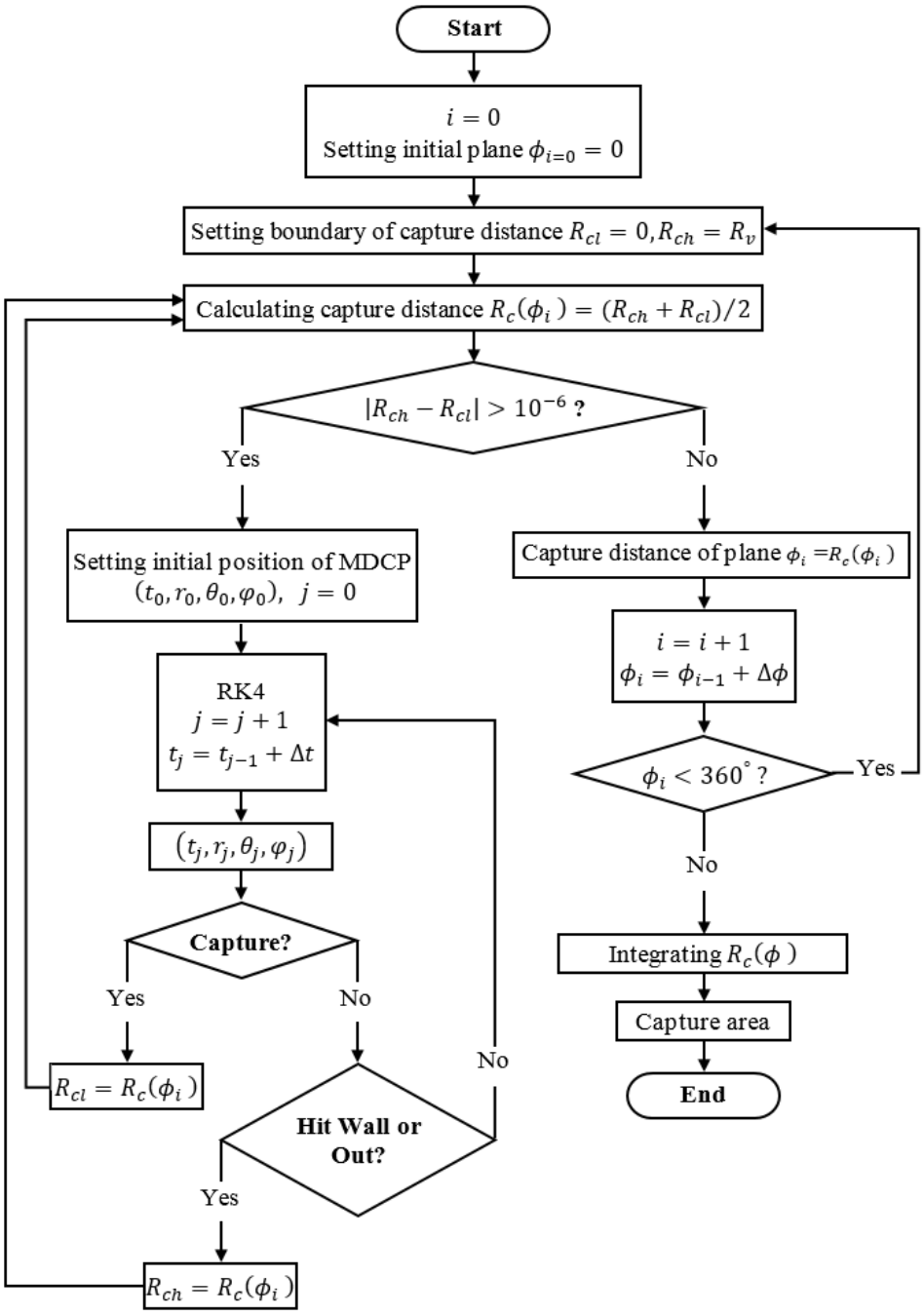

i is an iteration number of plane.

R_{cl} and R_{ch} are the lower and upper boundaries of the interval of capture distance.

R_v is the vessel radius.

RK4 is the fourth-order Runge-Kutta method.

Δt is time step in RK4.

j is an iteration number of calculation step in RK4.

$\Delta\phi$ is the angle difference between two adjacent planes.

In this work, Δt and $\Delta\phi$ of 5 degree and 10^{-7} s, respectively, are used in the simulation.

APPENDIX D

THE BILINEAR INTERPOLATION OF NUMERICAL BLOOD VELOCITY

The blood velocities at any MDCP position ($v_{b,r}$ and $v_{b,\theta}$) in the equations of motion (3.12) and (3.13), respectively, are required to achieve the simulation for the particle trajectories. To obtain the $v_{b,r}$ and $v_{b,\theta}$ at every solving time step, we used the numerical blood velocity data that was first exported from the CFD software and stored at the reference points inside the blood vessel. Then, the $v_{b,r}$ and $v_{b,\theta}$ at any time step could be obtained using an interpolation method based on the stored blood velocity data at those reference points.

The numerical blood velocity data on the plane φ = 0 is adequate for estimating the blood velocities at any particle position around the target because the blood velocity is independent of φ, as shown in Fig. 3.1 for the inlet blood velocity in $-\hat{\boldsymbol{z}}$ direction. In this work, bilinear interpolation [33] was used. The suitable and simple way to generate the reference points for bilinear interpolation is to create a 2-D Cartesian grid on the XZ plane ($\varphi = 0$), where the elements of the grid are squares and the vertices of the elements are used as the reference points. The reference points are represented in a rectangular coordinate system (x, z), because it is easy to determine the element that contains the required position of blood velocity. Then, the blood velocity data ($v_{b,r}$ and $v_{b,\theta}$) at all reference points are stored. The length of the square element (ΔL) was chosen to be 0.005 of the target radius, which was small enough to avoid an overlap between the target surface and the element that contained the particle position where the blood velocity had to be determined.

To obtain the blood velocity at the particle position $(r_i, \theta_i, \varphi_i)$, the corresponding position (x_i, z_i) on the XZ plane, φ = 0, was first determined, as shown in the flow chart. Then, the element that contained this position was located. The reference points, which are the four vertices of the element, namely: (x_m, z_n), (x_{m+1}, z_n), (x_m, z_{n+1}) and (x_{m+1}, z_{n+1}), as shown in Fig. C1. Then, the blood velocity data at the four reference points, namely: $v_{b,k}(x_m, z_n)$, $v_{b,k}(x_{m+1}, z_n)$, $v_{b,k}(x_m, z_{n+1})$ and

$v_{b,k}(x_{m+1}, z_{n+1})$, where $k = r$ and θ, were retrieved from the stored data. Finally, bilinear interpolation [33] was used to interpolate the blood velocity at the corresponding position $v_{b,k}(x_i, z_i)$ as described below.

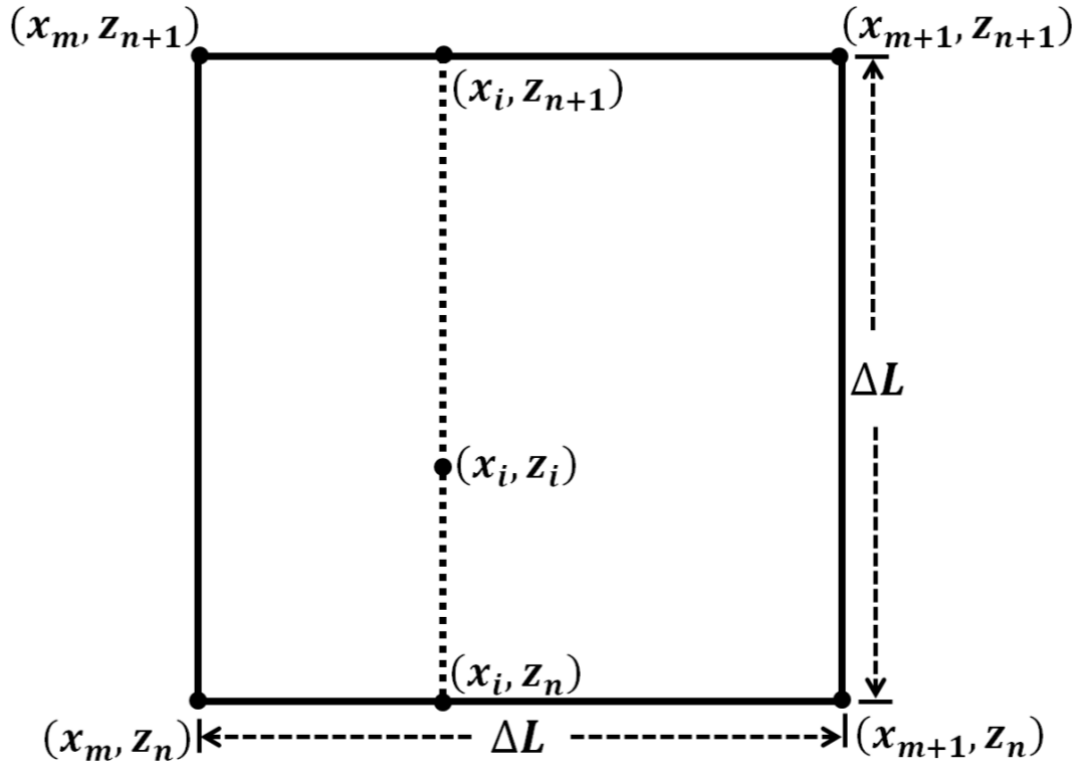

Figure C1 The particle position (x_i, z_i) inside a square element with a length of ΔL is surrounded by four reference points (x_m, z_n), (x_{m+1}, z_n), (x_m, z_{n+1}) and (x_{m+1}, z_{n+1}), which were used for exporting the blood velocity data from the CFD software.

Bilinear interpolation [33] was implemented by first applying one-dimensional linear interpolation along the $\hat{x}$ direction in order to determine $v_{b,k}(x_i, z_n)$ and $v_{b,k}(x_i, z_{n+1})$, using Eqs. (D1) and (D2), respectively:

$$v_{b,k}(x_i, z_n) = \left(\frac{x_{m+1} - x_i}{\Delta L}\right) v_{b,k}(x_m, z_n) + \left(\frac{x_i - x_m}{\Delta L}\right) v_{b,k}(x_{m+1}, z_n), \quad \text{(D1)}$$

$$v_{b,k}(x_i, z_{n+1}) = \left(\frac{x_{m+1} - x_i}{\Delta L}\right) v_{b,k}(x_m, z_{n+1}) + \left(\frac{x_i - x_m}{\Delta L}\right) v_{b,k}(x_{m+1}, z_{n+1}), \quad \text{(D2)}$$

and then $v_{b,k}(x, z_n)$ and $v_{b,k}(x, z_{n+1})$ were used to linearly interpolate along the $-\hat{\boldsymbol{z}}$ direction to yield the $v_{b,k}(x_i, z_i)$ using Eq. (D3),

$$v_{b,k}(x_i, z_i) = \left(\frac{z_{n+1} - z_i}{\Delta L}\right) v_{b,k}(x_i, z_n) + \left(\frac{z_i - z_n}{\Delta L}\right) v_{b,k}(x_i, z_{n+1}). \quad \text{(D3)}$$

The components of the blood velocity at the corresponding position $v_{b,k}(x_i, z_i)$ yield the blood velocity at the particle position $v_{b,k}(r_i, \theta_i, \varphi_i)$. Therefore, $v_{b,r}$ and $v_{b,\theta}$ in Eqs. (3.12) and (3.13), respectively, which are required to simulate the particle trajectories, are obtained.

The flow chart summarized the process of obtaining the components of the blood velocity at the particle position $v_{b,k}(r_i, \theta_i, \varphi_i)$ at any time step using bilinear interpolation are shown in Appendix of Ref. [54] as follows.

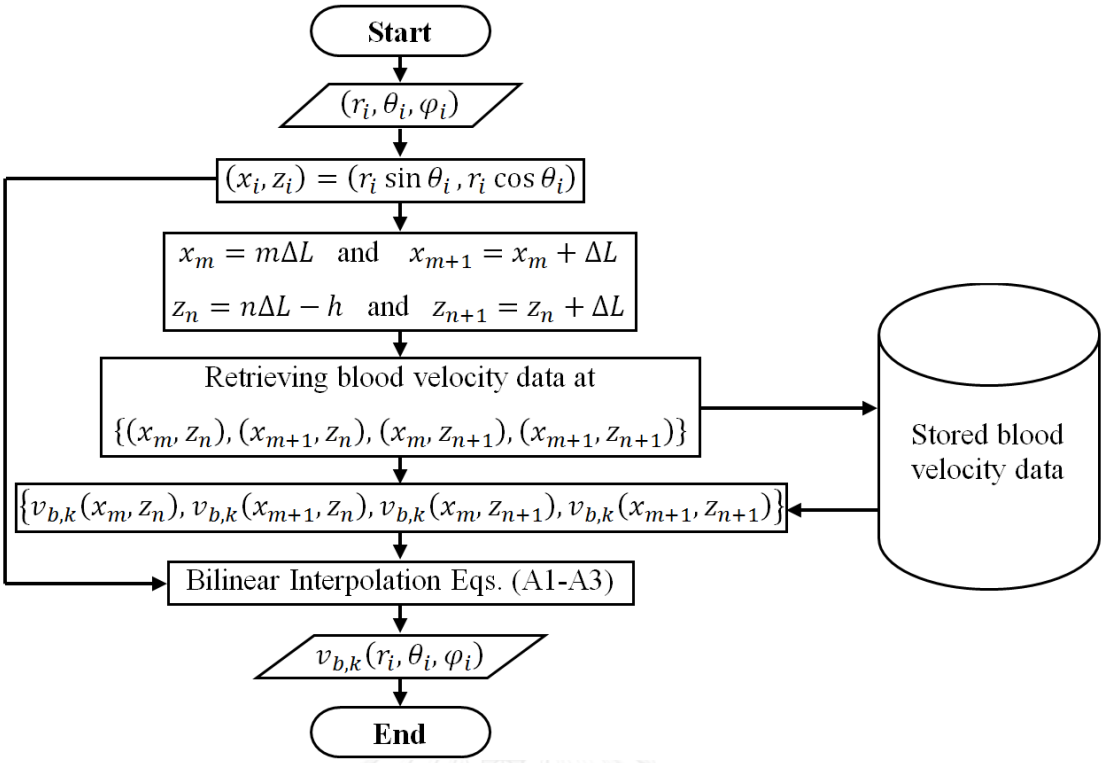

The integer m and n are in the ranges of 0 to $\lfloor R_v/\Delta L \rfloor$ and 0 to $\lfloor 2h/\Delta L \rfloor$, respectively.

ΔL is the distance between the adjacent reference points which is 0.005 of target radius.

$2h$ is the considered length of blood vessel, where h = 10 in unit of target radius.

APPENDIX E
THE CAPTURE EFFICIENCY OF MDCPS BY A FERROMAGNETIC CYLINDRICAL TARGET

For the 2-D model of MDCP capture by a ferromagnetic cylindrical target located in a rectangular control area as in Chapter IV, the capture efficiency of MDCPs for trajectory model is defined by [14, 18, 23]

$$\%CE = \frac{2R_c}{w} \times 100\% \tag{E1}$$

where R_c is the capture distance of the ferromagnetic target. w is the width of rectangular control area shown in Fig. 4.1. The capture distance is determined by analyzing the trajectories of MDCPs. The equations of motion of the MDCPs are constructed by considering the force balance between magnetic and fluid drag forces acting on the particle as shown in Chapter II and III. The force balance equation is expressed as [4, 7, 14, 18, 20, 23]:

$$\boldsymbol{F}_m + \boldsymbol{F}_d = \boldsymbol{F}_i \tag{E2}$$

where $\boldsymbol{F}_m$, $\boldsymbol{F}_d$ and $\boldsymbol{F}_i$ represent the magnetic, drag and inertial forces acting on the MDCPs, respectively. The inertial force $(\boldsymbol{F}_i)$ is negligible for the capture of small magnetic particles, then, Eq. (E2) can be written as [4, 7, 14, 18, 20, 23]:

$$\boldsymbol{F}_m + \boldsymbol{F}_d = 0 \tag{E3}$$

In the trajectory model of this work, the fluid flow within the rectangular control area is a steady-state flow, unaffected by any magnetic forces, which the viscosity of water (μ_w) is used instead of Eq. (4.17).

The fluid flow velocity $\left(\boldsymbol{v}_f\right)$ satisfies both the continuity equation for an incompressible fluid at steady state,

$$\nabla \cdot \boldsymbol{v}_f = 0, \tag{E4}$$

and the Navier-Stokes equation for a Newtonian fluid at steady state,

$$\rho_w \left[\left(\boldsymbol{v}_f \cdot \nabla\right)\boldsymbol{v}_f\right] = \nabla P + \mu_w \nabla^2 \boldsymbol{v}_f, \tag{E5}$$

where ρ_w and $\boldsymbol{P}$ are the density and pressure of water.

In order to determine the $\boldsymbol{v}_f$, both Eqs. (E7) and (E8) are solved numerically by using CFD software. No-slip boundary conditions, which both the perpendicular and parallel directions of fluid flow velocity vanished, are applied at the target surface and control area wall. The fluid flow is laminar flow and the parabolic flow velocity profile as shown in Eq. (4.5) is used as an inlet boundary condition.

By substituting $\boldsymbol{F}_m$ and $\boldsymbol{F}_d$ from Eqs. (4.14) and (4.25) into Eq. (E3), the particle velocity $\left(\boldsymbol{v}_p\right)$ can be obtained as follows:

$$\boldsymbol{v}_p = \boldsymbol{v}_f + \frac{1}{9}\frac{\mu_0 \omega_{fm,p} R_p^2}{\mu_w} \nabla\left(\boldsymbol{M}_{fm,p} \cdot \boldsymbol{H}_f\right), \tag{E6}$$

where all parameters in Eq. (E6) are already given in Chapter IV.

The local magnetic field strength $\left(H_f\right)$ around the ferromagnetic cylindrical target of radius R_w magnetized by the uniform externally applied magnetic field $\left(\boldsymbol{H}_0\right)$ in $\hat{\boldsymbol{x}}$ direction is given in polar coordinates as follows [3, 10]:

$$\boldsymbol{H}_f = \boldsymbol{H}_0 \left(1 + \left(\frac{M_w}{2H_0}\right)^2 \left(\frac{R_w}{r}\right)^4 + \left(\frac{M_w}{H_0}\right)\left(\frac{R_w}{r}\right)^2 \cos 2\theta\right)^{\frac{1}{2}}. \tag{E7}$$

When the magnetization of the ferromagnetic material in MDCPs is not magnetically saturated, the equations of motion of the MDCPs are obtained, by using Eqs. (E6) with (E7) and Eq. (4.17), as follows:

$$\frac{dr_a}{dt} = \frac{v_{b,r}}{a} - \frac{\alpha_{fm,p} V_{ma}}{r_a^3}\left[\frac{K_w}{r_a^2} + \cos 2\theta\right], \tag{E8}$$

$$\frac{d\theta}{dt} = \frac{v_{b,\theta}}{ar_a} - \frac{\alpha_{fm,p} V_{ma}}{r_a^4}\sin 2\theta, \tag{E9}$$

where $V_{ma} = \dfrac{4R_p^2 \omega_{fm,p} K_w \mu_0 H_0^2}{3\mu_w a^2}$ is defined as magnetic velocity. For the ferromagnetic material contained in MDCPs at before and after magnetic saturation, $\alpha_{fm,p}$ equals to $\chi_{fm,p,0}/\left(3+\chi_{fm,p,0}\right)$ and $M_{fm,p,s}/3H_0$, respectively

When the magnetization of the ferromagnetic material in MDCPs is magnetically saturated, the Eqs. (E8) and (E9) become as follows:

$$\frac{dr_a}{dt} = \frac{v_{b,r}}{a} - \frac{M_{fm,p,s} V_{ma}}{6Hr_a^3}\left[\frac{K_w}{r_a^2} + \cos 2\theta\right], \tag{E10}$$

$$\frac{d\theta}{dt} = \frac{v_{b,\theta}}{ar_a} - \frac{M_{fm,p,s} V_{ma}}{6Hr_a^4}\sin 2\theta. \tag{E11}$$

The $v_{b,r}$ and $v_{b,\theta}$ are the components of blood flow velocity in polar coordinates at the particle position for any times which are determined by applying bilinear interpolation [33] to the blood velocity data found from CFD software, as described in the Appendix C.

To draw the trajectories of the MDCPs, Eqs. (E8) and (E9) will be integrated numerically by using the forth-order Runge-Kutta method. Then, the capture distance is evaluated by analyzing the trajectories of MDCPs and the percentage capture efficiency based on trajectory model is obtained from Eq. (E1).

APPENDIX F

THE DIAGRAM OF MAGNETIC FORCE ACTING ON MDCPS AROUND A MAGNETIZED CYLINDRICAL FERROMAGNETIC TARGET

In order to describe the movement of MDCPs around the magnetized cylindrical ferromagnetic target, the direction of magnetic force acting on MDCPs in various regions around a target is depicted in Fig. E1 with the parameters given in Ref. [10]. The MDCPs carried by the blood flow move toward the target in $-\hat{\boldsymbol{y}}$ direction, which is perpendicular to the direction of uniform externally applied magnetic field $\left(B_0\hat{\boldsymbol{x}}\right)$, experience a repulsive magnetic force. Then, they are swept by the influences of both the magnetic and blood drag forces into the left and right sides of the target. Consequently, there is no particle capture on the top side of the target.

For the left and right sides of the target, which are attractive regions, the local magnetic field and its gradient are strongest resulting in the MDCPs are attracted towards the target surface under the dominant magnetic force acting on the MDCPs. At very close to the target surface, where the blood velocity approaches to zero because of no-slip boundary condition at the target-blood interface and the attractive magnetic force is much stronger so the MDCPs are easily captured by the target in these regions.

For the region under the target, the MDCPs experience a repulsive magnetic force, as same as the top side of the target, then some of the MDCPs are forced to move away from the target surface under the influences of both the repulsive magnetic and the blood drag forces. Consequently, there is also no particle capture on the region under the target.

In addition, the trajectories of MDCPs under the influences of magnetic and hydrodynamic blood drag forces can be seen in Fig. 3.2 with explanation in Chapter III. Furthermore, the dynamic behaviors of MDCPs under the influences of magnetic, drag and diffusion forces can be observed through the particle volume fraction as shown in Fig. 4.3 with details described in Chapter IV.

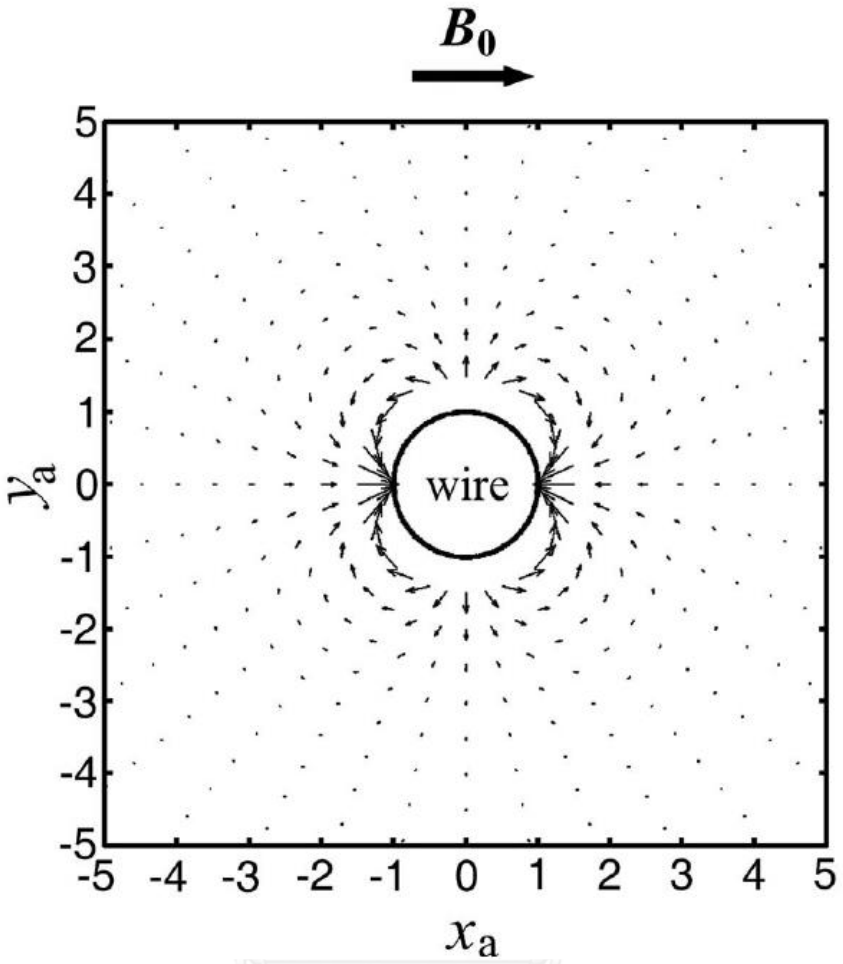

Figure E1 The direction of magnetic force acting on MDCPs in various regions around a magnetized cylindrical ferromagnetic target [10].

VITA

Name: Acting Sub. Lt. Natthaphon Choomphon-anomakhun

Education: 2011 B.Sc. in Physics (2nd class honor), Chulalongkorn University, Bangkok 10330, Thailand

Publications:

N. Choomphon-anomakhun, M. Natenapit, 3-D trajectory model for MDT using micro-spheres implanted within large blood vessels, Journal of Magnetism and Magnetic Materials, 413 (2016) 49-56.

N. Choomphon-anomakhun, A.D. Ebner, M. Natenapit, J.A. Ritter, Simulation of dynamic magnetic particle capture and accumulation around a ferromagnetic wire, Journal of Magnetism and Magnetic Materials, 428 (2017) 493-505.

N. Choomphon-anomakhun, M. Natenapit, Three-dimensional magnetic drug targeting with spherical targets by bilinear interpolation for determining the blood velocity profiles. The article has been submitted for publishing in Journal of Magnetism and Magnetic Materials and is in revision.

Presentations

N. Choomphon-anomakhun, M. Natenapit, Dynamic Behaviors of drug carrier nanoparticles in magnetic drug targeting, The 8th Mathematics and Physical Science Graduate Congress, Chualongkorn University, Thailand, 2012.

N. Choomphon-anomakhun, M. Natenapit, Capture area of magnetic particles for implant-assisted magnetic drug targeting in large arteries, The 9th Mathematics and Physical Science Graduate Congress, University of Malaya, Malaysia, 2014.

N. Choomphon-anomakhun, M. Natenapit, 3-D IA-MDT model using micro-spheres implanted within blood vessels, The RGJ-Ph.D. Congress XVII, Thailand, 2016.